



Camilo Perez Demydenko

Static and dynamic disorder in nanocrystalline materials

UNIVERSITY OF TRENTO



Doctoral School in Civil, Environmental and Mechanical Engineering
Topic 3. Modelling and Simulation - XXX cycle 2015/2018

Doctoral Thesis - February 2019

Camilo Perez Demydenko

Static and dynamic disorder in nanocrystalline materials

Supervisor

Prof. Paolo Scardi - University of Trento, Italy

Approved by

Prof. Bob Cernik - University of Manchester, UK

Prof. Nathalie Audebrand - University of Rennes 1, France



Contents on this book are licensed under a Creative Common Attribution
Non Commercial - No Derivatives
4.0 International License, except for the parts already published by other publishers.

University of Trento
Doctoral School in Civil, Environmental and Mechanical Engineering
<http://web.unitn.it/en/dricam>
Via Mesiano 77, I-38123 Trento
Tel. +39 0461 282670 / 2611 - *dicamphd@unitn.it*

to my mother

Acknowledgments

My PhD passed under a constant stress because of work. But things would have been even more difficult without the help and love from some people I met on this side of the world. I have to start with Cristy, my Cuban colleague who went to pick up me from Verona airport, the first time I arrive to Italy, in December 10, 2014. At that time I didn't know even one word in Italian and had zero experience in traveling abroad or using the Internet for getting any guidance; to come from the airport to Trento on my own seemed to me almost impossible. That was also the same day I met Pablo, my Brazilian friend. That night I passed literally from Cristy's hands to Pablo's hands, when I arrived to the student residence of San Bartolomeo. During all my first year Pablo was my one-person-teaching-me-everything I need. I appreciate a lot your help in every aspect of my early life in Trento, Pablo. Then I met my kitchen friends at the student residence. Wassim, with the loudest ever laugh, Luis, my always smiling Mexican friend, Aravind, the friendly Indian with his green plastic plate, Michaela, my Romanian Erasmus-student friend, always planning parties, and Preet, my cooking friend: thanks to you I was not the only one cooking every day! I made a separated group of friends in the faculty as well. Narges, my happy Iranian friend, Elena and Ricardo from Trento, and Roberto, Rocco, Angela, and Vincenzo, my Italian friends from the south. To all of you, thanks for making my days in the faculty and also many others outside. The only times I played football in Italy were with you, and those that always made my birthday parties were also you. Thanks! I would like to thanks also my Italian colleagues at the lab, Luca and Alberto. What surprised me from the very first time I met you, was how you always found the time to help me at work when I needed, despite being always busy with your own stuffs. I would like to thank also the University of Trento, for giving me access to all its facilities, including the student residence of San Bartolomeo, as well the Italian supercomputing center, CINECA, for hosting my calculations in the last months of the PhD, allowing me to get the results on time. Last, I would like to thanks to Professor Paolo Scardi for accepting me as his PhD student and supporting

my scholarship during all these years. As for the city, I leave Trento with the opinion that it is a very good place to study in Italy.

I want to thank also my family for their support all these years, specially to my mother. I think I reached this point in my life thanks to the way she educated me.

I can not finish these words without thanking the researchers and friends at the Institute of Material Science and Technology (IMRE) of the University of Havana, Cuba, who made possible my Master degree in Materials Science and later paved the way for the beginning of my PhD at Trento. Spacial thanks goes to Professor Ernesto Estévez Rams, for being my tutor during my Master and having accepted me as his student back in 2012, rescuing me from a non scientific career.

Scientific production

List of publications:

1. C. Perez-Demydenko and P. Scardi. Diffraction peak profiles of surface relaxed spherical nanocrystals. *Philosophical Magazine*, 97(26): 2317–2346, 2017.
2. P. Scardi, C. L. Azanza Ricardo, C. Perez-Demydenko, and A. A. Coelho. Whole powder pattern modelling macros for TOPAS. *Journal of Applied Crystallography*, 51(6):1752–1765, Dec 2018.

Publications in preparation:

1. C. Perez-Demydenko, B. Mukherjee, S. Siboni & P. Scardi. Mean square strain invariant expressions for all Laue classes.
2. C. Perez-Demydenko, A. Flor & P. Scardi. Temperature Diffuse Scattering of nanocrystals: comparison with Molecular Dynamic simulations.
3. A. Flor, C. Perez-Demydenko & P. Scardi. Inhomogeneous strain in nanocrystalline powders by diffraction line profile analysis.

Events participation:

1. Conference 100 years of the Debye Scattering Equation. Italy, 2015. Poster presentation. *X-DREAM: the evolution of the WPPM approach for size-strain analysis*.
2. Conference Size-Strain VII. UK, 2015. Poster presentation. *X-DREAM: the evolution of the WPPM approach for size-strain analysis*.
3. Conference 15 th European Powder Diffraction Conference. Italy 2016. Oral presentation. *Line broadening effect of nanocrystals surface*.

Contents

1	Introduction	14
2	Scattered intensity in reciprocal space by a particle	17
2.1	Scattered intensity in reciprocal space from a distorted domain with thermal vibrations	17
2.2	The Bragg intensity	20
2.3	The TDS intensity	22
2.4	The Debye equation for the total intensity	25
2.5	The powder average	26
3	The Whole Powder Pattern Modelling approach	30
3.1	The projected length variation	30
3.2	The transformations of the projected length variation	33
3.3	Peak profile construction with the WPPM approach	36
4	Diffraction peak profiles of surface relaxed spherical nanocrystals	49
4.1	Lattice distortion of nanoparticles due to Surface Relaxation	50
4.2	A displacement field due to the Surface Relaxation phenomenon	53
4.3	The coordination contribution	55
4.4	The elastic contribution	58
4.5	The Fourier Transform components for the peak profile due to the Surface Relaxation phenomenon	61
4.6	Surface Relaxation macro for <i>TOPAS</i>	72

4.7	Molecular Dynamics simulations setup	72
4.8	Test of the Surface Relaxation model	75
5	Thermal Diffuse Scattering in nanoparticles	80
5.1	The Vibrational Density of States in nanoparticles	81
5.2	The Debye-Waller exponent of nanoparticles	85
5.3	The first-order TDS in reciprocal space	88
5.4	The first order powder TDS	92
5.5	Higher order TDS	94
5.6	Powder TDS calculation from a Molecular Dynamics vibration trajectory	100
5.7	Beyerlein et. al. TDS model test	105
6	Invariant forms of microstrain	113
6.1	Microstrain effect on line broadening	114
6.2	Invariant forms for strain anisotropy	116
6.2.1	Triclinic crystal system (S.G. 1,2)	117
6.2.2	Monoclinic crystal system (S.G. 3-15)	117
6.2.3	Orthorhombic crystal system (S.G. 16-74)	118
6.2.4	Tetragonal crystal system (S.G. 75-142)	118
6.2.5	Trigonal crystal system (S.G. 143-167)	119
6.2.6	Hexagonal crystal system (S.G. 168-194)	121
6.2.7	Cubic crystal system (S.G. 195-230)	121
7	Conclusions	127
A	Analytical definitions of the F_i and G_i functions in the ex- pressions of $\langle \Delta L(L) \rangle$ and $\langle \Delta L^2(L) \rangle$ of the surface relaxation model in Chapter 4	131

List of Figures

2.1	The tangent plane approximation	29
3.1	Definition of the Projected Length Variation	31
3.2	Atomic configurations in a general distortion problem . . .	32
3.3	The reciprocal basis convenient to find the peak profile expression with the WPPM approach	42
4.1	Atomic displacements due to the Surface Relaxation phenomenon	54
4.2	Sub-coordination component of the displacement field in a nanoparticle	56
4.3	Model for the response of a spherical nanoparticle subject to an external hydrostatic pressure	59
4.4	Carved bar subject to a longitudinal pressure	60
4.5	Diagram for the orthorhombic basis in cubic materials . . .	62
4.6	Change of basis from a Cartesian coordinate system to cylindrical and polar systems	67
4.7	Geometrical construction for the calculation of $\langle \Delta L \rangle$ and $\langle \Delta L^2 \rangle$	69
4.8	<i>TOPAS</i> macro WPPM_SR_Sphere	73
4.9	Macro call example for macro WPPM_SR_Sphere	74
4.10	Inverse proportionality between effective pressure and nanoparticle radius	75
4.11	XRPD patterns for Pd, Ag and Pb spherical nanoparticles .	78
4.12	Scaled atomic displacements projected in the 100 plane for some Pb spherical particles	79

4.13	Warren plots and $\langle \Delta L \rangle$ distribution along [111] for a Ag nanoparticle of radius 4.9 nm	79
5.1	Hollow spherical region where the TDS intensity is concentrated	91
5.2	Unit sphere surface tessalation with the HEALPix method, for order parameter $n = 0, 1, 2$ and 3	102
5.3	Number of computation points for different maximum area elements with the HEALPix method	105
5.4	Fits of Pd particles TDS powder profile according to Beyerlein's model	106
5.5	Fits of Al particles TDS powder profile according to Beyerlein's model	107
5.6	Reciprocal space maps of the TDS, Bragg and total intensity of a Pd nanoparticle of diameter 12 unit cells	110
5.7	Reciprocal space maps of the TDS, Bragg and total intensity of a Pd nanoparticle of diameter 24 unit cells	111
6.1	<i>TOPAS</i> macro getInvariant (part 1 of 2)	125
6.2	<i>TOPAS</i> macro getInvariant (part 2 of 2)	126

List of Tables

4.1	Definition of the functions whose mean values are needed to compute $\langle \Delta L(L) \rangle$ and $\langle \Delta L^2(L) \rangle$	71
4.2	Values of parameters in eq. 4.10 after minimization of eq. 4.38 for nanoparticles of different metals and sizes	76
5.1	Number of neighbors and radius (in units of unit cell) of the inner coordination shells, for fcc and bcc metals	98
5.2	Parameters values from the TDS fits in Figures 5.4 and 5.5	108
6.1	Coefficients of the invariant form of the Miller indices for the different Laue classes (part 1 of 2)	122
6.2	Coefficients of the invariant form of the Miller indices for the different Laue classes (part 2 of 2)	123
6.3	Conversion from the E_i to the E_{hkl} coefficients notation, for all Laue classes and different settings	124
A.1	Explicit form of the G_1 , G_2 and G_3 functions of Table 4.1 .	131
A.2	Explicit form of the G_4 function of Table 4.1	131
A.3	Explicit form of the F_i functions, $i = 1, 2, \dots, 6$, of Table 4.1	132
A.4	Explicit form of the F_7 , F_8 and F_9 functions of Table 4.1 as well as of F_{10a} (part 1 of 2)	132
A.5	Explicit form of the F_7 , F_8 and F_9 functions of Table 4.1 as well as of F_{10a} (part 2 of 2)	132
A.6	Explicit form of the F_{10b} function (part 1 of 2)	132
A.7	Explicit form of the F_{10b} function (part 2 of 2)	133

Chapter 1

Introduction

X-ray diffraction (XRD) is one of the most used techniques in materials science. The greatest strength comes from the possibility of knowing how atoms are arranged, if in an ordered or disordered way, in a given material. With this information, the use of current theoretical knowledge in physics, chemistry and mathematics, as well as computational resources, allows investigations and estimates of most physical property. Despite being a mature technique, which has been growing and used since 1912, XRD is not yet fully exploited in its full potential. For example, many scientists still use old approaches, like those based on the Scherrer formula and the Williamson-Hall method, to characterize a material from the microstructural point of view. The prevalence of these methods over time stems from their mathematical simplicity; in spite of coarse simplifications and underlying hypotheses of limited validity, these simplified methods have often been deemed appropriate to provide estimates of basic parameters, like mean crystalline domain size and degree of lattice distortion. More sophisticated methods though, have been proposed in time. Starting from the '40s of past century, several scientists, among which A.J.C. Wilson and B.E. Warren, gave significant contributions to methods providing deeper insights and more reliable information, like particle shape and size distribution, and direction dependent lattice distortion. Even if computational resources nowadays available can easily implement the methods proposed by Wilson, Warren and all their epigones, these methods are still rarely used by material scientists. Their low popularity is mainly due to lim-

itations in the existing literature, especially concerning textbooks, and scarcity of software specially devoted to the analysis of powder diffraction patterns for the study of the microstructure, as other do for the structure (Rietveld analysis) of materials. The present thesis is a contribution to close this gap between potentiality of slightly used XRD methods and actual applications, with a contribution dedicated to the study of the static and dynamic disorder in nanocrystalline materials.

Related to the modern and most complete methods of microstructural analysis, we present here a clearer fundamental derivation of the expressions underlying the Whole Powder Pattern Modelling (WPPM) approach [1]. After reviewing the expressions for the scattered intensity in reciprocal space in Chapter 2, the fundamental concept of Projected Length Variation (PLV) is presented in Chapter 3, as a mean for a modern representation of the microstrain introduced by Warren. One of the most powerful methods for simulating diffraction patterns, and thus for testing microstrain models, is currently the use of the Debye equation over relaxed atomic configurations obtained, e.g., by Molecular Dynamics or other atomistic modelling. To properly link the distorted atomic configuration from which the patterns are computed, with the corresponding one used by the WPPM approach, the transformation laws of the mean PLVs are deduced and discussed in detail in the present thesis. As a straightforward application of the theory exposed in the previous chapter, Chapter 4 considers the static disorder caused by the Surface Relaxation phenomena; a peak profile model is proposed, based on three parameters with a clear physical meaning. The model involves peak asymmetry, which for the first time is modelled by an imaginary component of the Fourier Transform within the WPPM approach. Following in the path of the Debye equation use over atomic configuration, in Chapter 5 we present a software for computing the Thermal (or Temperature) Diffuse Scattering (TDS) in powder patterns, based on Molecular Dynamics trajectories. The software discretizes homogeneously the surface of spheres in reciprocal space to compute the scattered intensity over them, before making the powder diffraction average. In this way homogeneity in the density of points

contributing to the powder intensity is guaranteed, as opposed to other approaches that compute intensity in a homogeneous three dimensional grid in reciprocal space. Numerical TDS profiles carrying the dynamic disorder of nanoparticles are then used to test existing analytical models of vibrational properties at this scale. Last, in Chapter 6 we consider the hkl dependence of the squared microstrain, in the form of “invariant” expressions proposed by Popa [2]. Popa’s expressions are reviewed and, where necessary, corrected; additional expressions are proposed to deal with alternative crystallographic settings.

Regarding the software implementing modern Line Profile Analysis methods, in the present thesis we present new macros for *TOPAS* (a popular software for the analysis of diffraction patterns based on the Rietveld method) for the construction of peak profiles according to the WPPM approach. A macro implementing corrected and augmented invariant expressions of Popa is also presented.

The author hopes this thesis to be a convenient starting point of studies and further applications of the WPPM approach and the influence of thermal vibrations in X-ray powder patterns. This is especially evident in the first part, where basic concepts and needed physical approximations are illustrated, all reported with a clear mathematical deduction of all the expressions. The seminal works of B. E. Warren are here revived and valorized, as good reference readings to future students and scientists interested in the field of X-ray diffraction and its applications.

Chapter 2

Scattered intensity in reciprocal space by a particle

2.1 Scattered intensity in reciprocal space from a distorted domain with thermal vibrations

The instantaneous scattered intensity at reciprocal space point \mathbf{s} , from a crystallite where atoms occupy instantaneous positions \mathbf{R}_l and have atomic scattering factor f_l , is given by [3]:

$$I(\mathbf{s}) = I_e \sum_l f_l \text{Exp}[2\pi i \mathbf{s} \cdot \mathbf{R}_l] \sum_{l'} f_{l'}^* \text{Exp}[-2\pi i \mathbf{s} \cdot \mathbf{R}_{l'}], \quad (2.1)$$

or simply by

$$I(\mathbf{s}) = I_e \mathbb{F} \mathbb{F}^*, \quad (2.2)$$

if we define an instantaneous “particle” structure factor as

$$\mathbb{F} = \sum_l f_l \text{Exp}[2\pi i \mathbf{s} \cdot \mathbf{R}_l]. \quad (2.3)$$

I_e is the intensity of classical scattering by a single free electron, or Thomson scattering, and carries the dependence on the distance between the

crystallite and the detector [3]¹. Any intensity in *electron units* refers to the same divided by the factor I_e .

Due to thermal vibrations, the instantaneous positions \mathbf{R}_l will vary, so we can express them as the sum of some mean position \mathbf{r}_l , constant for each atom, plus a displacement $\boldsymbol{\delta}_l$ varying with time, i.e. $\mathbf{R}_l = \mathbf{r}_l + \boldsymbol{\delta}_l$. What we observe experimentally is the time average of eq. 2.1, which then reads as [3]:

$$\begin{aligned} \langle I(\mathbf{s}) \rangle &= I_e \langle \mathbb{F}\mathbb{F}^* \rangle \\ &= I_e \sum_l \sum_{l'} f_l e^{2\pi i \mathbf{s} \cdot \mathbf{r}_l} f_{l'}^* e^{-2\pi i \mathbf{s} \cdot \mathbf{r}_{l'}} \langle \text{Exp}[2\pi i \mathbf{s} \cdot (\boldsymbol{\delta}_l - \boldsymbol{\delta}_{l'})] \rangle. \end{aligned} \quad (2.4)$$

For a small argument, the mean of the exponential term can be Taylor expanded around zero and approximated as

$$\begin{aligned} \langle \text{Exp}[2\pi i \mathbf{s} \cdot (\boldsymbol{\delta}_l - \boldsymbol{\delta}_{l'})] \rangle &\approx 1 + 2\pi i \langle \mathbf{s} \cdot (\boldsymbol{\delta}_l - \boldsymbol{\delta}_{l'}) \rangle - 2\pi^2 \langle [\mathbf{s} \cdot (\boldsymbol{\delta}_l - \boldsymbol{\delta}_{l'})]^2 \rangle \\ &= 1 - 2\pi^2 \langle [\mathbf{s} \cdot (\boldsymbol{\delta}_l - \boldsymbol{\delta}_{l'})]^2 \rangle \\ &\approx \text{Exp} \left\{ -\frac{1}{2} \langle [2\pi \mathbf{s} \cdot (\boldsymbol{\delta}_l - \boldsymbol{\delta}_{l'})]^2 \rangle \right\} \\ &= e^{-2\pi^2 \langle (\mathbf{s} \cdot \boldsymbol{\delta}_l)^2 \rangle} e^{-2\pi^2 \langle (\mathbf{s} \cdot \boldsymbol{\delta}_{l'})^2 \rangle} (1 + e^{4\pi^2 s^2 \langle u_{\hat{\mathbf{s}}l} u_{\hat{\mathbf{s}}l'} \rangle} - 1) \\ &\approx \langle e^{2\pi i \mathbf{s} \cdot \boldsymbol{\delta}_l} \rangle \langle e^{-2\pi i \mathbf{s} \cdot \boldsymbol{\delta}_{l'}} \rangle + \langle e^{2\pi i \mathbf{s} \cdot \boldsymbol{\delta}_l} \rangle \langle e^{2\pi i \mathbf{s} \cdot \boldsymbol{\delta}_{l'}} \rangle (e^{4\pi^2 s^2 \langle u_{\hat{\mathbf{s}}l} u_{\hat{\mathbf{s}}l'} \rangle} - 1), \end{aligned} \quad (2.5)$$

where $u_{\hat{\mathbf{s}}l}$ is the projection of the instantaneous displacement of atom l over $\hat{\mathbf{s}}$, $u_{\hat{\mathbf{s}}l} = \boldsymbol{\delta}_l \cdot \hat{\mathbf{s}}$. Note that in the last of eqs. 2.5 the second mean term has been written with negative sign in the exponential part. This can be done because the approximation that is being used in these equations is $\langle \text{Exp}[\pm i x] \rangle \approx \text{Exp}[-(1/2)\langle x^2 \rangle]$, when x has an even and narrow

¹Let the incident X-ray beam, or electromagnetic wave, have intensity $I_o = c/(8\pi)\langle E_o^2 \rangle$, where E_o is the amplitude (not magnitude or norm) of the electric field $\mathbf{E}_o(t)$. Then $I_e = I_o \kappa (k_1 + k_2 \cos^2 2\theta)/R^2$, where 2θ is the scattering angle, R is the crystallite-detector distance and $\kappa = e^4/(m^2 c^4) = 7.94 \cdot 10^{-30} \text{ m}^2$. The term $k_1 + k_2 \cos^2 2\theta$ is known as *polarization factor* in powder diffractometry. If a Cartesian coordinate system $C = \{\hat{\mathbf{i}}, \hat{\mathbf{j}}, \hat{\mathbf{k}}\}$ is chosen with the XY plane containing the incident beam, the crystallite and the detector, then $k_1 = \langle (E_o \hat{\mathbf{E}}_o \cdot \hat{\mathbf{k}})^2 \rangle / \langle E_o^2 \rangle$ and $k_2 = \langle (E_o \hat{\mathbf{E}}_o \cdot \hat{\mathbf{j}})^2 \rangle / \langle E_o^2 \rangle$. For an unpolarized incident beam (lab diffractometer) $k_1 = k_2 = 1/2$, whereas for a synchrotron source (polarized incident beam) $k_1 = 1$ and $k_2 = 0$ are desired.

distribution around zero. Substituting the result in eqs. 2.5 in eq. 2.4 and properly including time independent terms inside time average terms we have

$$\begin{aligned}
\langle I(\mathbf{s}) \rangle &= I_e \langle \mathbb{F} \mathbb{F}^* \rangle = I_e \sum_l \sum_{l'} \langle f_l e^{2\pi i \mathbf{s} \cdot (\mathbf{r}_l + \boldsymbol{\delta}_l)} \rangle \langle f_{l'}^* e^{-2\pi i \mathbf{s} \cdot (\mathbf{r}_{l'} + \boldsymbol{\delta}_{l'})} \rangle \\
&+ I_e \sum_l \sum_{l'} \langle f_l e^{2\pi i \mathbf{s} \cdot (\mathbf{r}_l + \boldsymbol{\delta}_l)} \rangle \langle f_{l'}^* e^{-2\pi i \mathbf{s} \cdot (\mathbf{r}_{l'} + \boldsymbol{\delta}_{l'})} \rangle (e^{4\pi^2 s^2 \langle u_{\mathbf{s}l} u_{\mathbf{s}l'} \rangle} - 1) \\
&= I_B(\mathbf{s}) + I_{TDS}(\mathbf{s}),
\end{aligned} \tag{2.6}$$

where we have made the definitions

$$I_B(\mathbf{s}) = I_e \sum_l \sum_{l'} \langle f_l e^{2\pi i \mathbf{s} \cdot (\mathbf{r}_l + \boldsymbol{\delta}_l)} \rangle \langle f_{l'}^* e^{-2\pi i \mathbf{s} \cdot (\mathbf{r}_{l'} + \boldsymbol{\delta}_{l'})} \rangle = I_e \langle \mathbb{F} \rangle \langle \mathbb{F}^* \rangle \tag{2.7}$$

$$I_{TDS}(\mathbf{s}) = I_e \sum_l \sum_{l'} \langle f_l e^{2\pi i \mathbf{s} \cdot (\mathbf{r}_l + \boldsymbol{\delta}_l)} \rangle \langle f_{l'}^* e^{-2\pi i \mathbf{s} \cdot (\mathbf{r}_{l'} + \boldsymbol{\delta}_{l'})} \rangle (e^{4\pi^2 s^2 \langle u_{\mathbf{s}l} u_{\mathbf{s}l'} \rangle} - 1). \tag{2.8}$$

Introducing the Debye-Waller *exponent*, $M_l = M_{\mathbf{s}l}$, and the Debye-Waller *factor*, $\text{Exp}[-M_l]$ as

$$e^{-M_l} \equiv \langle e^{\pm 2\pi i \mathbf{s} \cdot \boldsymbol{\delta}_l} \rangle \approx e^{-2\pi^2 \langle (\mathbf{s} \cdot \boldsymbol{\delta}_l)^2 \rangle} = e^{-2\pi^2 s^2 \langle u_{\mathbf{s}l}^2 \rangle} \tag{2.9}$$

$$M_l = 2\pi^2 s^2 \langle u_{\mathbf{s}l}^2 \rangle, \tag{2.10}$$

the intensities $I_B(\mathbf{s})$ and $I_{TDS}(\mathbf{s})$ can be expressed as [3]

$$\begin{aligned}
I_B(\mathbf{s}) &= I_e \sum_l \sum_{l'} f_l \langle e^{2\pi i \mathbf{s} \cdot \boldsymbol{\delta}_l} \rangle f_{l'} \langle e^{-2\pi i \mathbf{s} \cdot \boldsymbol{\delta}_{l'}} \rangle e^{2\pi i \mathbf{s} \cdot (\mathbf{r}_l - \mathbf{r}_{l'})} \\
&= I_e \sum_l \sum_{l'} f_l e^{-M_l} f_{l'}^* e^{-M_{l'}} e^{2\pi i \mathbf{s} \cdot (\mathbf{r}_l - \mathbf{r}_{l'})}
\end{aligned} \tag{2.11}$$

$$I_{TDS}(\mathbf{s}) = I_e \sum_l \sum_{l'} f_l e^{-M_l} f_{l'}^* e^{-M_{l'}} e^{2\pi i \mathbf{s} \cdot (\mathbf{r}_l - \mathbf{r}_{l'})} \left\{ e^{4\pi^2 s^2 \langle u_{\mathbf{s}l} u_{\mathbf{s}l'} \rangle} - 1 \right\}. \tag{2.12}$$

Equations 2.11 and 2.12 allow for estimating the relative contribution of the two intensity functions $I_B(\mathbf{s})$ and $I_{TDS}(\mathbf{s})$ to the total intensity $I(\mathbf{s})$,

at a reciprocal space point \mathbf{s} . Whereas I_B equally receive the contribution from all possible values of $\mathbf{r}_l - \mathbf{r}_{l'}$, I_{TDS} practically receive the contribution of only smalls $|\mathbf{r}_l - \mathbf{r}_{l'}|$, which is the minority of the cases [3]. This is due to the fact that for large $|\mathbf{r}_l - \mathbf{r}_{l'}|$, $\langle u_{\mathbf{s}l} u_{\mathbf{s}l'} \rangle \rightarrow 0$ as the vibrations of the atoms l and l' will be uncorrelated, making null the factor $\text{Exp}[4\pi^2 s^2 \langle u_{\mathbf{s}l} u_{\mathbf{s}l'} \rangle] - 1$. Therefore, at those points in reciprocal space where I_B reaches its maxima, I_{TDS} will be order of magnitude lower. I_B is known as the *Bragg intensity* at \mathbf{s} , whereas I_{TDS} as the *Temperature* or *Thermal Diffuse Scattering* (TDS) intensity, at the same point [3].

2.2 The Bragg intensity

The Bragg intensity will be concentrated in *clouds* around reciprocal lattice points \mathbf{s}_{hkl} [4, 5]. Thus it is common to express it as a sum of individual intensity distributions, being each not null only near some \mathbf{s}_{hkl} :

$$I_B(\mathbf{s}) = \sum_{hkl} I_{hkl}(\mathbf{s}). \quad (2.13)$$

Let's suppose the coherent diffraction domain has the form of a parallelepipedon, with N_1 , N_2 and N_3 unit cells along each of the vectors \mathbf{a}_1 , \mathbf{a}_2 and \mathbf{a}_3 defining the unit cell for it, and a basis D for the direct space. The Bragg intensity in this case, for a monatomic material, can be expressed as [3]:

$$I_B(\mathbf{s}) = I_e |F|^2 e^{-2M} \prod_{i=1}^{i=3} \frac{\sin^2 N_i \pi \mathbf{s} \cdot \mathbf{a}_i}{\sin^2 \pi \mathbf{s} \cdot \mathbf{a}_i}, \quad (2.14)$$

where F is the structure factor, without temperature correction, referred to the unit cell defined by the basis $D = \{\mathbf{a}_1, \mathbf{a}_2, \mathbf{a}_3\}$:

$$F = \sum_n f^2 \text{Exp}[2\pi i \mathbf{s} \cdot \mathbf{r}_n]. \quad (2.15)$$

Defining $I_o(\mathbf{s})$ as

$$I_o(\mathbf{s}) \equiv \sum_l \sum_{l'} \text{Exp}[2\pi i \mathbf{s} \cdot (\mathbf{r}_l - \mathbf{r}_{l'})], \quad (2.16)$$

we have from eq. 2.14 and eq. 2.11 that in a monatomic case

$$I_o(\mathbf{s}) = \frac{|F|^2}{f^2} \prod_{i=1}^{i=3} \frac{\sin^2 N_i \pi \mathbf{s} \cdot \mathbf{a}_i}{\sin^2 \pi \mathbf{s} \cdot \mathbf{a}_i}. \quad (2.17)$$

See that the structure factor F and the atomic scattering factor f are also evaluated at the observation point \mathbf{s} in this equation. For large N_i , we can use the Dirac's delta to make the approximation

$$\frac{1}{N_i} \frac{\sin^2 N_i \pi x}{\sin^2 \pi x} \approx \delta(x - n_j), \quad (2.18)$$

where n_j is any integer. This is because the left member of this equation will tend to infinity as x tends to n_j , while being normalized in a small interval around n_j . Using this approximation eq. 2.17 can be written as

$$I_o(\mathbf{s}) = \frac{|F|^2}{f^2} N_1 N_2 N_3 \delta(\mathbf{s} \cdot \mathbf{a}_1 - n_1) \delta(\mathbf{s} \cdot \mathbf{a}_2 - n_2) \delta(\mathbf{s} \cdot \mathbf{a}_3 - n_3). \quad (2.19)$$

Since $\mathbf{s} \cdot \mathbf{a}_i = s_i$ are nothing more than the components of the scattering vector \mathbf{s} in the basis D^* reciprocal to D , we can express eq. 2.19 as

$$\begin{aligned} I_o(\mathbf{s}) &= \frac{|F|^2}{f^2} N_1 N_2 N_3 \delta(s_1 - \mathbf{s}_{hkl} \cdot \mathbf{a}_1) \delta(s_2 - \mathbf{s}_{hkl} \cdot \mathbf{a}_2) \delta(s_3 - \mathbf{s}_{hkl} \cdot \mathbf{a}_3) \\ &= \frac{|F|^2}{f^2} N_1 N_2 N_3 v_b \delta^{(3)}(\mathbf{s} - \mathbf{s}_{hkl}), \end{aligned} \quad (2.20)$$

where \mathbf{s}_{hkl} is any reciprocal lattice vector, so $\mathbf{s}_{hkl} \cdot \mathbf{a}_i$ will be an integer always, and $v_b = \mathbf{b}_1 \cdot \mathbf{b}_2 \times \mathbf{b}_3$ is the volume of the unit cell of D^* .

2.3 The TDS intensity

From eqs. 2.11 and 2.12 the total, experimentally observed, intensity in reciprocal space for a monatomic material, $I(\mathbf{s})$, is given by [3]:

$$I(\mathbf{s}) = I_e f^2 e^{-2M} \sum_l \sum_{l'} e^{2\pi i \mathbf{s} \cdot (\mathbf{r}_l - \mathbf{r}_{l'})} \text{Exp}[4\pi^2 s^2 \langle u_{\hat{\mathbf{s}}l} u_{\hat{\mathbf{s}}l'} \rangle]. \quad (2.21)$$

The average $\langle u_{\hat{\mathbf{s}}l} u_{\hat{\mathbf{s}}l'} \rangle$ can be computed assuming some theory for the dynamics of the crystalline lattice. In the present work we will assume the Born-von Kármán theory, which correctly describes the thermal vibration of atoms in crystals [6]. According to this theory, atoms vibrate due to the superposition of independent plane waves having wavevectors $\mathbf{q} = (2\pi/\lambda)\hat{\mathbf{q}} = 2\pi\mathbf{g}$ and polarization direction $\hat{\mathbf{e}}_{\mathbf{q}j}$, with $j = 1, 2, 3$, so their displacements can be expressed as:

$$\delta_l = \sum_{\mathbf{g}j} a_{\mathbf{g}j} \hat{\mathbf{e}}_{\mathbf{g}j} \cos(\omega_{\mathbf{g}j} t - 2\pi \mathbf{g} \cdot \mathbf{r}_l - \varphi_{\mathbf{g}j}). \quad (2.22)$$

These are also known as a normal vibration modes, $\mathbf{q}j$ or $\mathbf{g}j$. The amplitude of the waves, $a_{\mathbf{g}j}$, and their phase, $\varphi_{\mathbf{g}j}$, are independent among them and among different waves $\mathbf{g}j$, and vary arbitrarily with time. If the vibration of the atoms in the particle is described by this theory, the average in eq. 2.21 can be expanded as:

$$\begin{aligned} \langle u_{\hat{\mathbf{s}}l} u_{\hat{\mathbf{s}}l'} \rangle &= \sum_{\mathbf{g}j} \sum_{\mathbf{g}'j'} (\hat{\mathbf{e}}_{\mathbf{g}j} \cdot \hat{\mathbf{s}}) (\hat{\mathbf{e}}_{\mathbf{g}'j'} \cdot \hat{\mathbf{s}}) \\ &\times \langle a_{\mathbf{g}j} \cos(\omega_{\mathbf{g}j} t - 2\pi \mathbf{g} \cdot \mathbf{r}_l - \varphi_{\mathbf{g}j}) a_{\mathbf{g}'j'} \cos(\omega_{\mathbf{g}'j'} t - 2\pi \mathbf{g}' \cdot \mathbf{r}_{l'} - \varphi_{\mathbf{g}'j'}) \rangle. \end{aligned} \quad (2.23)$$

Because of the independence of the phases $\varphi_{\mathbf{g}j}$ the means in this equation for $\mathbf{g}j \neq \mathbf{g}'j'$ will vanish, so we obtain

$$\begin{aligned}
\langle u_{\hat{\mathbf{s}}l} u_{\hat{\mathbf{s}}l'} \rangle &= \sum_{\mathbf{g}j} (\hat{\mathbf{e}}_{\mathbf{g}j} \cdot \hat{\mathbf{s}})^2 \langle a_{\mathbf{g}j}^2 \rangle \langle \cos(\omega_{\mathbf{g}j} t - 2\pi \mathbf{g} \cdot \mathbf{r}_l - \varphi_{\mathbf{g}j}) \\
&\quad \times \cos(\omega_{\mathbf{g}j} t - 2\pi \mathbf{g} \cdot \mathbf{r}_{l'} - \varphi_{\mathbf{g}j}) \rangle \\
&= \frac{1}{2} \sum_{\mathbf{g}j} (\hat{\mathbf{e}}_{\mathbf{g}j} \cdot \hat{\mathbf{s}})^2 \langle a_{\mathbf{g}j}^2 \rangle \{ \langle \cos[2\pi \mathbf{g} \cdot (\mathbf{r}_l - \mathbf{r}_{l'})] \rangle \\
&\quad + \langle \cos[2\omega_{\mathbf{g}j} t - 2\pi \mathbf{g} \cdot (\mathbf{r}_l + \mathbf{r}_{l'}) - 2\varphi_{\mathbf{g}j}] \rangle \} \\
&= \frac{1}{2} \sum_{\mathbf{g}j} (\hat{\mathbf{e}}_{\mathbf{g}j} \cdot \hat{\mathbf{s}})^2 \langle a_{\mathbf{g}j}^2 \rangle \cos[2\pi \mathbf{g} \cdot (\mathbf{r}_l - \mathbf{r}_{l'})].
\end{aligned} \tag{2.24}$$

Defining

$$G_{\mathbf{g}j} = 2\pi^2 s^2 (\hat{\mathbf{e}}_{\mathbf{g}j} \cdot \hat{\mathbf{s}})^2 \langle a_{\mathbf{g}j}^2 \rangle, \tag{2.25}$$

we then conclude that

$$4\pi^2 s^2 \langle u_{\hat{\mathbf{s}}l} u_{\hat{\mathbf{s}}l'} \rangle = \sum_{\mathbf{g}j} G_{\mathbf{g}j} \cos[2\pi \mathbf{g} \cdot (\mathbf{r}_l - \mathbf{r}_{l'})]. \tag{2.26}$$

Also, evaluating this equation for $l = l'$ and comparing with eq. 2.10 we obtain that the Debye-Waller exponent in the Born-von Kármán theory can be expressed as

$$M = \frac{1}{2} \sum_{\mathbf{g}j} G_{\mathbf{g}j}. \tag{2.27}$$

Substituting eq. 2.26 in eq. 2.21 we have

$$I(\mathbf{s}) = I_e f^2 e^{-2M} \sum_l \sum_{l'} e^{2\pi i \mathbf{s} \cdot (\mathbf{r}_l - \mathbf{r}_{l'})} e^{Y_{ll'}}, \tag{2.28}$$

with

$$Y_{ll'} = \sum_{\mathbf{g}j} G_{\mathbf{g}j} \cos[2\pi \mathbf{g} \cdot (\mathbf{r}_l - \mathbf{r}_{l'})]. \tag{2.29}$$

Making then a Taylor expansion $Y_{ll'} = 1 + Y_{ll'} + Y_{ll'}^2/2! + \dots Y_{ll'}^n/n!$ and changing to a more common index choice, the total intensity in eq. 2.28

can be expressed as

$$I(\mathbf{s}) = I_e f^2 e^{-2M} \sum_m \sum_n e^{2\pi i \mathbf{s} \cdot (\mathbf{r}_m - \mathbf{r}_n)} + \sum_{l=1}^{\infty} I_{TDSl}(\mathbf{s}), \quad (2.30)$$

where

$$I_{TDSl}(\mathbf{s}) = I_e f^2 e^{-2M} \sum_m \sum_n e^{2\pi i \mathbf{s} \cdot (\mathbf{r}_m - \mathbf{r}_n)} \frac{Y_{mn}^l}{l!}. \quad (2.31)$$

Comparing with eqs. 2.11 and 2.12 we then conclude that the TDS intensity in reciprocal space, $I_{TDS}(\mathbf{s})$, can be seen as the contribution of different l -order terms, known as l th-order thermal diffuse scattering, $I_{TDSl}(\mathbf{s})$:

$$I_{TDS}(\mathbf{s}) = \sum_{l=1}^{\infty} I_{TDSl}(\mathbf{s}). \quad (2.32)$$

In particular, using eqs. 2.16 and 2.29, the first order TDS of a monatomic material can be expressed in electron units as [3]:

$$\begin{aligned} I_1(\mathbf{s}) &= f^2 e^{-2M} \sum_m \sum_n \sum_{\mathbf{g}j} e^{2\pi i \mathbf{s} \cdot (\mathbf{r}_m - \mathbf{r}_n)} G_{\mathbf{g}j} \cos[2\pi \mathbf{g} \cdot (\mathbf{r}_m - \mathbf{r}_n)] \\ &= \frac{1}{2} f^2 e^{-2M} \sum_{\mathbf{g}j} G_{\mathbf{g}j} \sum_m \sum_n e^{2\pi i \mathbf{s} \cdot (\mathbf{r}_m - \mathbf{r}_n)} \left\{ e^{2\pi i \mathbf{g} \cdot (\mathbf{r}_m - \mathbf{r}_n)} \right. \\ &\quad \left. + e^{-2\pi i \mathbf{g} \cdot (\mathbf{r}_m - \mathbf{r}_n)} \right\} \\ &= \frac{1}{2} f^2 e^{-2M} \sum_{\mathbf{g}j} \{I_o(\mathbf{s} + \mathbf{g}) + I_o(\mathbf{s} - \mathbf{g})\}. \end{aligned} \quad (2.33)$$

Summarizing, in this work we express the total observed intensity in reciprocal space as

$$\begin{aligned} I(\mathbf{s}) &= I_B(\mathbf{s}) + I_{TDS}(\mathbf{s}) \\ &= I_B(\mathbf{s}) + \sum_{l=1}^{\infty} I_{TDSl}(\mathbf{s}), \end{aligned} \quad (2.34)$$

where $I_B(\mathbf{s})$ is given by the first term in the right member of eq. 2.30, and $I_{TDSl}(\mathbf{s})$ is given by eq. 2.31, both for a monatomic case. Last but

not least, note that from eqs. 2.6 and 2.7 we can obtain a very compact and convenient way for expressing the TDS intensity in reciprocal space, in electron units [7, 8]:

$$I_{TDS}(\mathbf{s}) = \langle |\mathbb{F}|^2 \rangle - |\langle \mathbb{F} \rangle|^2. \quad (2.35)$$

2.4 The Debye equation for the total intensity

The instantaneous intensity at reciprocal space point \mathbf{s} , scattered by a particle, is given by eq. 2.1, which can be written as

$$I(\mathbf{s}) = \sum_m \sum_n f_m f_n \text{Exp}[2\pi i \mathbf{s} \cdot \mathbf{r}_{mn}], \quad (2.36)$$

where \mathbf{r}_{mn} is the vector separation between atoms m and n , $\mathbf{r}_{mn} = \mathbf{r}_m - \mathbf{r}_n$. If we have M *identical* particles diffracting together, for instance, in a powder sample, the intensity at \mathbf{s} will then be given by

$$I(\mathbf{s}) = \sum_{i=1}^M \sum_m \sum_n f_m f_n \text{Exp}[2\pi i \mathbf{s} \cdot \mathbf{r}_{mn}^i] = \sum_m \sum_n f_m f_n \sum_{i=1}^M \text{Exp}[2\pi i \mathbf{s} \cdot \mathbf{r}_{mn}^i], \quad (2.37)$$

where \mathbf{r}_{mn}^i is the \mathbf{r}_{mn} vector of the i th particle. For any pair (m, n) the sum over M in eq. 2.37 will be equal to M times the mean value of the magnitude we are summing up, so we can write

$$I(\mathbf{s}) = M \sum_m \sum_n f_m f_n \langle \text{Exp}[2\pi i \mathbf{s} \cdot \mathbf{r}_{mn}^i] \rangle_i. \quad (2.38)$$

If the particles do not have any preferred orientation and there are many of them (*powder sample* condition), the mean in this equation can be approximated by the mean of the function $\text{Exp}[2\pi i \mathbf{s} \cdot \mathbf{r}_{mn}]$, when \mathbf{s} is fixed and \mathbf{r}_{mn} takes all orientations relative to it, while having constant modulus. This is a mathematical trick that will be applied many times in this work. Orienting \mathbf{s} as the z -axis and using a spherical coordinate

system we therefore write

$$\begin{aligned}
I(\mathbf{s}) &= M \sum_m \sum_n f_m f_n \langle \text{Exp}[2\pi i \mathbf{s} \cdot \mathbf{r}_{mn}^i] \rangle_i \\
&\approx M \sum_m \sum_n f_m f_n \langle \text{Exp}[2\pi i s r_{mn} \cos \theta] \rangle \\
&= M \sum_m \sum_n f_m f_n \frac{1}{4\pi r_{mn}^2} \int_0^\pi \int_0^{2\pi} \text{Exp}[2\pi i s r_{mn} \cos \theta] r_{mn}^2 \sin \theta \, d\theta \, d\phi.
\end{aligned} \tag{2.39}$$

Solving the integral in eq. 2.39 we obtain

$$I(\mathbf{s}) = I(s) = M \sum_m \sum_n f_m f_n \frac{\sin(2\pi s r_{mn})}{2\pi s r_{mn}}. \tag{2.40}$$

Equation 2.40 is the celebrated *Debye scattering equation* [9, 3]. The factor M is usually omitted. This equation provides the *total* intensity at any point of reciprocal space, when practicing diffraction over a powder sample of identical particles, provided atoms' position, or pair distances r_{mn} , are known. Note that it is a function of $s \equiv \|\mathbf{s}\|$, so it is constant over a sphere of radius s in reciprocal space. We will call this sphere an s -sphere, though the terms *diffraction* or *reflection* sphere are more common in the literature.

2.5 The powder average

Let's suppose that we study the diffraction of a beam of X-rays having incident and scattered direction $\hat{\mathbf{s}}_o$ and $\hat{\mathbf{s}}$, respectively. The observed scattered intensity will be that at a point

$$\mathbf{s} = \frac{\hat{\mathbf{s}} - \hat{\mathbf{s}}_o}{\lambda}, \tag{2.41}$$

of reciprocal space. Since the intensity in reciprocal space tends to be concentrated around reciprocal lattice points \mathbf{s}_{hkl} , in a single crystal diffraction experiment diffraction will occur with appreciable intensity only through

certain directions $\hat{\mathbf{s}}$. Therefore we will observe or measure spots in a diffraction pattern. When we practice diffraction over a powder sample, on the other hand, the whole single crystal reciprocal space intensity map given by eq. 2.36, $I_{sc}(\mathbf{s})$, will pivot around the reciprocal space origin, due to the different orientations of the M crystallites composing the sample. The powder sample condition establishes that there are no preferred orientations for the crystallites in the sample. This implies that the intensity at point \mathbf{s} given by eq. 2.41, will be the sum of I_{sc} at M points homogeneously distributed over the surface of a sphere in reciprocal space of radius $s \equiv \|\mathbf{s}\|$, i.e. an s -sphere. According to eq. 2.41, the points at a constant angular position respect to the incident beam direction, $\hat{\mathbf{s}}_o$, over the Ewald sphere, have the same $\|\mathbf{s}\|$. The geometric place of those points will be the intersection of the Ewald sphere and the s -sphere. We call this an s -circle. If the powder condition holds, we conclude that the intensity $I(s)$ scattered through any point of an s -circle is the same. From what has been said, we can express $I(s)$ as a sum over the reciprocal space points in the s -sphere, which in turn can be approximated as an integral with a density function $M/(4\pi s^2)$:

$$\begin{aligned}
 I(s) &= \sum_{i=1}^M I_{sc}(\mathbf{s}_i) \\
 &\approx \frac{M}{4\pi s^2} \iint_{s\text{-sphere}} I_{sc}(\mathbf{s}) d^2\mathbf{s}.
 \end{aligned}
 \tag{2.42}$$

Equation 2.42 is called the *powder average*. It clearly says that the diffracted intensity at an angle 2θ , related to s as $s = 2 \sin \theta / \lambda$, will be the average of the intensity over a reciprocal space sphere of radius s , multiplied by the number of crystallites in the sample. This is a very simple but important result, used by all peak profiles models that first compute intensity in reciprocal space in correspondence with physical phenomena. Note that if we have the intensity in reciprocal space expressed as the sum of different “types” of intensities, this equation allows for finding the corresponding contribution to the powder intensity, $I(s)$, of each of them. This is a key

difference with the Debye equation, which always gives the total powder intensity at any s . Therefore, if $I_{sc}(\mathbf{s})$ is the total intensity at \mathbf{s} , and all particles in the powder sample are identical, from eq. 2.40 we have

$$I(s) \approx \frac{M}{4\pi s^2} \iint_{s\text{-sphere}} I_{sc}(\mathbf{s}) d^2\mathbf{s} \equiv M \sum_m \sum_n f_m f_n \frac{\sin(2\pi s r_{mn})}{2\pi s r_{mn}}. \quad (2.43)$$

The equivalence in eq. 2.43 can be deduced from eq. 2.39 exchanging r_{mn} with s , which would give the same result of the integration:

$$\begin{aligned} I(\mathbf{s}) &= M \sum_m \sum_n f_m f_n \frac{1}{4\pi s^2} \int_0^\pi \int_0^{2\pi} \text{Exp}[2\pi i s r_{mn} \cos \theta] s^2 \sin \theta d\theta d\phi \\ &= \frac{M}{4\pi s^2} \iint_{s\text{-sphere}} \sum_m \sum_n f_m f_n \text{Exp}[2\pi i \mathbf{s} \cdot \mathbf{r}_{mn}] d^2\mathbf{s} \\ &= \frac{M}{4\pi s^2} \iint_{s\text{-sphere}} I_{sc}(\mathbf{s}) d^2\mathbf{s}. \end{aligned} \quad (2.44)$$

Let's call Ω^{hkl} the region in reciprocal space where the Bragg intensity cloud of reciprocal space point \mathbf{s}_{hkl} is. Let's also call Ω_s^{hkl} the intersection of the s -sphere with Ω^{hkl} . Substituting equations 2.34 and 2.13 in eq. 2.42 and omitting the sub-index sc for clarity, we obtain the Bragg-only intensity at s :

$$I(s) = \sum_{hkl} I_{hkl}(s), \quad (2.45)$$

with

$$I_{hkl}(s) = \frac{M}{4\pi s^2} \iint_{\Omega_s^{hkl}} I_{hkl}(\mathbf{s}) d^2\mathbf{s}. \quad (2.46)$$

The integration in eq. 2.46 is challenging, unless for the case of a spherical crystallite, in which $I_{hkl}(\mathbf{s})$ has spherical symmetry around \mathbf{s}_{hkl} [10]. A useful simplification which is acceptable for not too small crystalline domains (not too big Ω_s^{hkl}) is the *tangent plane approximation* illustrated in Figure 2.1 [11, 12]. Let's call $\Omega_{s\hat{\mathbf{s}}_{hkl}}^{hkl}$ the intersection with Ω^{hkl} of a plane

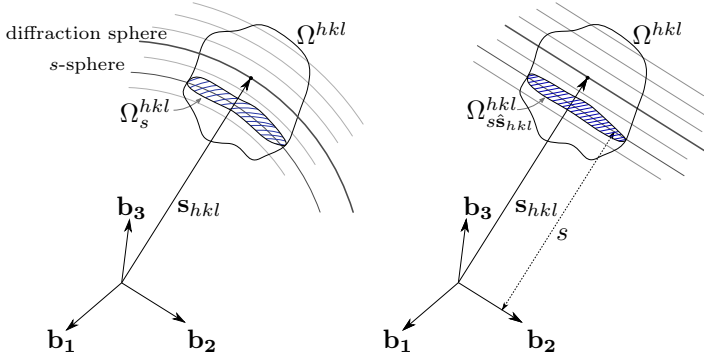


Figure 2.1: The tangent plane approximation. Ω_s^{hkl} is the intersection between Ω^{hkl} and an s -sphere, whereas $\Omega_{s\hat{\mathbf{s}}_{hkl}}^{hkl}$ is the intersection of Ω^{hkl} with a plane perpendicular to \mathbf{s}_{hkl} , at distance s from the origin.

perpendicular to $\hat{\mathbf{s}}_{hkl}$ and at distance s from the origin. If the dimensions of Ω^{hkl} are small compared with the length of \mathbf{s}_{hkl} , we can approximate the integration over Ω_s^{hkl} by an integration over $\Omega_{s\hat{\mathbf{s}}_{hkl}}^{hkl}$ and write eq. 2.46 as

$$I_{hkl}(s) \approx \frac{M}{4\pi s^2} \iint_{\Omega_{s\hat{\mathbf{s}}_{hkl}}^{hkl}} I_{hkl}(\mathbf{s}) d^2\mathbf{s}. \quad (2.47)$$

Chapter 3

The Whole Powder Pattern Modelling approach

3.1 The projected length variation

A rigorous exposition of the Whole Powder Pattern Modelling (WPPM) approach is based on the concept of *Projected Length Variation* (PLV). Let's consider a region bounded by the surface Ω in the three dimensional space, in which a continuous vectorial deformation field $\mathbf{u} = \mathbf{u}(\mathbf{r})$ is defined. The projected length variation $\Delta L = \Delta L(\mathbf{r}, \hat{\mathbf{s}}, L)$ is defined as

$$\begin{aligned}\Delta L(\mathbf{r}, \hat{\mathbf{s}}, L) &= \{\mathbf{r} + L\hat{\mathbf{s}} + \mathbf{u}(\mathbf{r} + L\hat{\mathbf{s}}) - [\mathbf{r} + \mathbf{u}(\mathbf{r})]\} \cdot \hat{\mathbf{s}} - L \\ &= [\mathbf{u}(\mathbf{r} + L\hat{\mathbf{s}}) - \mathbf{u}(\mathbf{r})] \cdot \hat{\mathbf{s}},\end{aligned}\tag{3.1}$$

where L is a real number. If the direction (versor) $\hat{\mathbf{s}}$ is known from the context, we can shortly write $\Delta L(\mathbf{r}, L)$. From the formula and Figure 3.1 we can see that we are referring to the variation of the projection of the line segment between two points due to \mathbf{u} (usually two atomic positions or unit cell origins in a crystal, as shown later). For a specific line segment of length $|L|$ inside the particle, if $L > 0$ the PLV is equal to the variation of the $\hat{\mathbf{s}}$ -projected length of the segment, whereas for $L < 0$ it is equal to minus that variation. Let's call $\Omega_{-L\hat{\mathbf{s}}}$ the surface Ω displaced as $-L\hat{\mathbf{s}}$ ¹, and $\Omega_{-L\hat{\mathbf{s}}}^*$ the surface of the intersection region between Ω and $\Omega_{-L\hat{\mathbf{s}}}$,

¹ $\Omega_{-L\hat{\mathbf{s}}}$ is the "ghost" domain as termed in [13].

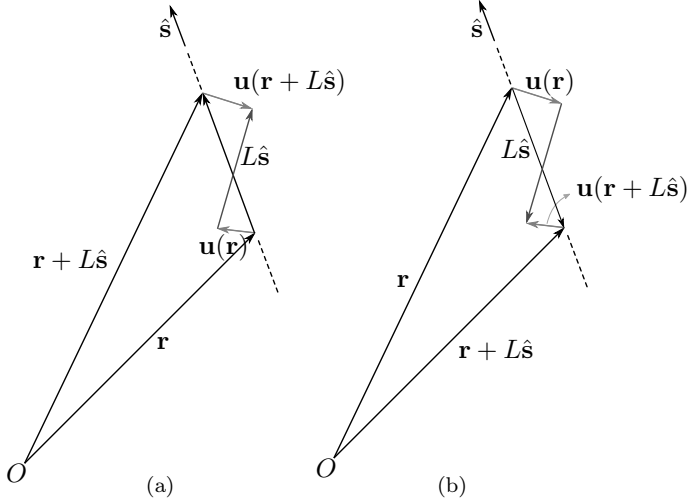


Figure 3.1: Definition of the Projected Length Variation. (a) A case where $L > 0$. (b) A case where $L < 0$.

$\Omega_{-L\hat{s}}^* = \Omega \cap \Omega_{-L\hat{s}}$. Since both points \mathbf{r} and $\mathbf{r} + L\hat{s}$ in eq. 3.1 have to be in Ω , we conclude that $\Delta L(\mathbf{r}, \hat{s}, L)$ is defined only for $\mathbf{r} \in \Omega_{-L\hat{s}}^*$. The mean and mean square values of the PLV for a given L and \hat{s} are defined as:

$$\langle \Delta L(\mathbf{r}, \hat{s}, L) \rangle_{\mathbf{r} \in \Omega_{-L\hat{s}}^*} \quad (3.2)$$

$$\langle \Delta L^2(\mathbf{r}, \hat{s}, L) \rangle_{\mathbf{r} \in \Omega_{-L\hat{s}}^*} \equiv \langle [\Delta L(\mathbf{r}, \hat{s}, L)]^2 \rangle_{\mathbf{r} \in \Omega_{-L\hat{s}}^*}. \quad (3.3)$$

By omitting the projection direction, as well as \mathbf{r} , since by definition it should be $\mathbf{r} \in \Omega_{-L\hat{s}}^*$, eqs. 3.2 and 3.3 can be written shortly as

$$\langle \Delta L(L) \rangle_{\Omega} \quad (3.4)$$

$$\langle \Delta L^2(L) \rangle_{\Omega}. \quad (3.5)$$

Note that for a fixed projection direction $\langle \Delta L(-L) \rangle_{\Omega} = -\langle \Delta L(L) \rangle_{\Omega}$ whereas $\langle \Delta L^2(-L) \rangle_{\Omega} = \langle \Delta L^2(L) \rangle_{\Omega}$. The (L, Ω) pair in eqs. 3.4 and 3.5 means that the terminal points of the examined line segments of length $|L|$, are initially

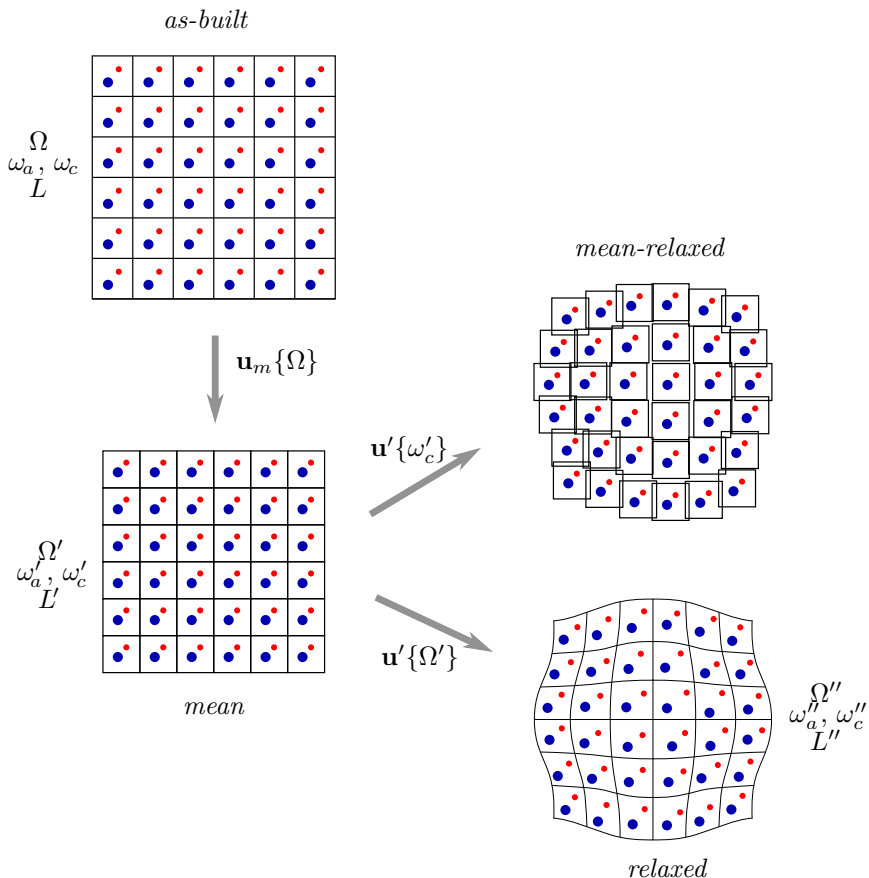


Figure 3.2: Atomic configurations in a general distortion problem. Blue and red circles represent atoms, and black squares represent unit cells. The relative atomic positions in the *mean* and *mean-relaxed* configurations can be slightly different. See text for details.

(before the deformation) points inside the surface Ω . It also emphasizes that the particular deformation field to be used in the computation of the average $\langle \dots \rangle$ should be that defined in all points of Ω .

3.2 The transformations of the projected length variation

In a general nanoparticle distortion problem, provided atoms do not “disappear”² we can distinguish among four different atomic configurations, as shown in Figure 3.2:

- The *as-built* configuration: where atoms occupy positions corresponding to a particle carved from a perfect, infinite structure.
- The *mean* configuration: a configuration obtained from the as-built by a simple shrinkage or expansion.
- The *mean-relaxed*: a configuration obtained from the mean one through small displacements at the unit cell level.
- The *relaxed* configuration: the “real” atomic configuration for the particle, obtained from the as-built or mean configurations through displacements at the atomic level.

The common scope of structure solution in X-ray diffraction experiments is to determine the unit cell parameters of the *mean* or *mean-relaxed configuration*, as well as characterize the content of the latter (atomic positions, occupancy factors, electronic distribution ecc.). The microstructural analysis, being linked to the Line Profile Analysis (LPA), of which the WPPM approach is part, is concerned about the distortion present in the *mean-relaxed* configuration.

Let’s define Ω as the surface delimiting the region in space in which the as-built configuration is. We will consider a nanoparticle distortion defined by the deformation field \mathbf{u} , such that Ω is transformed into Ω'' (see Figure 3.2). In operational form we write this as $\mathbf{u}\{\Omega\} = \Omega''$, with \mathbf{u} defined for all points inside Ω . In correspondence with the different types of atomic configurations introduced before, we can split the distortion

²As it is the case for planar defects and dislocations, where we talk in terms of missing planes or half plane in a stacking, respectively, with respect to a reference perfect crystal.

caused by \mathbf{u} into two successive distortions given, respectively, by two displacement fields \mathbf{u}_m and \mathbf{u}' . The displacement field \mathbf{u}_m will transform the as-built configuration into the mean one, doing $\mathbf{u}_m\{\Omega\} = \Omega'$. Then \mathbf{u}' will transform the mean configuration into the relaxed one, doing $\mathbf{u}'\{\Omega'\} = \Omega''$. In one equation we can state this as $\mathbf{u}'\{\mathbf{u}_m\{\Omega\}\} = \Omega''$. Looking at the atoms (a) and unit cells origins (c) in our piece of matter, they occupy particular positions ω_a and ω_c in Ω , which are transformed first to ω'_a and ω'_c positions in Ω' and then to ω''_a and ω''_c positions in Ω'' , respectively. So we can also write for them $\mathbf{u}'\{\mathbf{u}_m\{\omega_a\}\} = \omega''_a$ and $\mathbf{u}'\{\mathbf{u}_m\{\omega_c\}\} = \omega''_c$. For the cases of interest in this work, the number of atoms or unit cells in any Ω will be large. Thus, using the notation of eqs. 3.4 and 3.5 we can assume

$$\langle \Delta L(L') \rangle_{\Omega'} \approx \langle \Delta L(L') \rangle_{\omega'_c} \quad (3.6)$$

$$\langle \Delta L(L) \rangle_{\Omega} \approx \langle \Delta L(L) \rangle_{\omega_a}, \quad (3.7)$$

and the same for the corresponding mean square PLVs. The left members in eqs. 3.6 and 3.7 can be evaluated through integrals, since the involved displacement fields are continuous. The right members nevertheless, can only be evaluated through sums, since they are referred to discrete sets of points (unit cells origin and atomic positions).

Equations eqs. 3.6 and 3.7 are very important, since they allow for the construction of peak profiles in the WPPM approach using data from Molecular Dynamics (MD) atomistic simulations. These simulations can provide a realistic version of the atomic configuration of a whole nanoparticle, yielding $\langle \Delta L(L) \rangle_{\omega_a}$ and $\langle \Delta L^2(L) \rangle_{\omega_a}$. As shown later, WPPM needs $\langle \Delta L(L') \rangle_{\omega'_c}$ and $\langle \Delta L^2(L') \rangle_{\omega'_c}$. Therefore, if we find the relation between $\langle \Delta L(L') \rangle_{\Omega'}$ and $\langle \Delta L(L) \rangle_{\Omega}$ (the left members of eqs. 3.6 and 3.7), and the corresponding mean square magnitudes, we will also have the relations between the PLVs we can get from MD simulations and the PLVs we need for the WPPM approach. Below we derive these relations for a material of cubic symmetry.

According to what has been said, the total displacement field \mathbf{u} trans-

forming Ω into Ω'' can be expressed as

$$\mathbf{u}(\mathbf{r}) = \mathbf{u}_m(\mathbf{r}) + \mathbf{u}'(\mathbf{r} + \mathbf{u}_m(\mathbf{r})). \quad (3.8)$$

If a is the bulk lattice parameter and a' is the lattice parameter of the mean and mean-relaxed configurations, found after the indexing of the diffraction pattern, to be compatible with a simple shrinkage or expansion of the lattice, $\mathbf{u}_m(\mathbf{r})$ should be given by

$$\mathbf{u}_m(\mathbf{r}) = \left(\frac{a'}{a} - 1 \right) \mathbf{r} = \alpha \mathbf{r}, \quad (3.9)$$

so

$$\mathbf{u}(\mathbf{r}) = \alpha \mathbf{r} + \mathbf{u}'(\mathbf{r} + \mathbf{u}_m(\mathbf{r})). \quad (3.10)$$

Writing eq. 3.10 also for argument $\mathbf{r} + L\hat{\mathbf{s}}$, subtracting both equations and taking the scalar product with $\hat{\mathbf{s}}$ of both members of the obtained difference, we have

$$[\mathbf{u}(\mathbf{r} + L\hat{\mathbf{s}}) - \mathbf{u}(\mathbf{r})] \cdot \hat{\mathbf{s}} = \alpha L + [\mathbf{u}'(\mathbf{r} + L\hat{\mathbf{s}} + \mathbf{u}_m(\mathbf{r} + L\hat{\mathbf{s}})) - \mathbf{u}'(\mathbf{r} + \mathbf{u}_m(\mathbf{r}))] \cdot \hat{\mathbf{s}}. \quad (3.11)$$

Noting the the difference in the arguments of \mathbf{u}' in the right member of this equation is

$$\mathbf{r} + L\hat{\mathbf{s}} + \mathbf{u}_m(\mathbf{r} + L\hat{\mathbf{s}}) - \mathbf{r} - \mathbf{u}_m(\mathbf{r}) = \frac{a'}{a} L\hat{\mathbf{s}}, \quad (3.12)$$

we can apply the definition of the PLV in eq. 3.1 to obtain

$$\begin{aligned} \Delta L(\mathbf{r}, \hat{\mathbf{s}}, L) &= \alpha L + \Delta L'(\mathbf{r} + \mathbf{u}_m(\mathbf{r}), \hat{\mathbf{s}}, \frac{a'}{a} L) \\ &= \alpha L + \Delta L'(\mathbf{r}', \hat{\mathbf{s}}, L'), \end{aligned} \quad (3.13)$$

where we have defined

$$\mathbf{r}' \equiv \mathbf{r} + \mathbf{u}_m(\mathbf{r}) \quad (3.14)$$

$$L' \equiv \frac{a'}{a} L. \quad (3.15)$$

We have temporarily marked the PLV in right member of eq. 3.13 with a prime (') to remind that it is computed with the displacement field \mathbf{u}' , as opposed to the PLV in the left member, which is to be computed with \mathbf{u} . It can be demonstrated that

$$\mathbf{u}_m\{\Omega_{-L\hat{s}}^*\} = \Omega_{-L'\hat{s}}^*, \quad (3.16)$$

i.e., image \mathbf{r}' will belong to $\Omega_{-L'\hat{s}}^*$ for any preimage \mathbf{r} in $\Omega_{-L\hat{s}}^*$, with the transformation defined by \mathbf{u}_m . Therefore, we can take the mean over $\mathbf{r} \in \Omega_{-L\hat{s}}^*$ of both members in eq. 3.13 to obtain

$$\langle \Delta L(L') \rangle_{\Omega'} = \langle \Delta L(L) \rangle_{\Omega} - \alpha L, \quad (3.17)$$

for any direction \hat{s} . Similarly, solving for $\Delta L'(\mathbf{r}', \hat{s}, L')$ in eq. 3.13, squaring both members and taking the same mean, we obtain

$$\langle \Delta L^2(L') \rangle_{\Omega'} = \langle \Delta L^2(L) \rangle_{\Omega} - 2\langle \Delta L(L) \rangle_{\Omega} \alpha L - \alpha^2 L^2. \quad (3.18)$$

Equations 3.17 and 3.18 are the relations we were looking for. It is important to remind that the L s in the right- and left- members of these equations are not strictly the same, but are related through the equation $L' = (\alpha + 1)L = (a'/a)L$. The maximum permitted for both depends upon the particular direction we are dealing with, but for L the limiting volume is Ω whereas for L' it is Ω' . Nevertheless, in most practical cases we will have $\alpha \ll 1$, so we can consider $L \approx L'$ and $\Omega \approx \Omega'$.

3.3 Peak profile construction with the WPPM approach

Let's suppose we have a powder sample in which atoms inside each coherent diffraction domain vibrate due to temperature, around mean positions slightly different from those they would if that domain were just carved from a perfect bulk structure. We refer to a *distorted domain* in which atoms are individually displaced from their bulk positions to new mean

positions, and there are no “missing” atoms, i.e we exclude the cases of faulting and dislocations ³. In what follows we will deduce the expression for the profile of a hkl Bragg peak in such scenario, highlighting the contributions from the coherent diffraction domain size and shape, as well as the *strain*, intended as a continuous, slowly varying deformation of a crystalline structure. We will closely follow previous analytical works by Warren and by Stokes & Wilson [3, 14, 15], but adding many additional explanations and adapting the notation to the present thesis.

The Bragg intensity in eq. 2.11 already considers atoms in a particle (coherent diffraction domain) with arbitrary mean positions \mathbf{r}_l , different from those they would have in an infinite, or perfect, crystalline structure. If the distortion at the atomic level varies smoothly inside the domain, we can approximate and “bin” it into distortions at a unit cell level, using a new unit cell. We mean to substitute the real particle by a *fictitious* one, where all unit cells are *identical* and have small displacements, *without rotations*, respect to the points of a lattice formed with their cell parameters. It can be seen that we are referring to the *mean-relaxed* atomic configuration, introduced in section 3.2 and Figure 3.2. Inside the mean-relaxed unit cell, atoms vibrate due to temperature around some mean positions \mathbf{r}_p , relative to the unit cell origin. In this context we can approximate the real mean position of atom l in eq. 2.11 by its position in the mean-relaxed configuration as

$$\mathbf{r}_l \approx \mathbf{R}_m + \mathbf{r}_p, \quad (3.19)$$

where $\mathbf{R}_m = m_1 \mathbf{a}_1 + m_2 \mathbf{a}_2 + m_3 \mathbf{a}_3$ is the position of the displaced unit cell m . By inserting eq. 3.19 into eq. 2.11 and replacing the sums over l s by sums over m s and p s we obtain

$$\begin{aligned} I(\mathbf{s}) &= I_e \sum_m \sum_{m'} \sum_p \sum_{p'} f_p e^{-M_p} f_{p'} e^{-M_{p'}} e^{2\pi i \mathbf{s} \cdot (\mathbf{R}_m - \mathbf{R}_{m'})} e^{2\pi i \mathbf{s} \cdot \mathbf{r}_p} e^{-2\pi i \mathbf{s} \cdot \mathbf{r}_{p'}} \\ &= I_e F^2 \sum_m \sum_{m'} e^{2\pi i \mathbf{s} \cdot (\mathbf{R}_m - \mathbf{R}_{m'})}, \end{aligned} \quad (3.20)$$

³For a rigorous treatment in the case of faulting see [4].

where

$$F = F_T(\mathbf{s}) = \sum_p f_p e^{-M_p} e^{2\pi i \mathbf{s} \cdot \mathbf{r}_p} \quad (3.21)$$

is the average unit cell temperature-corrected structure factor, evaluated at \mathbf{s} . Calling \mathbf{r}_m the position of the cell m in the mean configuration, and $\mathbf{u}'(\mathbf{r}_m)$ its displacement, we have that $\mathbf{R}_m = \mathbf{r}_m + \mathbf{u}'(\mathbf{r}_m)$. Equation 3.20 can then be written as

$$I(\mathbf{s}) = I_e F^2 \sum_m \sum_{m'} \text{Exp}[2\pi i \mathbf{s} \cdot (\mathbf{r}_m - \mathbf{r}_{m'})] \text{Exp}[2\pi i \mathbf{s} \cdot (\mathbf{u}'(\mathbf{r}_m) - \mathbf{u}'(\mathbf{r}_{m'}))]. \quad (3.22)$$

Note that since vectors $\mathbf{r}_m - \mathbf{r}_{m'}$ will not be parallel to \mathbf{s} in general, we can not substitute in eq. 3.22 a PLV, as defined in eq. 3.1.

Let's define the separation vectors $\mathbf{r} = \mathbf{r}_m - \mathbf{r}_{m'}$. Since they are vectors between unit cell origins, they will have integer components in the direct space basis $D = \{\mathbf{a}_1, \mathbf{a}_2, \mathbf{a}_3\}$ used for the mean configuration. Therefore, they will belong to the lattice $L_D = \{\mathbf{r} = u\mathbf{a}_1 + v\mathbf{a}_2 + w\mathbf{a}_3 \mid u, v, w \in \mathbb{Z}\}$. Let's also define

$$\delta(\mathbf{r}_{m'}, \mathbf{r}) = \delta(\mathbf{r}_{m'}, \mathbf{r}_m - \mathbf{r}_{m'}) = \mathbf{u}'(\mathbf{r}_m) - \mathbf{u}'(\mathbf{r}_{m'}). \quad (3.23)$$

Using these magnitudes, and recalling the surface, Ω' , and unit cell origins, ω'_c , of the mean configuration (see Figure 3.2), we can transform eq. 3.22 as:

$$I(\mathbf{s}) = I_e F^2 \sum_{\mathbf{r} \in L_D} \text{Exp}[2\pi i \mathbf{s} \cdot \mathbf{r}] \sum_{\mathbf{r}_{m'} \in \omega'_{c, -\mathbf{r}}} \text{Exp}[2\pi i \mathbf{s} \cdot \delta(\mathbf{r}_{m'}, \mathbf{r})], \quad (3.24)$$

where $\omega'_{c, -\mathbf{r}} = \Omega'_{-\mathbf{r}} \cap \omega'_c$, i.e. it is the subset of unit cell origins ω'_c which is inside Ω' and its ghost $\Omega'_{-\mathbf{r}}$. The number of vectors $\mathbf{r}_{m'} \in \omega'_{c, -\mathbf{r}}$ will be equal to the number of unit cells inside $\Omega'_{-\mathbf{r}}$. Since the condition for a cell to have a neighbor cell at \mathbf{r} relative to it is to be inside $\Omega'_{-\mathbf{r}}$, we have that the number of these $\mathbf{r}_{m'}$ vectors is also equal to the number of cell pairs separated a distance \mathbf{r} in the mean configuration, $N(\mathbf{r})$. Calling v_a the volume of the unit cell in L_D , $v_a = \mathbf{a}_1 \times \mathbf{a}_2 \cdot \mathbf{a}_3$, and $\sqrt{v} \Omega'_{-\mathbf{r}}$ the volume

of $\Omega_{-\mathbf{r}}^*$, $N(\mathbf{r})$ is given by:

$$N(\mathbf{r}) = \frac{v\Omega_{-\mathbf{r}}^*}{v_a} = N_{uc} \frac{v\Omega_{-\mathbf{r}}^*}{N_{uc}v_a} = N_{uc} CV_D(\mathbf{r}), \quad (3.25)$$

where $CV_D(\mathbf{r})$ is the Common Volume Function for the particle when using basis D [13, 16, 4], and N_{uc} is the number of unit cells it contains (cells in L_D having structure factor F). Using this quantity and labeling for the sake of clarity $\mathbf{r}_{m'}$ as \mathbf{r}_o , eq. 3.24 can be written as

$$I(\mathbf{s}) = I_e F^2 N_{uc} \sum_{\mathbf{r} \in L_D} CV_D(\mathbf{r}) \langle \text{Exp}[2\pi i \mathbf{s} \cdot \boldsymbol{\delta}(\mathbf{r}_o, \mathbf{r})] \rangle_{\mathbf{r}_o} \text{Exp}[2\pi i \mathbf{s} \cdot \mathbf{r}], \quad (3.26)$$

with

$$\boldsymbol{\delta}(\mathbf{r}_o, \mathbf{r}) = \mathbf{u}'(\mathbf{r}_o + \mathbf{r}) - \mathbf{u}'(\mathbf{r}_o). \quad (3.27)$$

In words, for a given separation distance between cells, \mathbf{r} , we consider the mean of the phase factor containing the relative inter-cells displacement $\boldsymbol{\delta}(\mathbf{r}_o, \mathbf{r})$ [13, 3]. In eq. 3.26 we have also omitted the domain covered by \mathbf{r}_o when doing the average, keeping in mind that it is $\omega_{c,-\mathbf{r}}^*$.

We are interested in the intensity around the reciprocal space point \mathbf{s}_{hkl} . If the spreading of such intensity is small compared with the length of \mathbf{s}_{hkl} we can approximate \mathbf{s} by \mathbf{s}_{hkl} in the dot product $\mathbf{s} \cdot \boldsymbol{\delta}(\mathbf{r}_o, \mathbf{r})$ [14]. Besides, expressing the observation point \mathbf{s} through its position \mathbf{s}_r relative to \mathbf{s}_{hkl} , $\mathbf{s} = \mathbf{s}_{hkl} + \mathbf{s}_r$ we have that $\mathbf{r} \cdot \mathbf{s} = \mathbf{r} \cdot \mathbf{s}_{hkl} + \mathbf{r} \cdot \mathbf{s}_r = n + \mathbf{r} \cdot \mathbf{s}_r$, where n is an integer number since $\mathbf{r} \in L_D$ and $\mathbf{s}_{hkl} \in L_{D^*}$. With these transformations we can write eq. 3.26 as

$$I_{hkl}(\mathbf{s}) = I_e F^2 N_{uc} \sum_{\mathbf{r} \in L_D} CV_D(\mathbf{r}) \langle \text{Exp}[2\pi i \mathbf{s}_{hkl} \cdot \boldsymbol{\delta}(\mathbf{r}_o, \mathbf{r})] \rangle_{\mathbf{r}_o} \text{Exp}[2\pi i \mathbf{s}_r \cdot \mathbf{r}], \quad (3.28)$$

where we have labeled the left member as $I_{hkl}(\mathbf{s})$ since now the intensity is referred to a position \mathbf{s}_r , relative to a specific reciprocal lattice point \mathbf{s}_{hkl} . The number of points $\mathbf{r} \in L_D$ inside the particle volume over which we are making the sum in eq. 3.28 is large, since the unit cell volume v_a is much smaller than the particle volume. Therefore we can approximate

the sum with an integration over the direct space $S_D = \{\mathbf{r} = x\mathbf{a}_1 + y\mathbf{a}_2 + z\mathbf{a}_3 \mid x, y, z \in \mathbb{R}\}$, with a number of points per unit volume given by $(1/v_a)d^3\mathbf{r}$:

$$I_{hkl}(\mathbf{s}) = \frac{I_e F^2 N_{uc}}{v_a} \iiint_{\mathbf{r} \in S_D} \text{CV}_D(\mathbf{r}) \langle \text{Exp}[2\pi i \mathbf{s}_{hkl} \cdot \boldsymbol{\delta}(\mathbf{r}_o, \mathbf{r})] \rangle_{\mathbf{r}_o} \text{Exp}[2\pi i \mathbf{s}_r \cdot \mathbf{r}] d^3\mathbf{r}. \quad (3.29)$$

In this equation \mathbf{r}_o spans ${}_v\Omega_{-\mathbf{r}}^*$ though. See that the Common Volume Function will be zero for vectors \mathbf{r} of length longer than the longest line segment fully contained in the particle volume, so the integral will be finite even if the integration limits are infinite.

Let's now demonstrate the invariance of eq. 3.29 against rotations of the direct and reciprocal space bases. Let's say basis D changes to D' through matrix α , and D^* changes to D'^* , correspondingly through α^{-T} [17]. The new function I'_{hkl} , giving the reciprocal space intensity distribution in D'^* , can be found from the function I_{hkl} specified in eq. 3.29 as $I'_{hkl}([\mathbf{s}]_{D'^*}) = I_{hkl}(\alpha^T[\mathbf{s}]_{D'^*})$. Expressing all vectors by their components in the corresponding bases D and D^* , eq. 3.29 gives

$$I_{hkl}([\mathbf{s}]_{D'^*}) = \frac{I_e F^2 N_{uc}}{v_a} \iiint_{\mathbf{r} \in S_D} \text{CV}_D([\mathbf{r}]_D) \times \langle \text{Exp} \{ 2\pi i [\mathbf{s}_{hkl}]_{D'^*}^T [\boldsymbol{\delta}(\mathbf{r}_o, \mathbf{r})]_D \} \rangle_{\mathbf{r}_o} \text{Exp} \{ 2\pi i [\mathbf{s}_r]_{D'^*}^T [\mathbf{r}]_D \} d^3\mathbf{r}, \quad (3.30)$$

where $[\boldsymbol{\delta}(\mathbf{r}_o, \mathbf{r})]_D$ is defined through the function $\mathbf{u}' = \mathbf{u}'([\mathbf{r}]_D)$ as

$$\begin{aligned} [\boldsymbol{\delta}(\mathbf{r}_o, \mathbf{r})]_D &= [\mathbf{u}'(\mathbf{r}_o + \mathbf{r})]_D - [\mathbf{u}'(\mathbf{r}_o)]_D \\ &= \mathbf{u}'([\mathbf{r}_o]_D + [\mathbf{r}]_D) - \mathbf{u}'([\mathbf{r}_o]_D). \end{aligned} \quad (3.31)$$

Since $\mathbf{s} = \mathbf{s}_{hkl} + \mathbf{s}_r$, from eq. 3.30 we have that

$$\begin{aligned}
I'_{hkl}([\mathbf{s}]_{D'^*}) &= I_{hkl}(\alpha^T[\mathbf{s}]_{D'^*}) \\
&= \frac{I_e F^2 N_{uc}}{v_a} \iiint_{\mathbf{r} \in S_D} \text{CV}_D([\mathbf{r}]_D) \langle \text{Exp} \{ 2\pi i [\mathbf{s}_{hkl}]_{D'^*}^T \alpha[\boldsymbol{\delta}(\mathbf{r}_o, \mathbf{r})]_D \} \rangle_{\mathbf{r}_o} \\
&\quad \times \text{Exp} \{ 2\pi i [\mathbf{s}_r]_{D'^*}^T \alpha[\mathbf{r}]_D \} d^3 \mathbf{r} \\
&= \frac{I_e F^2 N_{uc}}{v_a} \iiint_{\mathbf{r} \in S_D} \text{CV}_{D'}([\mathbf{r}]_{D'}) \langle \text{Exp} \{ 2\pi i [\mathbf{s}_{hkl}]_{D'^*}^T [\boldsymbol{\delta}(\mathbf{r}_o, \mathbf{r})]_{D'} \} \rangle_{\mathbf{r}_o} \\
&\quad \times \text{Exp} \{ 2\pi i [\mathbf{s}_r]_{D'^*}^T [\mathbf{r}]_{D'} \} d^3 \mathbf{r},
\end{aligned} \tag{3.32}$$

where $[\boldsymbol{\delta}(\mathbf{r}_o, \mathbf{r})]_{D'}$ is defined through the image \mathbf{v}' of function \mathbf{u}' under α :

$$\begin{aligned}
\alpha[\boldsymbol{\delta}(\mathbf{r}_o, \mathbf{r})]_D &= \alpha \mathbf{u}'([\mathbf{r}_o]_D + [\mathbf{r}]_D) - \alpha \mathbf{u}'([\mathbf{r}_o]_D) \\
&= \mathbf{v}'([\mathbf{r}_o]_{D'} + [\mathbf{r}]_{D'}) - \mathbf{v}'([\mathbf{r}_o]_{D'}) \\
&= [\mathbf{v}'(\mathbf{r}_o + \mathbf{r})]_{D'} - [\mathbf{v}'(\mathbf{r}_o)]_{D'} \\
&= [\boldsymbol{\delta}(\mathbf{r}_o, \mathbf{r})]_{D'}.
\end{aligned} \tag{3.33}$$

Note that in order to use the Common Volume Function evaluated at $[\mathbf{r}]_{D'}$ we changed it to its form in basis D' . All integrand terms in the last of eqs. 3.32 are function of the transformed vector components of \mathbf{r} and \mathbf{r}_o . Therefore, since the infinitesimal volume element also stays the same with our transformation, instead of doing the integral over S_D we can do it over $S_{D'}$. Calling \mathbf{r}' and \mathbf{s}' the vectors in the new direct and corresponding reciprocal space, we can write then

$$\begin{aligned}
I'_{hkl}(\mathbf{s}') &= \frac{I_e F^2 N_{uc}}{v_a} \iiint_{\mathbf{r}' \in S_{D'}} \text{CV}_{D'}(\mathbf{r}') \langle \text{Exp} \{ 2\pi i \mathbf{s}'_{hkl} \cdot \boldsymbol{\delta}(\mathbf{r}'_o, \mathbf{r}') \} \rangle_{\mathbf{r}'_o} \\
&\quad \times \text{Exp} \{ 2\pi i \mathbf{s}'_r \cdot \mathbf{r}' \} d^3 \mathbf{r}',
\end{aligned} \tag{3.34}$$

which has exactly the same form as equation 3.29. This allows us to use that equation for any choice of direct and reciprocal space bases, D and D^* , obtained through an arbitrary rotation from the bases where the structure

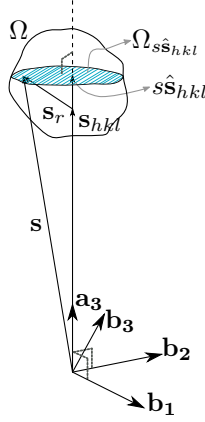


Figure 3.3: The reciprocal basis $D^* = \{\mathbf{b}_1, \mathbf{b}_2, \mathbf{b}_3\}$ convenient to find the peak profile expression with the Whole Powder Pattern Modelling approach. Vectors \mathbf{b}_1 and \mathbf{b}_2 are perpendicular to \mathbf{s}_{hkl} , which makes the direct space basis vector \mathbf{a}_3 parallel to \mathbf{s}_{hkl} . In this particular case s does not refer to the norm of \mathbf{s} , but to the distance of the plane section of Ω perpendicular to \mathbf{s}_{hkl} , $\Omega_{s\hat{\mathbf{s}}_{hkl}}$, to the origin.

factor F is specified.

For the analytical work that follows it is convenient to use a reciprocal basis $D^* = \{\mathbf{b}_1, \mathbf{b}_2, \mathbf{b}_3\}$ where vectors \mathbf{b}_1 and \mathbf{b}_2 are perpendicular to \mathbf{s}_{hkl} , as shown in Figure 3.3 [14]. Note that this makes \mathbf{a}_3 parallel to \mathbf{s}_{hkl} . This basis need not be orthorhombic, which in fact is not possible for any \mathbf{s}_{hkl} in materials of low symmetry [14]. Using such direct and reciprocal bases, the substitution of eq. 3.29 in eq. 2.47 gives (we will use the tangent

plane approximation):

$$\begin{aligned}
I_{hkl}(s) &= \frac{M}{4\pi s^2} \frac{I_e F^2 N_{uc}}{v_a} \iint_{\Omega_s^{hkl}} d^2\mathbf{s} \iint_{\mathbf{r} \in S_D} CV_D(\mathbf{r}) \langle \text{Exp}[2\pi i \mathbf{s}_{hkl} \cdot \boldsymbol{\delta}(\mathbf{r}_o, \mathbf{r})] \rangle_{\mathbf{r}_o} \\
&\quad \times \text{Exp}[2\pi i \mathbf{s}_r \cdot \mathbf{r}] d^3\mathbf{r} \\
&= \frac{M}{4\pi s^2} \frac{I_e F^2 N_{uc}}{v_a} \iint_{\mathbf{r} \in S_D} CV_D(\mathbf{r}) \langle \text{Exp}[2\pi i \mathbf{s}_{hkl} \cdot \boldsymbol{\delta}(\mathbf{r}_o, \mathbf{r})] \rangle_{\mathbf{r}_o} \\
&\quad \times \left\{ \iint_{\Omega_s^{hkl}} d^2\mathbf{s} \text{Exp}[2\pi i \mathbf{s}_r \cdot \mathbf{r}] \right\} d^3\mathbf{r}.
\end{aligned} \tag{3.35}$$

Note that the structure factor F has been considered constant and taken out of the integral over Ω_s^{hkl} in eq. 3.35. This is an approximation meaning that we are evaluating it at $\mathbf{s} = s \hat{\mathbf{s}}_{hkl}$. Using the area element

$$\begin{aligned}
d^2\mathbf{s} &= \|ds_{r_1} \mathbf{b}_1 \times ds_{r_2} \mathbf{b}_2\| = ds_{r_1} ds_{r_2} \|\mathbf{b}_1 \times \mathbf{b}_2\| \\
&= ds_{r_1} ds_{r_2} \frac{v_b}{\mathbf{b}_3 \cdot \hat{\mathbf{s}}_{hkl}} = \frac{ds_{r_1} ds_{r_2}}{v_a (\mathbf{b}_3 \cdot \hat{\mathbf{s}}_{hkl})} \\
&= \frac{a_3 ds_{r_1} ds_{r_2}}{v_a (\mathbf{b}_3 \cdot a_3 \hat{\mathbf{s}}_{hkl})} = \frac{a_3 ds_{r_1} ds_{r_2}}{v_a (\mathbf{b}_3 \cdot \mathbf{a}_3)} \\
&= \frac{a_3}{v_a} ds_{r_1} ds_{r_2},
\end{aligned} \tag{3.36}$$

the integral in \mathbf{s} can be solved as

$$\begin{aligned}
\iint_{\Omega_s^{hkl}} d^2\mathbf{s} \text{Exp}[2\pi i \mathbf{s}_r \cdot \mathbf{r}] &= \frac{a_3}{v_a} \int_{-w}^w \int_{-w}^w \text{Exp}[2\pi i s_{r_1} x] \text{Exp}[2\pi i s_{r_2} y] \\
&\quad \times \text{Exp}[2\pi i s_{r_3} z] ds_{r_1} ds_{r_2} \\
&= \frac{a_3}{v_a} \frac{\sin 2\pi\omega x}{\pi x} \frac{\sin 2\pi\omega y}{\pi y} \text{Exp}[2\pi i s_{r_3} z],
\end{aligned} \tag{3.37}$$

where the symmetric interval $[-\omega, \omega]$ is big enough to cover all the area Ω_s^{hkl} . The $\sin 2\pi\omega x / \pi x$ functions in eq. 3.37 are normalized in $(-\infty, \infty)$.

Besides, they will decrease rapidly for values of x and y far from zero, while the rest of the \mathbf{r} -dependent terms in eq. 3.35 vary smoothly. Therefore, upon substitution of eq. 3.37 in eq. 3.35 we can substitute them by Diracs' delta $\delta(x - 0)$ and $\delta(y - 0)$. Using a direct space volume element

$$\begin{aligned} d^3\mathbf{r} &= \mathbf{a}_1 dx \cdot \mathbf{a}_2 dy \times \mathbf{a}_3 dz \\ &= (\mathbf{a}_1 \cdot \mathbf{a}_2 \times \mathbf{a}_3) dx dy dz \\ &= v_a dx dy dz, \end{aligned} \tag{3.38}$$

we thus obtain from 3.35

$$\begin{aligned} I_{hkl}(s) &= \frac{Ma_3}{4\pi s^2} \frac{I_e F^2 N_{uc}}{v_a} \int_{-\infty}^{\infty} \text{Exp}[2\pi i s_{r_3} z] dz \times \\ &\quad \int_{-\infty}^{\infty} \int_{-\infty}^{\infty} \text{CV}_D(\mathbf{r}) \langle \text{Exp}[2\pi i \mathbf{s}_{hkl} \cdot \boldsymbol{\delta}(\mathbf{r}_o, \mathbf{r})] \rangle_{\mathbf{r}_o} \delta(x - 0) \delta(y - 0) dx dy \\ &= \frac{Ma_3}{4\pi s^2} \frac{I_e F^2 N_{uc}}{v_a} \int_{-\infty}^{\infty} \text{Exp}[2\pi i s_{r_3} z] \text{CV}_D(z\mathbf{a}_3) \\ &\quad \times \langle \text{Exp}[2\pi i \mathbf{s}_{hkl} \cdot \boldsymbol{\delta}(\mathbf{r}_o, z\mathbf{a}_3)] \rangle_{\mathbf{r}_o} dz. \end{aligned} \tag{3.39}$$

Since in the basis we are using \mathbf{a}_3 is parallel to \mathbf{s}_{hkl} , the exponent in the average term of eq. 3.39 can now be substituted by a PLV. Defining

$$L = za_3 \tag{3.40}$$

we have

$$\begin{aligned} \mathbf{s}_{hkl} \cdot \boldsymbol{\delta}(\mathbf{r}_o, z\mathbf{a}_3) &= s_{hkl} \hat{\mathbf{s}}_{hkl} \cdot [\mathbf{v}'(\mathbf{r}_o + z\mathbf{a}_3) - \mathbf{v}'(\mathbf{r}_o)] \\ &= s_{hkl} \Delta L(\mathbf{r}_o, \hat{\mathbf{s}}_{hkl}, za_3) \\ &= s_{hkl} \Delta L(\mathbf{r}_o, \hat{\mathbf{s}}_{hkl}, L). \end{aligned} \tag{3.41}$$

Also, from Figure 3.3 we can see that

$$s - s_{hkl} = s_{r_3} \mathbf{b}_3 \cdot \hat{\mathbf{s}}_{hkl} = \frac{s_{r_3} \mathbf{b}_3 \cdot a_3 \hat{\mathbf{s}}_{hkl}}{a_3} = \frac{s_{r_3} \mathbf{b}_3 \cdot \mathbf{a}_3}{a_3} = \frac{s_{r_3}}{a_3}. \quad (3.42)$$

Substituting eqs. 3.40, 3.41 and 3.42 in eq. 3.39 we obtain

$$I_{hkl}(s) = \frac{M}{4\pi s^2} \frac{I_e F^2 N_{uc}}{v_a} \int_{-\infty}^{\infty} \text{CV}_D(L \hat{\mathbf{s}}_{hkl}) \langle \text{Exp}[2\pi i s_{hkl} \Delta L(\mathbf{r}_o, \hat{\mathbf{s}}_{hkl}, L)] \rangle_{\mathbf{r}_o} \\ \times \text{Exp}[2\pi i (s - s_{hkl})L] dL. \quad (3.43)$$

Omitting the projection direction $\hat{\mathbf{s}}_{hkl}$ for clarity and adopting the conventions for the mean PLVs in eqs. 3.4 and 3.5, this expression can be written shortly as

$$I_{hkl}(s) = \frac{M}{4\pi s^2} \frac{I_e F^2 N_{uc}}{v_a} \int_{-\infty}^{\infty} \text{CV}(L) \langle \text{Exp}[2\pi i s_{hkl} \Delta L(L)] \rangle_{\Omega'} \\ \times \text{Exp}[2\pi i (s - s_{hkl})L] dL, \quad (3.44)$$

where Ω' is the surface delimiting the mean configuration (see Figure 3.2).

Equation 3.44 gives the profile in reciprocal space $s = 2 \sin \theta / \lambda$ of one of the hkl components of a Bragg peak profile. The total profile is then given by eq. 2.45. It is implicitly assumed that there are M identical crystallites in the sample, each with N_{uc} unit cells. Note that if particles are not spherical the Common Volume Function will be different for each profile component. When they have spherical shape on the other hand, the Common Volume Function will be the same and the total profile will be given by eq. 3.44 multiplied by the multiplicity factor of the reflection, $p(hkl)$. Equation 3.44 shows that the hkl profile will have center (but not necessarily maximum, see below) at $s_{hkl} = 2 \sin \theta_{hkl} / \lambda$. We can redefine the variable s as the previous $s - s_{hkl}$ and express a profile in reciprocal

space centered at $s = 0$, $i_{hkl}(s)$, as

$$i_{hkl}(s) = K(s_{hkl} + s) \int_{-\infty}^{\infty} A_{hkl}^S(L) A_{hkl}^D(L) \text{Exp}[2\pi i sL] dL, \quad (3.45)$$

where,

$$\begin{aligned} K(s_{hkl} + s) &= \frac{M}{4\pi(s_{hkl} + s)^2} \frac{I_e F^2 N_{uc}}{v_a} \\ A_{hkl}^S(L) &= CV(L) \\ A_{hkl}^D(L) &= \langle \text{Exp}[2\pi i s_{hkl} \Delta L(L)] \rangle_{\Omega'}. \end{aligned} \quad (3.46)$$

Note that the term $I_e F^2$ is meant to be evaluated at $s_{hkl} + s$ too. Equation 3.45 is the *fundamental expression* with regard to the Whole Powder Pattern Modelling (WPPM) approach [1] (see also [3], p. 268, and [13], p. 41), when dealing with a mono-disperse powder samples in which the lattice distortion can be described by some smooth displacement field. It is also a general equation in powder diffraction, and shows how the zero-centered profile in reciprocal space can be found as the Fourier Transform (FT) of a function embodying the particle's *size effect*, $A_{hkl}^S(L)$, and *distortion effect*, $A_{hkl}^D(L)$. As such, neglecting the factor K , the peak $i_{hkl}(s)$ will be normalized (unitary area), since $A_{hkl}^S(0)A_{hkl}^D(0) = 1$. Expanding the distortion term as

$$\begin{aligned} A_{hkl}^D(L) &= \langle \cos(2\pi s_{hkl} \Delta L(L)) \rangle_{\Omega'} + i \langle \sin(2\pi s_{hkl} \Delta L(L)) \rangle_{\Omega'} \\ &= M_{hkl}^D(L) + i N_{hkl}^D(L), \end{aligned} \quad (3.47)$$

eq. 3.45 expands as

$$\begin{aligned}
i_{hkl}(s) = K(s_{hkl} + s) & \left\{ \int_{-\infty}^{\infty} A_{hkl}^S(L) M_{hkl}^D(L) \cos(2\pi sL) dL \right. \\
& + i \int_{-\infty}^{\infty} A_{hkl}^S(L) M_{hkl}^D(L) \sin(2\pi sL) dL \\
& + i \int_{-\infty}^{\infty} A_{hkl}^S(L) N_{hkl}^D(L) \cos(2\pi sL) dL \\
& \left. - \int_{-\infty}^{\infty} A_{hkl}^S(L) N_{hkl}^D(L) \sin(2\pi sL) dL \right\}.
\end{aligned} \tag{3.48}$$

Since for a fixed pair of points inside the particle the PLV is an odd function of L , as seen in section 3.1, from eq. 3.47 the real part of the distortion FT term, $M_{hkl}^D(L)$, will be an even function of L , whereas the imaginary part $N_{hkl}^D(L)$ will be an odd function. The size term $A_{hkl}^S(L)$ is an even function of L . This means that the integrals in eq. 3.48 having the imaginary unit i as factor will be null, since their integrands will be odd functions. The other two integrands will be even functions. Therefore, we can rewrite equation 3.48 as

$$i_{hkl}(s) = i_{hkl}^R(s) + i_{hkl}^I(s), \tag{3.49}$$

where

$$\begin{aligned}
i_{hkl}^R(s) &= 2K(s_{hkl} + s) \int_0^{\infty} A_{hkl}^S(L) M_{hkl}^D(L) \cos(2\pi sL) dL \\
i_{hkl}^I(s) &= -2K(s_{hkl} + s) \int_0^{\infty} A_{hkl}^S(L) N_{hkl}^D(L) \sin(2\pi sL) dL.
\end{aligned} \tag{3.50}$$

$i_{hkl}^R(s)$ and $i_{hkl}^I(s)$ are called, respectively, the *real* and *imaginary profile components* of $i_{hkl}(s)$. In practice, for a monodisperse sample, the integration will always be done up to a limit $L_{max} = L_{max}(h, k, l)$, since beyond

that the size term $A_{hkl}^S(L)$ will be null. The real profile will always be an even function of s with maximum at 0, whereas the imaginary component will be odd. Thus, when the imaginary profile is not zero, the resulting profile will have maximum shifted from zero and will be neither an even nor an odd function. This will naturally result in an *asymmetric* peak profile in reciprocal space carrying the size and strain effects ⁴.

When lattice distortion or strains are small ($2\pi s_{hkl}\Delta L(L)$ small for any L) the real and imaginary distortion FT components can be Taylor expanded as

$$\begin{aligned}
 M_{hkl}^D(L) &= \langle \cos(2\pi s_{hkl}\Delta L(L)) \rangle_{\Omega'} \approx 1 - 2\pi^2 s_{hkl}^2 \langle \Delta L^2(L) \rangle_{\Omega'} \\
 &\approx \text{Exp}[-2\pi^2 s_{hkl}^2 \langle \Delta L^2(L) \rangle_{\Omega'}] \\
 N_{hkl}^D(L) &= \langle \sin(2\pi s_{hkl}\Delta L(L)) \rangle_{\Omega'} \approx 2\pi s_{hkl} \langle \Delta L(L) \rangle_{\Omega'}.
 \end{aligned}
 \tag{3.51}$$

With this approximation, all what we need to know in order to build a peak profile with the WPPM approach, are the mean and mean square PLVs in Ω' .

⁴Note that a symmetric peak profile in reciprocal space will always be asymmetric in 2θ or direct space, because of the non linearity of the transformation $s = 2 \sin \theta / \lambda$.

Chapter 4

Diffraction peak profiles of surface relaxed spherical nanocrystals

• ◦ • ◦ *This chapter has been adapted from [18].*

The surface structure of crystals is characterized by an atomic environment different from the bulk, influencing chemical bonds on the surface and several atomic layers underneath. A modified atomic rearrangement is responsible for static and dynamic disorder, if not for the formation of specific surface structures, different from the corresponding bulk structure. This phenomenon is well known in surface sciences, where it has been extensively studied under the general terms of surface relaxation and surface reconstruction [19, 20].

The effect most frequently reported for nanoparticle systems is a change in bond distances, related to a surface atomic coordination lower than in the bulk. When observed by X-ray Powder Diffraction (XRPD) the main effect is a displacement of Bragg peaks, most often described in terms of change in average unit cell parameter [21, 22]. This is just part of the effect, since the lattice distortion created by the surface is not homogeneous, being larger on the surface region and decaying toward the inside, and thus yields a peak broadening in addition to peak displacement.

The effects on peak profiles of the Surface Relaxation (SR) phenomenon, as it will be referred to hereafter, has been considered by several authors. The concept of “apparent lattice parameter” was introduced in [23] to link

its plots against the diffraction vector modulus with specific distortion states of a particle due to the surface. Rather basic and simplified models were proposed by Nunes & Lin [24] and by Ishikawa & Uemori [25] as well, so to provide closed expressions for the powder diffraction peak profiles; the lattice distortion effect of SR was represented as an exponential displacement of parallel atomic planes near the particle surface. Displacement of single atoms has been recently considered [26, 27, 28], although none of the cited papers present analytical expressions for the peak profiles. The first attempt to model XRPD peak profiles in reciprocal space according to a WPPM approach was reported in [29], but these authors too used a simplified model based on planar displacements, taking no account of the anisotropy of the elastic medium.

In the present chapter we propose a consistent model for the SR effect on XRPD peak profiles which can be used directly within a WPPM approach presented in Chapter 3. Since there is no general rule on how an arbitrary nanoparticle distorts because of the SR effect, we deliberately opted for a simple but flexible model able to account, at least approximately, for a large variety of cases, mostly considering metals or simple inorganic systems. Closed analytical expressions are obtained and peak profiles are computed by the Fourier Transform approach of WPPM. The expressions will depend only on three parameters, each one with a clear physical meaning, characterizing the SR as one more type of crystalline defect, according to the perturbative approach of WPPM. In order to obtain a proof of concept we confine attention to nanoparticles of cubic symmetry and monodisperse spherical shape, but the approach, however, can be extended to lower symmetries and different shapes.

4.1 Lattice distortion of nanoparticles due to Surface Relaxation

Surface relaxation may cause quite different, even opposite effects, like contraction or expansion of nanoparticles [22, 30], depending on the specific material considered. Even if these effects have been studied in nanocryst-

talline powders as well as in thin films, here we confine attention to the former case only. Early experiments on fcc metal nanoparticles point out a contraction when the size decreases. This was observed in Au [22], Ag [31], Pt [32] and Al [33], but in Cu, with clean as well as oxidized surface, no appreciable variation of lattice parameter was found [32, 34]. More recent studies reveal a small decrease in the cell parameter of Cu with crystallite size in the range 20-200 nm [35]. On the contrary Ni tends to expand [36, 37, 38]. Average contraction with decreasing size was also found in bcc metals, like Fe [39] and W [40], and in non-cubic metals like Sn and Bi below 35 nm of particle size [41]; the latter case was explained as a vacancy effect, although this interpretation is not shared by all authors [42, 43, 44].

While most metal nanoparticles tend to shrink with decreasing size, the opposite is true for several ceramics. TiO_2 anatase expands when particle size decreases from 33 to 4 nm [45]; similar observations are reported for cubic CeO_2 obtained by different preparations [29, 46, 47], while a significant expansion was observed for BaTiO_3 [48], and other perovskites (e.g., SrTiO_3 [49] and PbTiO_3 [50], which shows expansion dependent on decreasing particle size in the paraelectric cubic polymorph). Surface effect was studied in MgO powders [51]: while samples prepared in vacuum showed lattice contraction for decreasing particle size, those prepared in air expanded. Surface stress and adsorbed water were considered to explain this behavior [52]. Also iron (III) oxide expands in both its main (γ and α) phases: explanations provided in [53] point out an expansion driven by surface effects. Finally, two non-cubic binary oxides, ZnO [54, 55, 56] and SnO_2 [57, 58], also show lattice expansion in small-sized particles, with different trends for the variation of the unit cell parameters in the tetragonal structure.

Literature on the size-dependent structure of materials is abundant, more examples (also including non-oxide materials) could be found in [59, 60, 61, 40]. The examples mentioned above on several metals and oxides are, nevertheless, enough to illustrate the variability of SR effects, including contingent conditions, like whether nanoparticles are free, or

embedded in a matrix or held on some support (e.g., see the complex cases of silver [31, 62, 34, 63] and anatase [64, 45]). It is therefore difficult to predict whether single-crystal nanoparticles expand or contract when size decreases, as well as the extent of the effect. The model we propose in this chapter describes SR in general terms, without relying on specific details which are expected to be different from one type of material or experiment to another; single atom displacements are mainly driven by the sub-coordination, so the model better applies to metals, but it can also be used empirically for ceramics.

A further element of importance is nanoparticle shape. It is once again difficult to make a general model, valid for any shape, so we consider a spherical shape, which at the same time is (i) sufficiently simple to yield analytical expressions of the SR effect including also elastic anisotropy, but also (ii) a reasonable approximation to many real cases. But we would like to point out that monodisperse, single-crystal and spherical shape nanoparticles can be really produced. Most often nanoparticles have well defined polygonal shape, possibly distorted and with rounded corners [65, 66, 67, 68, 69, 70, 71, 72], but silver [73, 74] and gold [75] nanospheres have been produced, with sizes below 40 nm and around 80 nm, and in the size range 15-30 nm, respectively. Recently, gold spherical single-crystals have also been obtained below 10 nm with a narrow size distribution using a seed-mediated method [76]. Further examples of metal nanospheres are found for the FePt alloy [77, 78, 79], where spherical shape and monodispersity during annealing treatments can be preserved by high melting-point ceramic coatings (SiO_2 or MgO) or by grinding with a large excess of NaCl [80, 81, 82, 83]. Highly monodisperse single-crystal nanoparticles of fct FePt phase are obtained, usually in the 3-10 nm range and with rounded sphere-like shape, after the salt coating is removed [83, 84]. Single-crystal spherical nanoparticles have also been obtained for perovskites structures and simple oxides, like barium titanate [85], TiO_2 brookite [86] and Mn_3O_4 [87].

4.2 A displacement field due to the Surface Relaxation phenomenon

As concluded in Chapter 3, all what we need to know in order to build a peak profile with the WPPM approach, are the mean and mean square of the Projected Length Variation, as defined in section 3.1. In turn, these two magnitudes depend on the particular displacement field $\mathbf{u}(\mathbf{r})$ describing the distortion of the particle. Taking the Surface Relaxation as the only defect creating the distortion of the crystal structure, we now propose a model for the displacement caused by it in an arbitrary point inside the crystallite.

The displacements of atoms near the surface can be quite complex as it was commented before. There is no a general rule that tell us how much a given atom in a terrace or kink will displace and in which direction [88]. Nevertheless some evidences from experiments and simulations already exist, and they agree in that the amount of this displacement will be proportional to how much sub-coordinated the atom is, i.e. to how much the coordination of the atom decreased respect to one fully coordinated. So this will be one contribution to the displacement of the atoms due to the presence of the surface. We will call it the *coordination contribution*.

Simulations by Molecular Dynamics have further shown that the distortion due to the surface is not only confined to regions near it, but actually extends into the core of nanoparticles [89]. In the present work we will model this second contribution considering the nanoparticle as an elastically anisotropic body that deforms according to the laws of linear elasticity [90]. We will call this one the *elastic contribution*.

To keep things simple while still being near to some real experimental cases as mentioned before, we will develop a model for single crystal nanoparticles with spherical shape and monodisperse size distribution (all identical spherical particles). Secondly, we will consider that the atomic displacements are always in radial sense. Molecular Dynamics simulations on metal nanoparticles have shown that while for morphologies far from spheres, like cubes, this assumption is clearly false, for spherical shape it

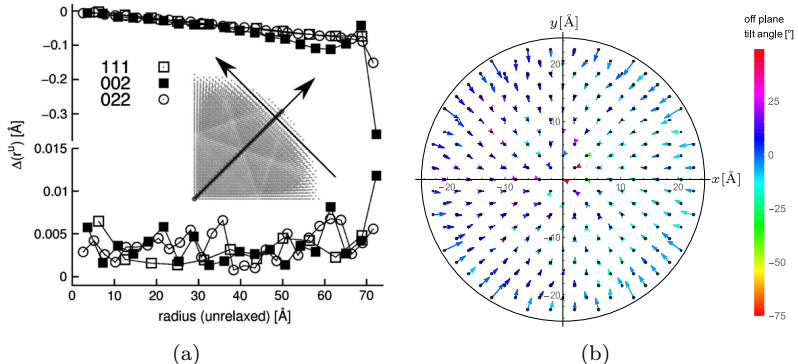


Figure 4.1: Atomic displacements due to the Surface Relaxation phenomenon. (a) Mean projected displacement along -upper part- and perpendicular -lower part- to some hkl directions, as function of the radial position. Plot for a free standing Cu spherical particle [89]. (b) Atomic displacements projected in the 100 plane for a Ag spherical particle of 5 nm diameter. The predominant blue color of the arrows demonstrate the radial sense of the displacements. The positive off-plane tilt angle is toward the reader (figure built with unpublished data from [28]).

is a good approximation (see Figure 4.1).

The idea of considering the displacement field due to the presence of the surface in terms of “coordination” and “elastic” contributions is not new, as it was already proposed in [28]. In what follows nevertheless, we will consider each contribution separately, providing specific physical justifications in each case. Besides, these contributions will not determine directly the final position of the atoms due to the lattice relaxation, but their displacements from a perfect lattice position. This choice agrees better with the nature of the contributions we are considering for the atomic displacement, as it will be shown later. Last, for the case of the elastic contribution we propose a more physically meaningful expression than what was proposed in [28].

4.3 The coordination contribution

Suppose that an atom in some structure (molecule or crystal) is bonded to other n of the same nature. Reviewing the available data about solid materials with metallic and covalent bonds, in 1947 Pauling observed that the bond radius (half of the inter-atomic distance) of that atom and that of one bonded with only one, can be related with the equation [91]:

$$R(n) - R(1) = -0.353 \log_{10} n \text{ \AA}. \quad (4.1)$$

Writing down this expression for the possible maximum coordination N in a crystalline structure and subtracting both of these equations we get

$$R(n) - R(N) = 0.353 \log_{10} \frac{N}{n} \text{ \AA}. \quad (4.2)$$

If we consider now one sub-coordinated atom in the surface bonded to other n , most of them fully coordinated (i.e. other atoms “not in the surface”), the right member of this equation would give approximately the displacement of that atom in surface. This is because we can think about atoms fully coordinated as less free to move, compared to those sub-coordinated. The right member of eq. 4.2 says that the displacement of an atom due to the sub-coordination effect is proportional to the logarithm of the ratio between the maximum coordination it can have, N , and its real coordination in the crystalline structure, n . The value of n will be between a maximum N for fully coordinated atoms in the bulk, and a minimum for some surface atoms. In between values of n can be reasonably assigned to atoms placed in a spherical layer of thickness r_o , near the surface of the reference spherical nanoparticle of radius R (see Figure 4.2a). We will call it the *sub-coordination layer*. Inside this layer, n will decrease when we approach the surface. Making an average over all possible directions we can consider n as a continuous function $n(r)$, going from a maximum of N , for $r = R - r_o$, to a minimum of M , for $r = R$, equal to the average coordination of surface atoms. Correspondingly, the logarithm factor in equation 4.2 will go from zero to a maximum of $\log_{10} N/M$ in the same

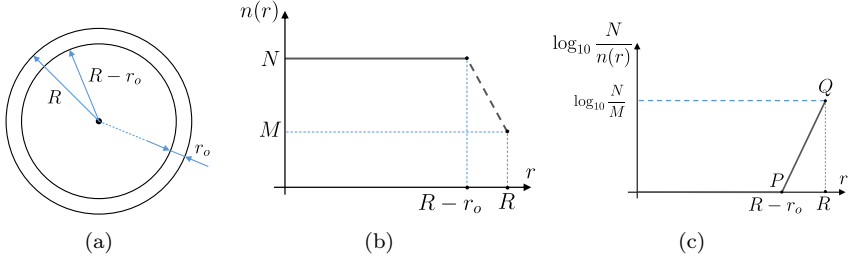


Figure 4.2: Sub-coordination component of the displacement field. (a) Cross section of the sphere representing a particle with a sub-coordination layer of thickness r_o near the surface. (b) Average behavior of the coordination n as function of the radial position r . (c) Average behavior of $\log_{10} N/n$ considering the coordination n as a continuous function $n(r)$. The equation of the line segment between the points P and Q is $\log_{10}(N/M) (r/r_o - (R - r_o)/r_o)$. See text for more details.

region, giving displacements for all atoms in there and not only for those on the particle surface (sphere surface). This is illustrated in Figure 4.2b and 4.2c. Based on the fact that in general $r_o \ll R$, we will consider the behavior of this logarithm term simply linear in the sub-coordination layer, as shown in Figure 4.2c. In this way we obtain a radial displacement component due to the sub-coordination effect, $u^c(\mathbf{r})$, which will affect only atoms in a thin layer of thickness r_o near the surface:

$$u^c(\mathbf{r}) = \begin{cases} 0.353 \log_{10} \frac{N}{M} \left(\frac{1}{r_o} r - \frac{R - r_o}{r_o} \right) \hat{\mathbf{r}}, & \text{for } R - r_o \leq r \leq R \\ 0, & \text{for } 0 \leq r < R - r_o. \end{cases} \quad (4.3)$$

In this equation it can be seen that the factor $0.353 \log_{10}(N/M)$ will give the average maximum radial displacement possible, which will correspond to atoms in the surface with $r = R$. In order to gain some flexibility in the model we will now let this maximum displacement to be a free signed parameter β . The same will be done for the sub-coordination layer thickness $r_o > 0$. They will be parameters to be found from the modelling of the experimental diffraction pattern, in the framework of the WPPM approach. Note that the sign of β will determine whether the lattice near

the surface expands ($\beta > 0$) or contracts ($\beta < 0$), taking into account the behavior of different materials as pointed out before. In this way we propose for the sub-coordination component of the displacement field due to the Surface Relaxation phenomenon:

$$\mathbf{u}^c(\mathbf{r}) = \beta f_{R,r_o}(r) \hat{\mathbf{r}}, \quad (4.4)$$

where

$$f_{R,r_o}(r) = \begin{cases} \frac{1}{r_o}r - \frac{R-r_o}{r_o}, & \text{for } R - r_o \leq r \leq R \\ 0, & \text{for } 0 \leq r < R - r_o. \end{cases} \quad (4.5)$$

Although we have made a deduction of this expression following a particular initial idea (that of Pauling [91]) it can be considered as a simplified and general way to describe the lattice distortion near the surface of a nanocrystal. What this equation says is that, due to the truncation of the crystalline structure and thus the sub-coordination of some atoms, there will be a distortion of the lattice which will take its maximum expression in the surface and will extend some distance toward the core. Even if here we have proposed a specific behavior of this distortion, namely a radial displacement of a magnitude that varies linearly, the approach qualitatively agrees with previous ones. For instance, in [23] a core and a surface region with finite thickness were considered as well. The distortion of the lattice was described nevertheless by means of a constant lattice parameter in the core and a radially varying one in the surface region, instead of a continuous displacement field as in this work. Experimentally, it was observed in [92] that lattice distortion in TiO_2 nanoparticles were mainly located in the surface. From a theoretically point of view and taking as example this same semiconductor, in [30] the concepts of surface-, near surface- and bulk-regions, were proposed to differentiate among lattice regions with different degree of distortion due to the surface. There the surface region was defined as that where atoms have a modified coordination geometry, which can be understood as modified distance and bond angles with first neighbors. This effect clearly extends some distance into the core of the particle and is not only confined to atoms exactly on the surface (those

who lose some bonds when the surface is created). Here we have taken this into account through the proposed atomic coordination variation with the distance, $n(r)$. Although the coordination number as a concept does not vary continuously as we proposed, the underlying idea, which is surface lattice distortion that gradually extend some distance into the particle's core, is the same.

4.4 The elastic contribution

Several authors have explained the lattice expansion or contraction of small nanoparticles by means of a size-induced equivalent hydrostatic pressure over the particle surface [93, 94, 53, 44, 61]. If we suppose the spherical nanoparticle as an elastically anisotropic body subject to hydrostatic pressure (Figure 4.3c), equations from the elastostatics theory allow for finding the resulting distortion of the body, $\mathbf{u}(\mathbf{r})$, provided we fully specify its compliance tensor s_{ijkl} . To estimate only the radial component of this displacement field we can, nevertheless, follow a simple approach. Suppose we are interested in the radial component of the displacement of a point placed at \mathbf{r} respect to a Cartesian basis $C = \{\hat{\mathbf{x}}_1, \hat{\mathbf{x}}_2, \hat{\mathbf{x}}_3\}$, parallel to the usual basis of the cubic material. As an approximation, we can assume this displacement equal to what it would be if the point were placed on an infinitesimally thin bar parallel to $\hat{\mathbf{r}}$, subject to a longitudinal pressure σ (see Figures 4.3d and 4.4). Let's define the auxiliary Cartesian basis $C' = \{\hat{\mathbf{x}}'_1, \hat{\mathbf{x}}'_2, \hat{\mathbf{x}}'_3\}$ with $\hat{\mathbf{x}}'_1$ parallel to $\hat{\mathbf{r}}$. Since the bar is homogeneous, we can assume that the stress tensor σ_{ij} , resulting inside it due to the applied longitudinal pressure, is homogeneous, i.e. independent of the position. This means that the strain tensor ϵ_{ij} is also homogeneous, since $\epsilon_{ij} = s_{ijkl} \sigma_{kl}$ and all components in the compliance tensor s_{ijkl} are constants [90]. Since the (1,1) component of the strain tensor in the system C' , ϵ'_{11} , is related to the displacement field in that system $\mathbf{u}'(u'_1, u'_2, u'_3)$ by $\epsilon'_{11} = \partial u'_1 / \partial x'_1$, we conclude that the component of displacement along

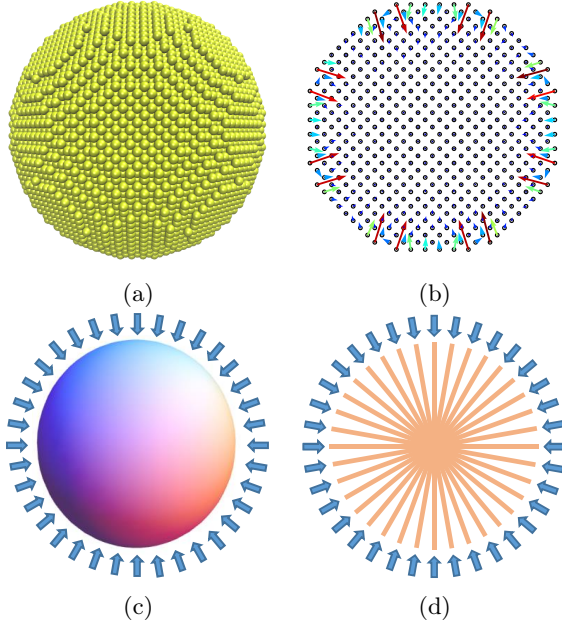


Figure 4.3: Model for the response of a spherical nanoparticle subject to an external hydrostatic pressure. (a) Atomistic model of a spherical nanoparticle. (b) Typical displacement field obtained from a Molecular Dynamics simulation. (c) Elastic anisotropic spherical body subject to hydrostatic pressure. (d) Set of intercepting radial bars carved from the spherical body, each one subject to the same longitudinal pressure σ .

the bar, $u'_1(x'_1)$, is simply proportional to the position x'_1 :

$$u'_1(x'_1) = \frac{\partial u'_1}{\partial x'_1} x'_1 = \epsilon'_{11} x'_1. \quad (4.6)$$

The dependence of u'_1 on x'_2 and x'_3 can be neglected since the bar is infinitesimally thin. The ratio between the applied longitudinal pressure $\sigma = \sigma'_{11}$ and ϵ'_{11} is the Young modulus, E , along the direction of the bar. Since $E = 1/s'_{11}$, where s'_{11} is the (1,1) component of the compliance

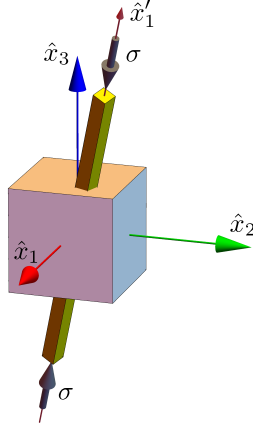


Figure 4.4: Carved bar parallel to the $\hat{\mathbf{x}}'$ direction, subject to a longitudinal pressure σ .

matrix expressed in the C' system, eq. 4.6 gives

$$u'_1(x'_1) = s'_{11} \sigma'_{11} x'_1, \quad (4.7)$$

where

$$s'_{11} = s_{11} - 2(s_{11} - s_{12} - \frac{1}{2}s_{44})(l_1^2 l_2^2 + l_2^2 l_3^2 + l_3^2 l_1^2) \quad (4.8)$$

is the inverse of the Young modulus along the direction of the bar $[\hat{\mathbf{x}}'_1]_C = [l_1, l_2, l_3]^T$, supposing that the material has cubic symmetry [90]. Now we can generalize eq. 4.7 to an arbitrary orientation of the bar $[\hat{\mathbf{r}}]_C = [l_1, l_2, l_3]^T$, obtaining an expression for the radial component of displacement at a point \mathbf{r} inside the spherical nanoparticle:

$$\mathbf{u}^e(\mathbf{r}) = \sigma s'_r r \hat{\mathbf{r}}. \quad (4.9)$$

This will be the radial displacement component due to the size-induced hydrostatic pressure and the elastic response of the material. Shortly, the elastic contribution to the displacement. Note that the sign of σ will be negative for the case of compression (particle contraction) and positive for

the case of tension (particle expansion). $s'_{\hat{\mathbf{r}}}$ is the inverse of the Young modulus along $\hat{\mathbf{r}}$, given by eq. 4.8 provided we are using a Cartesian basis parallel to the cubic basis of the material. In this way we end up with the following expression for the displacement field due to the Surface Relaxation phenomenon:

$$\mathbf{u}(\mathbf{r}) = \mathbf{u}^e(\mathbf{r}) + \mathbf{u}^c(\mathbf{r}) = \sigma s'_{\hat{\mathbf{r}}} \mathbf{r} + \beta f_{R,r_o}(r) \hat{\mathbf{r}}. \quad (4.10)$$

The three parameters of the SR model for describing peak profiles are now visible in this equation. We summarize their definitions: σ , the size-induced pressure; β , the maximum radial displacement due to the sub-coordinated effect; $r_o > 0$, the thickness of the layer where atoms are displaced mainly because of the sub-coordination effect (sub-coordination layer thickness). Note that β and σ may have opposite signs, meaning that the particle surface and core show opposite contraction/expansion behavior.

A quick examination of eq. 4.10 shows that it will give a radial strain in the core of the nanoparticle independent of the radial position \mathbf{r} , $\|\mathbf{u}\|/r = \sigma s'_{\hat{\mathbf{r}}}$. This is in agreement with Molecular Dynamics simulations of metal nanoparticles [27, 89]. Nevertheless, the oscillatory behavior of the radial strain also shown in these studies will not be reproduced by the simple model we are proposing.

4.5 The Fourier Transform components for the peak profile due to the Surface Relaxation phenomenon

Once we have defined the displacement field $\mathbf{u}(\mathbf{r})$ we can try to find the corresponding analytical expressions for the distortion terms $M_{hkl}^D(L)$ and $N_{hkl}^D(L)$ of eqs. 3.51. As shown in those equations, we can do this in terms of the mean and mean square of the Projected Length Variation, $\langle \Delta L(L) \rangle$ and $\langle \Delta L^2(L) \rangle$. To find these two quantities we will follow again Warren [95, 3]. Namely, for a given component of a Bragg reflection we will

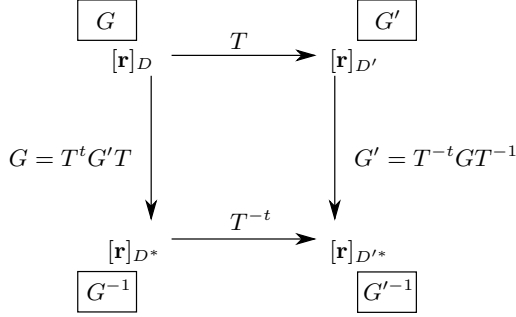


Figure 4.5: Diagram for the orthorhombic basis D' . The arrows indicate transformations of the component of a vector \mathbf{r} from one basis to another. For instance $T[\mathbf{r}]_D = [\mathbf{r}]_{D'}$. The matrices inside squares are the metric tensors of the corresponding bases. See [17] for details.

find an orthorhombic basis with the z -axis parallel to the hkl direction, such that this reflection takes the form $00l'$. This is always possible for cubic symmetry materials [96]. We will then express the deformation field in a Cartesian basis parallel to that basis, and will compute there the mentioned mean values.

Let's denote the basis of the cubic material $D = \{\mathbf{a}, \mathbf{b}, \mathbf{c}\}$ and its reciprocal basis by $D^* = \{\mathbf{a}^*, \mathbf{b}^*, \mathbf{c}^*\}$. In D^* the reciprocal lattice vector \mathbf{s}_{hkl} , corresponding to the hkl component of the Bragg reflection, will have components $[\mathbf{s}]_D = [h, k, l]^T$. Similarly, let's denote the orthorhombic basis by $D' = \{\mathbf{a}', \mathbf{b}', \mathbf{c}'\}$, and its reciprocal basis by $D'^* = \{\mathbf{a}'^*, \mathbf{b}'^*, \mathbf{c}'^*\}$. Let's denote the metric tensors of D and D' by G and G' , respectively, and the change of basis matrix from D to D' by T . The relations between these bases and matrices are shown schematically in Figure 4.5. The conditions mentioned before for the orthorhombic basis D' can be transformed to three conditions for matrix T . First, T^{-1} can be written with integer components, since D' is a basis for the same crystalline structure as D ¹.

¹By definition the columns of T^{-1} are the components of the basis vectors of D' in the basis D , i.e. $T^{-1} = [[\mathbf{a}']_D | [\mathbf{b}']_D | [\mathbf{c}']_D]$. For a cubic $D = \{\mathbf{a}, \mathbf{b}, \mathbf{c}\}$, any set of orthogonal vectors \mathbf{a}' , \mathbf{b}' and \mathbf{c}' belonging to the lattice spanned by D , will define a basis D' for the same crystalline structure, and will have integer components in D .

Secondly, T must be such that G' is a diagonal matrix, since D' must be an orthorhombic basis ². Third, T must be such that in the reciprocal basis of D' , \mathbf{s} has components $[\mathbf{s}]_{D'^*} = [0, 0, l']^T$, with integer l' . Let's define the auxiliary matrix with integer entries $A = T^{-t}$. As shown in Figure 4.5, $G' = T^{-t} G T^{-1}$. Since D is a cubic basis, $G = a^2 I$, where a is the lattice parameter and I is the identity matrix. Therefore $G' = a^2 A A^T$. Writing down all the matrices in this equation and according to the second condition for T just mentioned we have:

$$\begin{bmatrix} a'^2 & 0 & 0 \\ 0 & b'^2 & 0 \\ 0 & 0 & c'^2 \end{bmatrix} = a^2 \begin{bmatrix} a_{11} & a_{12} & a_{13} \\ a_{21} & a_{22} & a_{23} \\ a_{31} & a_{32} & a_{33} \end{bmatrix} \begin{bmatrix} a_{11} & a_{21} & a_{31} \\ a_{12} & a_{22} & a_{32} \\ a_{13} & a_{23} & a_{33} \end{bmatrix} \quad (4.11)$$

which gives three equations that the entries of A must hold:

$$\begin{aligned} a_{11}a_{21} + a_{12}a_{22} + a_{13}a_{23} &= 0 \\ a_{11}a_{31} + a_{12}a_{32} + a_{13}a_{33} &= 0 \\ a_{21}a_{31} + a_{22}a_{32} + a_{23}a_{33} &= 0. \end{aligned} \quad (4.12)$$

Other three equations can be obtained from the condition $A[\mathbf{s}]_{D^*} = [\mathbf{s}]_{D'^*}$ (see Figure 4.5). Writing down the matrices and according to the third condition for T we have

$$\begin{bmatrix} a_{11} & a_{12} & a_{13} \\ a_{21} & a_{22} & a_{23} \\ a_{31} & a_{32} & a_{33} \end{bmatrix} \begin{bmatrix} h \\ k \\ l \end{bmatrix} = \begin{bmatrix} 0 \\ 0 \\ l' \end{bmatrix}, \quad (4.13)$$

which gives

$$\begin{aligned} a_{11}h + a_{12}k + a_{13}l &= 0 \\ a_{21}h + a_{22}k + a_{23}l &= 0 \\ a_{31}h + a_{32}k + a_{33}l &= l'. \end{aligned} \quad (4.14)$$

Now, according to the first condition, we have to find a solution for eqs.

²If G is the metric tensor of $D' = \{\mathbf{v}_1, \mathbf{v}_2, \mathbf{v}_3\}$, then its entries are $\{G'_{ij}\} = \mathbf{v}_i \cdot \mathbf{v}_j$. If D' is an orthorhombic (orthogonal) basis then $\mathbf{v}_i \cdot \mathbf{v}_j = 0$ for $i \neq j$.

4.12 and 4.14 with only integer numbers a_{ij} . This can easily be done if we give a geometrical interpretation to the problem. We can imagine the numbers a_{11} , a_{12} and a_{13} as the components of a vector \mathbf{a}_1 in a Cartesian basis, and similarly for the rest of the a_{ij} . Then, looking to eqs. 4.12 and 4.14 we conclude that vectors \mathbf{a}_1 , \mathbf{a}_2 and \mathbf{a}_3 are mutually perpendicular and that \mathbf{a}_3 is parallel to a vector with components $[h, k, l]^T$. Let's choose $a_{31} = h$, $a_{32} = k$ and $a_{33} = l$, i.e. $l' = h^2 + k^2 + l^2$. A vector perpendicular to \mathbf{a}_3 , which can be chosen as \mathbf{a}_1 , is $\mathbf{a}_3 \times \hat{\mathbf{k}}$, where $\hat{\mathbf{k}}$ is the versor along the z -axis of the Cartesian basis. We thus obtain $a_{11} = k$, $a_{12} = -h$ and $a_{13} = 0$. To obtain \mathbf{a}_2 we just make the cross product $\mathbf{a}_3 \times \mathbf{a}_1$, which gives $a_{21} = hl$, $a_{22} = kl$ and $a_{23} = -h^2 - k^2$. In this way we obtain for the matrix A :

$$A = \begin{bmatrix} k & -h & 0 \\ hl & kl & -h^2 - k^2 \\ h & k & l \end{bmatrix}. \quad (4.15)$$

It can be easily verified that the entries of this matrix satisfy eqs. 4.12 and 4.14. To express the deformation field in a Cartesian basis C' parallel to D' , we need the change of basis matrix, α , from C to C' , where C is the Cartesian basis parallel to D . Calling the basis vectors of D and D' as \mathbf{a}_i and \mathbf{a}'_i , the entry (i, j) of α will be given by the cosine of the angle between \mathbf{a}_i and \mathbf{a}'_j :

$$\alpha_{ij} = \cos(\mathbf{a}_j, \mathbf{a}'_i) = \frac{[\mathbf{a}_j]_D^T G [\mathbf{a}'_i]_D}{\|\mathbf{a}_j\| \|\mathbf{a}'_i\|} = \frac{[\mathbf{a}_j]_D^T [\mathbf{a}'_i]_D}{([\mathbf{a}'_i]_D^T [\mathbf{a}'_i]_D)^{1/2}}, \quad (4.16)$$

where we have used the fact that $\|\mathbf{a}_j\| = a$, the lattice parameter of D , and $G = a^2 I$. Given an arbitrary matrix m , let's label its i th row as $m^{(i)}$ and its j th column as $m_{(j)}$. With this notation eq. 4.16 can be worked

out as

$$\begin{aligned}
\alpha_{ij} &= \frac{[\delta_{j1}, \delta_{j2}, \delta_{j3}](T^{-1})_{(i)}}{((T^{-1})_{(i)}(T^{-1})_{(i)})^{1/2}} \\
&= \frac{[\delta_{j1}, \delta_{j2}, \delta_{j3}]A^{(i)}}{(A^{(i)}A^{(i)})^{1/2}} = \frac{\sum_{k=1}^3 \delta_{jk}a_{ik}}{\left(\sum_{k=1}^3 a_{ik}^2\right)^{1/2}} \\
&= \frac{a_{ij}}{\left(\sum_{k=1}^3 a_{ik}^2\right)^{1/2}},
\end{aligned} \tag{4.17}$$

where δ_{ij} is the Kronecker delta. Substituting the entries of matrix A from eq. 4.15 we then obtain for matrix α

$$\alpha = \begin{bmatrix} \frac{k}{\sqrt{h^2+k^2}} & -\frac{h}{\sqrt{h^2+k^2}} & 0 \\ \frac{hl}{\sqrt{(h^2+k^2)(h^2+k^2+l^2)}} & \frac{kl}{\sqrt{(h^2+k^2)(h^2+k^2+l^2)}} & \frac{-h^2-k^2}{\sqrt{(h^2+k^2)(h^2+k^2+l^2)}} \\ \frac{h}{\sqrt{h^2+k^2+l^2}} & \frac{k}{\sqrt{h^2+k^2+l^2}} & \frac{l}{\sqrt{h^2+k^2+l^2}} \end{bmatrix}. \tag{4.18}$$

Note that α is orthogonal ($\alpha^{-1} = \alpha^T$), as expected for a transformation (rotation) matrix between two Cartesian bases. From eq. 4.10 we see that only the term corresponding to the elastic contribution of the deformation field will be affected by the change of basis $C \rightarrow C'$, since the sub-coordination term only depends on the absolute value of \mathbf{r} , which remains the same. What we should do now, therefore, is to find the corresponding expression for the inverse of the Young modulus in a given direction, when the used basis is C' . With the form of α shown above, the compliance tensor s_{ijkl} will transform, in general, in such a way that the corresponding compliance matrix s_{ij} in basis C' will not have the usual form for cubic materials. We mean the form referred to the Cartesian basis parallel to the common basis of the cubic material, a case where there are only three distinct entries s_{11} , s_{12} and s_{44} in the compliance matrix [90]. Consequently the inverse of the Young modulus in a given direction will not be given simply by eq. 4.8 but, in principle, by a different expression for each hkl we study. Nevertheless we can save this difficulty and keep using eq. 4.8

if we apply before α^{-1} , i.e. if we use the components of the normalized position vector \mathbf{r} in the “old basis”. The i th of such components will be given by

$$l_i = \frac{[\mathbf{r}]_C^{(i)}}{r} = \frac{(\alpha^{-1}[\mathbf{r}]_{C'})^{(i)}}{r} = \frac{[\alpha_{(i)}]^T [\mathbf{r}]_{C'}}{r}. \quad (4.19)$$

Defining the function $g_{hkl}([\mathbf{r}]_{C'})$ as

$$\begin{aligned} g_{hkl}([\mathbf{r}]_{C'}) &= l_1^2 l_2^2 + l_2^2 l_3^2 + l_3^2 l_1^2 = \sum_{i=1}^2 \sum_{j=i+1}^3 l_i^2 l_j^2 \\ &= r^{-4} \sum_{i=1}^2 \sum_{j=i+1}^3 ([\alpha_{(i)}]^T [\mathbf{r}]_{C'})^2 ([\alpha_{(j)}]^T [\mathbf{r}]_{C'})^2, \end{aligned} \quad (4.20)$$

we then can express the displacement field in the basis C' as

$$\mathbf{u}(\mathbf{r}) = \sigma s_{\hat{\mathbf{r}}}'' \mathbf{r} + \beta f_{R,r_o}(r) \hat{\mathbf{r}}, \quad (4.21)$$

where

$$s_{\hat{\mathbf{r}}}'' = s_{11} - 2(s_{11} - s_{12} - s_{44}/2) g_{hkl}([\mathbf{r}]_{C'}). \quad (4.22)$$

All the analytical work that follows will be done with the position vector \mathbf{r} referred to the basis C' . Therefore let's now call this basis simply C , with orthonormal axes $\{\hat{\mathbf{i}}, \hat{\mathbf{j}}, \hat{\mathbf{k}}\}$. The components of \mathbf{r} in C will be denoted as usual $[\mathbf{r}]_C = [x, y, z]^T$, and the vectorial displacement field with its components along each axis as $\mathbf{u}(\mathbf{r}) = \mathbf{u}(u_x(\mathbf{r}), u_y(\mathbf{r}), u_z(\mathbf{r}))$.

Since in C the z -axis is parallel to the hkl direction, the Projected Length Variation between two points separated a distance $|L|$ will be given by

$$\Delta L(L) = u_z(\mathbf{r} + L\hat{\mathbf{z}}) - u_z(\mathbf{r}). \quad (4.23)$$

From eq. 4.21 the z -component of the displacement field is

$$u_z(\mathbf{r}) = \sigma s_{\hat{\mathbf{r}}}'' z + \beta \frac{f_{R,r_o}(r)}{r} z. \quad (4.24)$$

This expression is considerably complicated by the complex form of the function g_{hkl} , which enters through the term $s_{\hat{\mathbf{r}}}''$. The number of terms

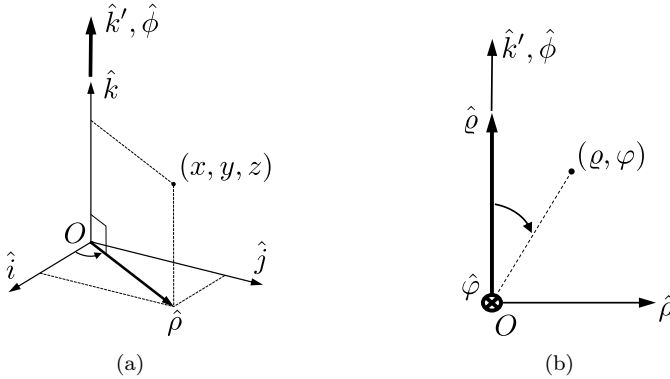


Figure 4.6: Change of basis used to express the z -component of the displacement field. (a) Relation between the Cartesian coordinate system (x, y, z) of basis C and the cylindrical coordinate system (ρ, ϕ, z') . (b) Relation between (ρ, ϕ, z') and the polar coordinate system $\{\rho, \varphi\}$. The versor $\hat{\phi}$ in (b) is pointing from the reader toward the paper.

will be further increased when we square it in order to find $\langle \Delta L^2(L) \rangle$. Therefore, it is convenient to make some approximations to simplify it. Adopting a cylindrical coordinate system (ρ, ϕ, z') related to the basis C system (x, y, z) as:

$$\begin{aligned}
 x &= \rho \cos \phi \\
 y &= \rho \sin \phi \\
 z' &= z,
 \end{aligned}
 \tag{4.25}$$

the only term depending on ϕ in eq. 4.24 will be $s_{\mathbf{r}}''$, since $r = (\rho^2 + z^2)^{1/2}$. See Figure 4.6a. We can eliminate this dependence approximating $s_{\mathbf{r}}''$ by its mean over ϕ , while keeping ρ and z' constant (mean over a circular path δl of length l , centered about and perpendicular to the z -axis, and at

height z):

$$\begin{aligned}
 s_{\mathbf{r}}'' &\approx \frac{1}{l} \oint_{\delta l} s_{\mathbf{r}}'' dl = \frac{1}{2\pi\rho} \left\{ 2\pi\rho s_{11} - 2(s_{11} - s_{12} - s_{44}/2)\rho \int_0^{2\pi} g_{hkl}([\mathbf{r}]_C) d\phi \right\} \\
 &= s_{11} - \frac{s_{11} - s_{12} - s_{44}/2}{\pi} \int_0^{2\pi} g_{hkl}([\mathbf{r}]_C) d\phi.
 \end{aligned} \tag{4.26}$$

Using eq. 4.20 the integral of g_{hkl} can be solved to give

$$\int_0^{2\pi} g_{hkl}([\mathbf{r}]_C) d\phi = \frac{\gamma_1 z^4 + \gamma_2 z^2 \rho^2 + \gamma_3 \rho^4}{(\rho^2 + z^2)^2}, \tag{4.27}$$

where

$$\begin{aligned}
 \gamma_1 &= 2\pi H \\
 \gamma_2 &= 2\pi(H' - H) \\
 \gamma_3 &= 2\pi \left(\frac{1}{8}H' + \frac{5}{8}H \right),
 \end{aligned} \tag{4.28}$$

and

$$\begin{aligned}
 H &= \frac{h^2 k^2 + k^2 l^2 + l^2 h^2}{(h^2 + k^2 + l^2)^2} \\
 H' &= \frac{h^4 + k^4 + l^4}{(h^2 + k^2 + l^2)^2}.
 \end{aligned} \tag{4.29}$$

Eqs. 4.26-4.29 allow us to rewrite eq. 4.24 as

$$\begin{aligned}
 u_z(\rho, z) &= \sigma z \left[s_{11} - \frac{s_{11} - s_{12} - s_{44}/2}{\pi(\rho^2 + z^2)^2} (\gamma_1 z^4 + \gamma_2 z^2 \rho^2 + \gamma_3 \rho^4) \right] \\
 &\quad + \beta z \frac{f_{R,r_o}((\rho^2 + z^2)^{1/2})}{(\rho^2 + z^2)^{1/2}}.
 \end{aligned} \tag{4.30}$$

The cylindrical symmetry of eq. 4.30 allows for its further simplification. Let's define another coordinate system, a polar one (ϱ, φ) , related to the last cylindrical system through

$$\begin{aligned}
 \rho &= \varrho \sin \varphi \\
 z &= \varrho \cos \varphi,
 \end{aligned} \tag{4.31}$$

and oriented respect to that as shown in Figure 4.6b. In this new system the polar axis is oriented as the z -axis, and the polar angle is measured positive in clockwise sense from the latter. Making these substitutions in eq. 4.30 we obtain

$$u_z(\varrho, \varphi) = \sigma \varrho (a \cos \varphi + b \cos^3 \varphi + c \cos^5 \varphi) + \beta \cos \varphi f_{R,r_o}(\varrho), \quad (4.32)$$

with

$$\begin{aligned} a &= s_{11} - \gamma_3(s_{11} - s_{12} - s_{44}/2)/\pi, \\ b &= (2\gamma_3 - \gamma_2)(s_{11} - s_{12} - s_{44}/2)/\pi, \\ c &= (\gamma_2 - \gamma_1 - \gamma_3)(s_{11} - s_{12} - s_{44}/2)/\pi. \end{aligned} \quad (4.33)$$

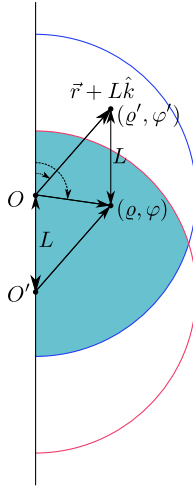


Figure 4.7: Geometrical construction for the calculation of $\langle \Delta L(L) \rangle$ and $\langle \Delta L^2(L) \rangle$ in the $\{\hat{\varrho}, \hat{\varphi}\}$ system. The solid of revolution generated by the rotation of the shadowed area around the polar axis, is the region where the mean values $\langle \Delta L(L) \rangle$ and $\langle \Delta L^2(L) \rangle$ will be computed, for a given distance L . The blue semi-circle represents a half cross section of the spherical nanoparticle of radius R .

The evaluation of ΔL (eq. 4.23) can now be easily done with the expression of u_z in eq. 4.32 and the last polar coordinates system. Let's

denote the coordinates of a point at \mathbf{r} , respect to the common origin O we have been using, as $[\mathbf{r}]_O = (\varrho, \varphi)$. See Figure 4.6b. The point at $\mathbf{r} + L\hat{\mathbf{k}}$ will have coordinates $[\mathbf{r} + L\hat{\mathbf{k}}]_O = (\varrho', \varphi')$. From Figure 4.7 it can be seen that $[\mathbf{r} + L\hat{\mathbf{k}}]_O = [\mathbf{r}]_{O'}$, where O' is an origin placed at (L, π) respect to O . Figure 4.7 allows also for visualizing the region where ΔL is defined and where its mean and square mean will be computed, for a given value of L . It corresponds to the solid of revolution around the polar axis generated by the intersection area of the two equal semi-circles centered at O and O' , respectively. In this way we obtain for ΔL :

$$\begin{aligned}\Delta L &= u_z(\varrho', \varphi') - u_z(\varrho, \varphi) \\ &= a\sigma(\varrho' \cos \varphi' - \varrho \cos \varphi) + b\sigma(\varrho' \cos^3 \varphi' - \varrho \cos^3 \varphi) \\ &\quad + c\sigma(\varrho' \cos^5 \varphi' - \varrho \cos^5 \varphi) + \beta(f_{R,r_o}(\varrho') \cos \varphi' - f_{R,r_o}(\varrho) \cos \varphi)\end{aligned}\tag{4.34}$$

and for ΔL^2 :

$$\begin{aligned}\Delta L^2 &= (u_z(\varrho', \varphi') - u_z(\varrho, \varphi))^2 \\ &= a^2\sigma^2(\varrho \cos \varphi - \varrho' \cos \varphi')^2 \\ &\quad + 2ab\sigma^2(\varrho \cos \varphi - \varrho' \cos \varphi')(\varrho \cos^3 \varphi - \varrho' \cos^3 \varphi') \\ &\quad + b^2\sigma^2(\varrho \cos^3 \varphi - \varrho' \cos^3 \varphi')^2 \\ &\quad + 2ac\sigma^2(\varrho \cos \varphi - \varrho' \cos \varphi')(\varrho \cos^5 \varphi - \varrho' \cos^5 \varphi') \\ &\quad + 2bc\sigma^2(\varrho \cos^3 \varphi - \varrho' \cos^3 \varphi')(\varrho \cos^5 \varphi - \varrho' \cos^5 \varphi') \\ &\quad + c^2\sigma^2(\varrho \cos^5 \varphi - \varrho' \cos^5 \varphi')^2 \\ &\quad + 2a\beta\sigma(\varrho \cos \varphi - \varrho' \cos \varphi')(f_{R,r_o}(\varrho) \cos \varphi - f_{R,r_o}(\varrho') \cos \varphi') \\ &\quad + 2b\beta\sigma(\varrho \cos^3 \varphi - \varrho' \cos^3 \varphi')(f_{R,r_o}(\varrho) \cos \varphi - f_{R,r_o}(\varrho') \cos \varphi') \\ &\quad + 2c\beta\sigma(\varrho \cos^5 \varphi - \varrho' \cos^5 \varphi')(f_{R,r_o}(\varrho) \cos \varphi - f_{R,r_o}(\varrho') \cos \varphi') \\ &\quad + \beta^2(f_{R,r_o}(\varrho) \cos \varphi - f_{R,r_o}(\varrho') \cos \varphi')^2.\end{aligned}\tag{4.35}$$

The computation of $\langle \Delta L(L) \rangle$ and $\langle \Delta L^2(L) \rangle$ now corresponds to the computation of the mean values over the mentioned solid of revolution of the terms enclosed in parenthesis in eqs. 4.34 and 4.35. Using the definitions

in Table 4.1 we finally obtain for $\langle \Delta L(L) \rangle$ and $\langle \Delta L^2(L) \rangle$ the expressions:

$$\langle \Delta L(L) \rangle = a\sigma G_1(R, L) + b\sigma G_2(R, L) + c\sigma G_3(R, L) + \beta G_4(R, L, r_o) \quad (4.36)$$

$$\begin{aligned} \langle \Delta L^2(L) \rangle &= a^2\sigma^2 F_1(R, L) + ab\sigma^2 F_2(R, L) + b^2\sigma^2 F_3(R, L) + ac\sigma^2 F_4(R, L) \\ &+ bc\sigma^2 F_5(R, L) + c^2\sigma^2 F_6(R, L) + a\beta\sigma F_7(R, L, r_o) \\ &+ b\beta\sigma F_8(R, L, r_o) + c\beta\sigma F_9(R, L, r_o) + \beta^2 F_{10}(R, L, r_o). \end{aligned} \quad (4.37)$$

Functions F_i and G_i are listed in Appendix A for brevity. The mean and mean square PLVs in eqs. 4.36 and 4.37 are referred to the as-built configuration and not to the mean one (see Figure 3.2). Therefore, before using them in eqs. 3.51 to build the peak profiles with the WPPM approach, the corrections in eqs. 3.17 and 3.18 of section 3.2 must be applied.

Table 4.1: Definition of the functions whose mean values are needed to compute $\langle \Delta L(L) \rangle$ and $\langle \Delta L^2(L) \rangle$. $CV(R, L) = (4\pi R^3/3)(L^3/16R^3 - 3L/4R + 1)$ is the common volume between two spheres of radius R separated by distance L , and δV denotes that region. $\langle f(\mathbf{r}) \rangle = [CV(R, L)]^{-1} \times \iiint_{\delta V} f(\mathbf{r}) d^3\mathbf{r}$. See text for more details.

$f(\mathbf{r})$	$\langle f(\mathbf{r}) \rangle$
$\varrho' \cos \varphi' - \varrho \cos \varphi$	$G_1(R, L)$
$\varrho' \cos^3 \varphi' - \varrho \cos^3 \varphi$	$G_2(R, L)$
$\varrho' \cos^5 \varphi' - \varrho \cos^5 \varphi$	$G_3(R, L)$
$f_{R,r_o}(\varrho') \cos \varphi' - f_{R,r_o}(\varrho) \cos \varphi$	$G_4(R, L, r_o)$
$(\varrho \cos \varphi - \varrho' \cos \varphi')^2$	$F_1(R, L)$
$2(\varrho \cos \varphi - \varrho' \cos \varphi') (\varrho \cos^3 \varphi - \varrho' \cos^3 \varphi')$	$F_2(R, L)$
$(\varrho \cos^3 \varphi - \varrho' \cos^3 \varphi')^2$	$F_3(R, L)$
$2(\varrho \cos \varphi - \varrho' \cos \varphi') (\varrho \cos^5 \varphi - \varrho' \cos^5 \varphi')$	$F_4(R, L)$
$2(\varrho \cos^3 \varphi - \varrho' \cos^3 \varphi') (\varrho \cos^5 \varphi - \varrho' \cos^5 \varphi')$	$F_5(R, L)$
$(\varrho \cos^5 \varphi - \varrho' \cos^5 \varphi')^2$	$F_6(R, L)$
$2(\varrho \cos \varphi - \varrho' \cos \varphi') (f_{R,r_o}(\varrho) \cos \varphi - f_{R,r_o}(\varrho') \cos \varphi')$	$F_7(R, L, r_o)$
$2(\varrho \cos^3 \varphi - \varrho' \cos^3 \varphi') (f_{R,r_o}(\varrho) \cos \varphi - f_{R,r_o}(\varrho') \cos \varphi')$	$F_8(R, L, r_o)$
$2(\varrho \cos^5 \varphi - \varrho' \cos^5 \varphi') (f_{R,r_o}(\varrho) \cos \varphi - f_{R,r_o}(\varrho') \cos \varphi')$	$F_9(R, L, r_o)$
$(f_{R,r_o}(\varrho) \cos \varphi - f_{R,r_o}(\varrho') \cos \varphi')^2$	$F_{10}(R, L, r_o)$

4.6 Surface Relaxation macro for *TOPAS*

• ◦ • ◦ *This section has been adapted from [97].*

The surface relaxation model described above have been implemented in a *TOPAS* [98, 99] macro called WPPM_SR_Sphere [97]. The macro is shown in Figure 4.8, as well as an example call in Figure 4.9, for the case of a Pt nanoparticle. Differently from others WPPM *TOPAS* macros, in this case the later it is set to do the FT up to the particle diameter as maximum Fourier length: $\text{WPPM_L_max} = 2 * \text{CeV}(\text{radioc}, \text{radiov})$. No stopping criteria is based on the values of the real or imaginary FT (the command `WPPM_brake_on_small` is not used). This is because for the Surface Relaxation phenomenon the real and imaginary strain FT components may be non-monotonous [97].

4.7 Molecular Dynamics simulations setup

In the present thesis Molecular Dynamics simulation were performed to obtain vibrational trajectories of atoms in a particle, and from them the corresponding relaxed configuration (see Figure 3.2). The objective was to obtain a realistic version of the atomic building at room temperature (298 K), i.e. a relaxed configuration, as termed in Figure 3.2 [28, 100]. Simulations were performed in vacuum, and although periodic boundary conditions were enforced, the simulation box was chosen with linear dimension three times larger than the particle radius. In this way cross interactions between different replicas of the system are impossible. The timestep (ts) for simulation was chosen as some orders of magnitude smaller than the reciprocal of the highest frequency of motion [101, 102], while the overall timescale (the duration in wall-time) was long enough to sample a suitable number of statistically uncorrelated configurations of the system. For Pd, for instance, the maximum frequencies are on the order of $\text{THz} = 10^{12} \text{s}^{-1}$ [103, 104], therefore the integration ts is chosen to be 1 femto-second = 10^{-15} s and the time for the simulation at least 0.75 ns. The potentials used were EAM potentials [105], listed in [106]. All simulations were performed using the Large-scale Atomic/Molecular Massively

```

macro WPPM_SR_Sphere(sigmac, sigmav, betac, betav, roc, rov, radioc,
radiov, shiftc, shiftv, s11, s12, s44) {
  #m_argu sigmac 'in TPa if s11, s12, s44 are in TPa^-1
  #m_argu betac 'in nm
  #m_argu roc 'in nm
  #m_argu radioc 'in nm
  #m_argu shiftc 'pure number
  WPPM_ft_conv = {
    def sigma = CeV(sigmac,sigmav);
    def beta = CeV(betac,betav);
    def ro = CeV(roc, rov);
    def RR = CeV(radioc, radiov);
    def shift = CeV(shiftc, shiftv);
    def qhkl = 2*Pi/(D_spacing*0.1); 'interplanar distance in nm
    def deltaL = meanDeltaL(RR, WPPM_L/(shift+1),H,K,L,s11,s12,s44,
sigma,beta,ro);
    def deltaLsquare = meanDeltaL2(RR, WPPM_L/(shift+1),H,K,L,s11,s12,
s44,sigma,beta,ro);
    def deltaLsquareCorr = deltaLsquareCorrFun(deltaL, deltaLsquare,
shift,WPPM_L/(shift+1));
    return Exp((-1/2)*qhkl^2*deltaLsquareCorr);
  }
  WPPM_ft_conv_im = {
    def sigma = CeV(sigmac,sigmav);
    def beta = CeV(betac,betav);
    def ro = CeV(roc, rov);
    def RR = CeV(radioc, radiov);
    def shift = CeV(shiftc, shiftv);
    def qhkl = 2*Pi/(D_spacing*0.1); 'interplanar distance in nm
    def deltaL = meanDeltaL(RR, WPPM_L/(shift+1),H,K,L,s11,s12,s44,
sigma, beta, ro);
    def deltaLCorr = deltaLCorrFun(deltaL, shift, WPPM_L/(shift+1));
    return qhkl*deltaLCorr;
  }
  WPPM_L_max = 2*CeV(radioc, radiov);
  WPPM_th2_range = 55;
}

```

Figure 4.8: *TOPAS* macro `WPPM_SR_Sphere`. For the exact definition of the functions `meanDeltaL`, `meanDeltaL2`, `meanDeltaLsquareCorrFun`, and so forth, see the file “`WPPM_SR_Sphere_macro.inc`” in the Supplementary information of [97].

Parallel Simulator (LAMMPS) [107].

The simulations start at 0 K from the as-built configuration, letting the system arrive to a static equilibrium configuration in a maximum of 1000

```

prm !s11 = 7.33706; 'elastic costants for Pt in TPa^-1 units
prm !s12 = -3.0796;
prm !s44 = 12.987;
prm RRR 4.67813' min .001 max=Min(2 Val+.01,20); val_on_continue=Rand(0,4);
prm nofAtoms 28727.79819'
fit_obj = saxs(X, 10*RRR /*A*/, 1.54059/*A*/, nofAtoms, 78);
prm !aPtbulk = 3.9242;
STR(F_M_3_M)
phase_name "platinum"
Cubic(!aPt 3.9115_0.000041)
  site Pt x 0 y 0 z 0 occ Pt 1 beq 0
MVW( 780.312, 59.845, 100.000')
prm !ssigma -0.000392 ' TPa
prm !bbeta -0.0214 ' nm
prm !rro 0.133 ' nm
prm kk = Constant(aPt)/aPtbulk -1;
WPPM_Sphere(, RRR)
WPPM_SR_Sphere(,ssigma,,bbeta,,rro,,RRR,,kk,s11,s12,s44)

```

Figure 4.9: Macro call example for macro WPPM_SR_Sphere. The saxs function models the small angle scattering from a sphere; see the Supplementary information of [97] for its definition.

ts. Then a chain of Nose-Hoove thermostats in NVT regime is used, to slowly bring the system to room temperature conditions. The total number of ts used at this stage is 250 000, evenly divided among each thermostat. Equilibration before system sampling is achieved letting it further evolve in NVE regime, during 500 000 ts, once room temperature is reached at the end of the chain. System sampling every 1000 ts is made during additional 250 000 ts, after which the simulation ends. With this sampling a vibrational trajectory at room temperature is obtained, composed of 250 particle snapshots. The relaxed configuration is obtained averaging the configurations in the vibrational trajectory. Powder diffraction patterns carrying only the effect of the static disorder, can then be computed feeding the Debye scattering equation with the relaxed configuration [28, 100]. Thermal Diffuse Scattering patterns, on the other hand, can be obtained from the vibration trajectory, as described in Chapter 5.

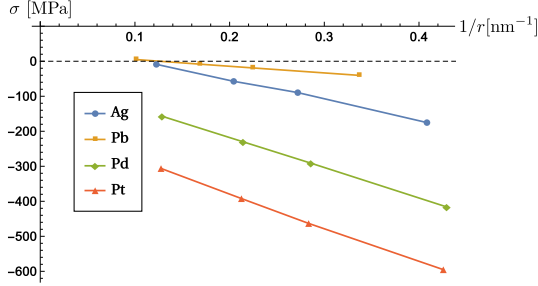


Figure 4.10: Inverse proportionality between effective pressure and nanoparticle radius (from Table 4.2, see text for details).

4.8 Test of the Surface Relaxation model

To test the model described so far we used nanocrystals at room temperature, obtained through Molecular Dynamics (MD) simulations as described in section 4.7. To start with we displace atom positions of an ideal, perfect spherical nanocrystal, according to eq. 4.10, to match the MD relaxed configuration. To this purpose we minimize the sum of squares of distances between atomic positions, i.e. parameters σ , β and r_o were varied to minimize the function h :

$$h(\sigma, \beta, r_o) = \sum_{i=1}^N [\mathbf{r}_{i,r} - (\mathbf{r}_{i,u} + \mathbf{u}(\mathbf{r}_{i,u}))]^2, \quad (4.38)$$

with N as the number of atoms, and $\mathbf{r}_{i,r}$ and $\mathbf{r}_{i,u}$, as positions of the i th atom, respectively in the MD relaxed configuration and according to eq. 4.10. This procedure was applied to spherical nanocrystals of Ag, Pb, Pd and Pt, with radius of 6, 9, 12 and 20 unit cells. Results are listed in Table 4.2.

As expected, the increase of σ is inversely proportional to the nanoparticle radius (Figure 4.10), with larger values for stiffer metals, i.e. growing in the sequence Pb→Ag→Pd→Pt. Differences in β and r_o values for different metals are small, pointing out similarity in the SR effect. Pb is most peculiar in this group of metals, with a thicker sub-coordination layer of

Table 4.2: Values of parameters in eq. 4.10 after minimization of eq. 4.38 for nanoparticles of different metals and sizes. The Young Modulus is shown for each metal.

metal	radius [nm]	σ [GPa]	β [\AA]	r_o [\AA]
Ag (83 GPa)	2.45	-1.75e-1	-2.11e-1	1.56
	3.68	-8.94e-2	-2.06e-1	1.48
	4.90	-5.72e-2	-2.02e-1	1.52
	8.17	-8.70e-3	-1.98e-1	1.46
Pb (16 GPa)	2.97	-4.03e-2	-4.19e-1	2.13
	4.46	-1.90e-2	-4.34e-1	1.92
	5.94	-8.28e-3	-4.36e-1	1.93
	9.90	4.90e-3	-4.22e-1	1.86
Pd (121 GPa)	2.33	-4.16e-1	-2.01e-1	1.39
	3.50	-2.91e-1	-1.92e-1	1.35
	4.67	-2.30e-1	-1.84e-1	1.38
	7.78	-1.57e-1	-1.84e-1	1.33
Pt (168 GPa)	2.35	-5.95e-1	-2.22e-1	1.43
	3.53	-4.63e-1	-2.19e-1	1.32
	4.71	-3.92e-1	-2.14e-1	1.33
	7.85	-3.06e-1	-2.12e-1	1.27

about 0.2 nm, likely due to the much smaller Young modulus compared to the other three metals. In addition, it effectively shows a particle core transition from contraction to expansion when increasing size, while in the surface contraction is still predominant (see also Figure 4.12a). Nanoparticle surface contraction (β) agrees with experimental values of surface atom displacement in several fcc metals, including Au [26], Pt [108] and Pd [109].

Comparison between MD simulations and nanocrystal deformed according to the model can also be made for the corresponding XRPD patterns, obtained by feeding the atomic coordinates to the Debye scattering equation. Figure 4.11a shows the XRPD pattern for a Pd nanocrystal of radius 6 unit cells (2.3 nm). Agreement between MD (dots) and the model (line) is quite good, as it is demonstrated by the small difference (see residual below, amplified by a factor 10X). Agreement further im-

proves for larger sizes (Figure 4.11b); the proposed model seems to work even better for Ag, as shown in Figure 4.11c. The inset shows a detail of the main effect of SR, which is peak shift, with finer details affecting the line profiles. Results for Pb (Figure 4.11d) are still acceptably good, although the match between XRPD patterns generated by MD and the model is the least satisfactory of the four metals investigated. Reason is (i) low stiffness of Pb, causing large deformation (cf. β in Table 4.2), (ii) quite high elastic anisotropy (Zener ratio $A_z = 4.1$ [110]), and (iii) low shear modulus (5.6 GPa). As a consequence, the atomic displacements from the perfect crystal lattice positions of a Pb nanosphere (Figure 4.12b) have a larger non-radial component, causing deviations from the proposed model.

A common tool in the analysis of XRPD line profiles is the Warren plot. As illustrated in section 3.1, different values of the PLV, $\Delta L(L)$, are obtained when different line segments of length $|L|$ are examined inside a particle, in general. First introduced in a seminal paper on the so-called Warren-Averbach method [95], the Warren plot is a plot of the standard deviation of $\Delta L(L)$ against L , for some specific direction, i.e. $\sigma_{\Delta L} = \sqrt{\langle \Delta L^2 \rangle - \langle \Delta L \rangle^2}$ vs L . If the mean displacement is zero we simply have $\sigma_{\Delta L} = \sqrt{\langle \Delta L^2 \rangle}$ vs L . The Warren plot for the pattern in Figure 4.11c (Ag nanosphere) is shown in Figure 4.13a, for the [111] direction. Discrete points are from MD and from the model given by eq. 4.10, whereas the line is given by the model's eqs. 4.36 and 4.37. The distribution corresponding to the data point indicated by the arrow is shown in Figure 4.13b. The good agreement in Figure 4.13a, between MD result and model confirms the validity of the proposed approach to capture information on the atomic displacement caused by SR. Contrary to what reported for work-hardened metals, $\sigma_{\Delta L}$ steadily grows with L . This is a peculiarity of the SR effect, related to the effective hydrostatic pressure and sub-coordination effects. A similar trend, although less markedly growing with L , was observed for small metal domains embedded in a polycrystalline matrix, where also some effective uniform pressure was active [111]. The study of line profiles from nanocrystals could therefore provide insights on the specificity of the

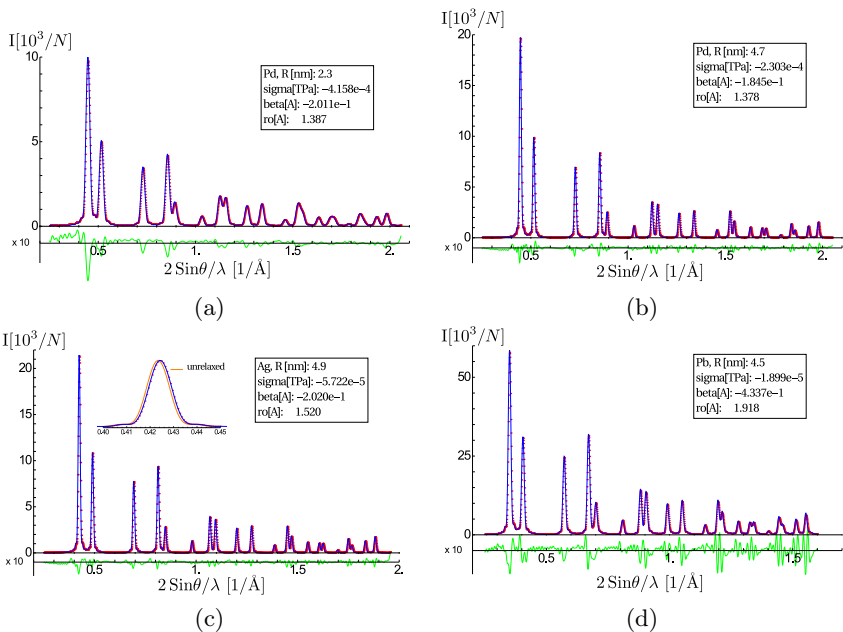


Figure 4.11: XRPD patterns for spherical nanoparticles: (a) Pd, radius 2.3 nm and (b) 4.7 nm; (c) Ag, radius 4.9 nm; (d) Pb, radius 4.5 nm. Patterns are obtained by using the Debye scattering equation with atomic coordinates provided by MD (dot) or by applying the SR model: the difference (residual) is shown below with a 10X magnification factor. Used parameter values are shown in the inset of each pattern; a further inset in (c) shows the shift between the peak position of the starting perfect spherical crystal model (unrelaxed, orange) and same crystal after application of the model. N is the number of atoms in the particle in each case.

atomic displacement, which depend on nanocrystal composition, size and shape, as well as on the environment.

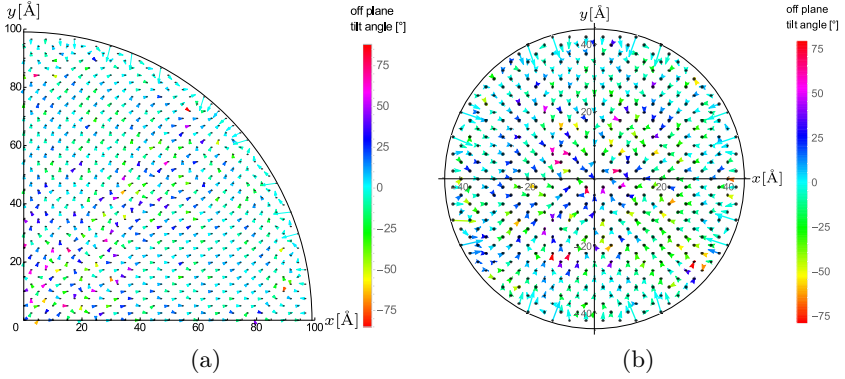


Figure 4.12: Scaled atomic displacements projected in the 100 plane for some Pb spherical particles. (a) One fourth of the cross section, radius 9.90 nm. (b) Whole cross section, radius 4.5 nm (pattern shown in Figure 4.11d). Arrow lengths are magnified by a factor 15 for easier reading of the figure, to highlight non-radial displacement components (cf. Figure 4.1b for Cu). The positive off-plane tilt angle is toward the reader. Figure built with unpublished data from [28].

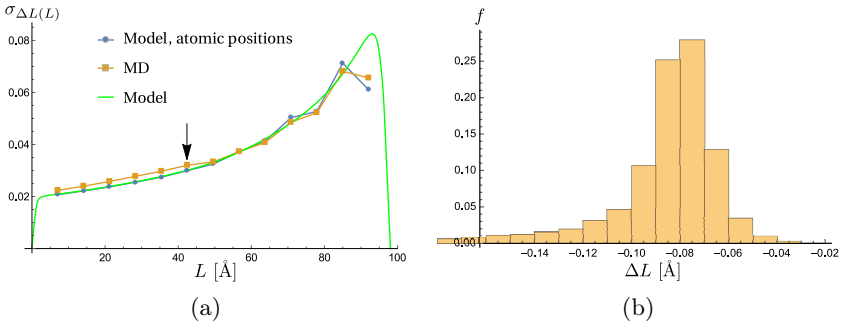


Figure 4.13: (a) Warren plots along [111] for the Ag nanoparticle of radius 4.9 nm (Figure 4.11c). Square points are obtained from the relaxed atomic configuration provided by MD, whereas circles are from the model eq. 4.10 with parameters from the minimization of eq. 4.38; the line is the corresponding continuous trend of $\sigma_{\Delta L}$ according to the model (see text for details). The arrow indicates the data point corresponding to the distribution (b) shown aside.

Chapter 5

Thermal Diffuse Scattering in nanoparticles

As shown in Chapter 2, the total scattered intensity from a particle can be split in two contributions, the Bragg and the Thermal Diffuse Scattering (TDS) intensity. When integrated with the powder average, the TDS intensity in reciprocal space gives rise to peaks underneath the Bragg peaks, forming a background profile far from a flat or polynomial one [112, 7, 3]. The later featureless TDS contributions would therefore lead to errors in the calculated integrated intensities or modeled Bragg peak profiles. Because of this, many models have been proposed to account for thermal vibrations (see [113], section 7.1.4, and references therein). Any departure from a mean (after thermal vibration) perfect crystalline structure will also cause diffuse scattering [114], masking the effect of the TDS in a one dimensional diffraction pattern. Therefore, the goal of the mentioned TDS model is to estimate as accurate as possible the contribution of the TDS intensity to the total scattered intensity at each 2θ , rather than to extract information about the phenomena underlying the TDS. All diffuse scattering intensity not due to thermal vibration is then taken into account through an additional polynomial background. This approach allows for a better profile, and thus integrated intensity determination in structural and microstructural studies of polycrystalline materials (see, for instance, [3] p. 199).

Since the 60s of last century the TDS models for powder samples have

been extended to deal also with fine particles, or nanoparticles, as it is preferred to term them nowadays (see [113], section 7.4.2, and references therein). The extensions have been based mainly on modifications to the same theory proposed for larger particles, by using more suitable Vibrational Densities of States and defining a non-zero minimum vibration mode wavelength. One of these model is the work by Beyerlein et. al. [115]. In that work the validity of the extension is assessed by comparing against patterns computed with the Debye equation, over atomic configurations obtained through Molecular Dynamics simulations. In the present chapter this model is reviewed, supplying for additional details and correcting some errors in the original work. In addition, we improve the assessing procedure used by Beyerlein et. al. by comparing against the profile of the TDS alone, instead of the total profile which, in general, is several orders of magnitude more intense (as shown in section 2.4, the Debye equation always gives the total intensity at any s). This will allow to isolate and study with greater detail the *dynamic* component of the disorder in a nanoparticle. Particularly, the anisotropy of the TDS will be shown, highlighting the limitations of Beyerlein et. al., and similar, models.

5.1 The Vibrational Density of States in nanoparticles

The vectors \mathbf{g} that give atomic vibrations with all possible frequencies, according to the Born-von Kármán theory of lattice dynamics introduced in section 2.3, are inside the first Brillouin zone. The angular frequency $\omega_{\mathbf{q}j} = 2\pi\nu_{\mathbf{q}j}$ of wave $\mathbf{q}j$ in this theory is, in general, given by a dispersion relation $\omega_{\mathbf{q}j} = \omega_{\mathbf{q}j}(\mathbf{q})$. Counting the waves with frequency between ω and $\omega + d\omega$ among all the modes, the so called *Vibrational Density of States* (VDOS), $g(\omega)$, is constructed. It has been proposed that a small particle size introduces new vibration modes respect to those of a macrocrystal [116, 117, 118]. Based on the calculations of the vibration modes inside a cube with rigid walls by Bolt and Maa [119, 120], Montroll proposed a

“small particle” VDOS as [116]:

$$g(\nu) = \begin{cases} \frac{4\pi V}{c_3} \nu^2 + \frac{\pi S}{2c_2} \nu + \frac{E}{8c_1}, & \text{for } 0 \leq \nu \leq \nu_{max} \\ 0, & \text{otherwise,} \end{cases} \quad (5.1)$$

where the c_j are constants related to the average speed of longitudinal and transverse sound waves in the material, c_l and c_t respectively, as

$$c_j^{-1} = c_l^{-j} + 2c_t^{-j}. \quad (5.2)$$

The symbols V , S and E in eq. 5.1 stand for the particle’s volume, surface and total edge length, respectively. The maximum frequency ν_{max} , on the other hand, is found from the normalization condition of the VDOS according to the Born-von Kármán theory of lattice dynamics. For a material with N primitive unit cells per crystallite and $n = 1$ atoms per primitive unit cell, this condition takes the form:

$$\int_0^{\nu_{max}} g(\nu) d\nu = 3N. \quad (5.3)$$

As proposed by Beyerlein et. al. [115], the maximum wavelength of stationary wave that can be present in an isolated crystallite can be approximated by twice its linear dimension, $\lambda_{max} \approx 2D$. This means that vectors $\mathbf{g} = \mathbf{q}/(2\pi) = (1/\lambda)\hat{\mathbf{q}}$ will have some minimum length $g_{min} = 1/(2D)$. Due to its great analytical simplicity we now assume the Debye lattice model [6], according to which all waves are pure longitudinal or pure transverse, with mean constant velocities c_l and c_t , respectively. Furthermore, for the dispersion of mode $\mathbf{g}j$ it is assumed a simple linear relation

$$\nu_{\mathbf{g}j}(\mathbf{q}) = c_s g, \quad (5.4)$$

where c_s is a constant average velocity given by [3]:

$$\frac{1}{c_s^2} = \frac{1}{3} \left(\frac{1}{c_l^2} + \frac{2}{c_t^2} \right). \quad (5.5)$$

This implies that the minimum vibration frequency for all modes will not be 0 as assumed in eq. 5.1, but

$$\nu_{min} = c_s g_{min} = \frac{c_s}{2D}. \quad (5.6)$$

The normalization condition in eq. 5.3 would then read as

$$3N = \int_{\nu_{min}}^{\nu_{max}} g(\nu) d\nu = \frac{4\pi V}{3c_3} (\nu_{max}^3 - \nu_{min}^3) + \frac{\pi S}{4c_2} (\nu_{max}^2 - \nu_{min}^2) + \frac{E}{8c_1} (\nu_{max} - \nu_{min}), \quad (5.7)$$

from which the maximum allowed frequency can be found as [116]¹:

$$\nu_{max} = \left(\frac{9N'c_3}{4\pi V} \right)^{1/3} \left[1 - \frac{\pi S}{36c_2 N'^{1/3}} \left(\frac{9c_3}{4\pi V} \right)^{2/3} + O(N'^{-2/3}) \right], \quad (5.8)$$

with

$$3N' = 3N + \frac{4\pi V}{3c_3} \nu_{min}^3 + \frac{\pi S}{4c_2} \nu_{min}^2 + \frac{E}{8c_1} \nu_{min}. \quad (5.9)$$

Since we are neglecting dispersion, the number of vectors \mathbf{g} in reciprocal space with norm between g and $g + dg$ can be found directly from the distribution in eq. 5.1 as $c_s \times g(\nu = c_s g)$:

$$\rho(g) = \begin{cases} 4\pi V \left\{ \alpha_3 g^2 + \frac{\alpha_2 S}{8} g + \frac{\alpha_1 E}{32\pi V} \right\}, & \text{for } g_{min} \leq g \leq g_{max} \\ 0, & \text{otherwise,} \end{cases} \quad (5.10)$$

where the dimensionless constants α_j are equal to

$$\alpha_j = \frac{c_s^j}{c_j} = \frac{1 + 2c_l^j/c_t^j}{[(1/3)(1 + 2c_l^2/c_t^2)]^{j/2}}. \quad (5.11)$$

¹A cubic equation on x , $N = ax^3 + bx^2 + cx$, can be solved approximately as $x = (N/a)^{1/3} [1 - 3^{-1} a^{-2/3} b N^{-1/3} + O(N^{-2/3})]$, if $N \gg b$ and $N \gg c$.

In the Born-von Kármán theory the number of \mathbf{g} -vectors in the first Brillouin zone is N , the number of primitive unit cells in the crystal, so the normalization condition for $\rho(g)$ would read as

$$N = \int_{g_{min}}^{g_{max}} \rho(g). \quad (5.12)$$

Using then eq. 5.10 this gives a maximum length for the \mathbf{g} -vectors

$$g_{max} = \left(\frac{3N''}{4\pi V \alpha_3} \right)^{1/3} \left[1 - \frac{\pi \alpha_2 S}{12N''^{1/3}} \left(\frac{3}{4\pi V \alpha_3} \right)^{2/3} + O(N''^{-2/3}) \right], \quad (5.13)$$

with

$$N'' = N + 4\pi V \left\{ \frac{\alpha_3}{3} g_{min}^3 + \frac{\alpha_2 S}{16 V} g_{min}^2 + \frac{\alpha_1 E}{32\pi V} g_{min} \right\}. \quad (5.14)$$

Note that in this way we have approximated the Brillouin zone as a hollow sphere, of inner and outer radius equal to g_{min} and g_{max} , respectively. The allowed \mathbf{g} -vectors will be inside that region only. The volume of this zone is not equal to the volume of the primitive unit cell in reciprocal space, as in the Born-von Kármán theory, but is determined by the assumed VDOS, the normalization condition of the corresponding density $\rho(g)$, and the assumed Debye lattice model.

Warren's model for the TDS powder profiles of cubic symmetry and monatomic macrocrystals is also based on the Debye lattice model, but considers the Brillouin zone as a common sphere, of volume equal to the Brillouin zone volume in the Born-von Kármán theory [3]. The latter is the volume of the primitive unit cell in reciprocal space, so that Warren's Brillouin zone radius is given by $g_{max} = (3nb^3/(4\pi))^{1/3}$, where n is the number of atoms per cubic cell and b is the cubic reciprocal lattice parameter. This means that Warren's VDOS and density of norms of \mathbf{g} -vectors

are given by:

$$g_W(\nu) = \begin{cases} 4\pi V \nu^2 / c_s^3, & \text{for } 0 \leq \nu \leq c_s g_{max} \\ 0, & \text{otherwise,} \end{cases} \quad (5.15)$$

and

$$\rho_W(g) = \begin{cases} 4\pi V g^2, & \text{for } 0 \leq g \leq g_{max} \\ 0, & \text{otherwise.} \end{cases} \quad (5.16)$$

Comparing eqs. 5.1 and 5.10 with eqs. 5.15 and 5.16 we can see that Montrroll's VDOS and $\rho(g)$ density, reduce to the Warren's ones by neglecting the surface effects (particle diameter $D \rightarrow \infty$), and assuming $c_3 = c_s^3$:

$$\begin{cases} c_3 = c_s^3, \\ S = 0, \\ E = 0, \\ g_{min} = 0. \end{cases} \quad (5.17)$$

5.2 The Debye-Waller exponent of nanoparticles

According to the Born-von Kármán theory of lattice dynamics, the Debye-Waller exponent, M , at temperature T for a monatomic material, can be expressed as [3]:

$$\begin{aligned} M = M(\mathbf{s}) &= \frac{h}{8\pi^2 N m} \sum_{\mathbf{g}j} \frac{(2\pi \mathbf{s} \cdot \hat{\mathbf{e}}_{\mathbf{g}j})^2}{\nu_{\mathbf{g}j}} \left(\frac{1}{\text{Exp}[h\nu_{\mathbf{g}j}/(k_B T)] - 1} + \frac{1}{2} \right) \\ &= \frac{s^2 h}{4N m} \sum_{\mathbf{g}j} \frac{\cos^2(\mathbf{s}, \hat{\mathbf{e}}_{\mathbf{g}j})}{\nu_{\mathbf{g}j}} \coth \frac{h\nu_{\mathbf{g}j}}{2k_B T}, \end{aligned} \quad (5.18)$$

where the sum extends over all vibration modes $\mathbf{g}j$. In this equation m is the atom mass, N is the number of primitive unit cells or atoms in the crystallite, h is the Plank constant and k_B is Boltzman constant; $\cos^2(\mathbf{s}, \hat{\mathbf{e}}_{\mathbf{g}j})$

denotes the square of the cosine of the angle between the scattering vector, \mathbf{s} , and the polarization vector of wave \mathbf{g}_j , $\hat{\mathbf{e}}_{\mathbf{g}_j}$. At high temperatures we can make the approximation

$$\coth \frac{h\nu_{\mathbf{g}_j}}{2k_B T} \approx \frac{2k_B T}{h\nu_{\mathbf{g}_j}}, \quad (5.19)$$

transforming eq. 5.18 into

$$M(\mathbf{s}) = \frac{s^2 k_B T}{2Nm} \sum_{\mathbf{g}_j} \frac{\cos^2(\mathbf{s}, \hat{\mathbf{e}}_{\mathbf{g}_j})}{\nu_{\mathbf{g}_j}^2}. \quad (5.20)$$

The Debye lattice model allows for expressing the sum in eq. 5.20 as

$$\begin{aligned} \sum_{\mathbf{g}_j} \frac{\cos^2(\mathbf{s}, \hat{\mathbf{e}}_{\mathbf{g}_j})}{\nu_{\mathbf{g}_j}^2} &= \frac{1}{c_s^2} \sum_{\mathbf{g}} \frac{1}{g^2} \sum_j \cos^2(\mathbf{s}, \hat{\mathbf{e}}_{\mathbf{g}_j}) \\ &= \frac{1}{c_s^2} \sum_{\mathbf{g}} \frac{1}{g^2}, \end{aligned} \quad (5.21)$$

since the versors $\hat{\mathbf{e}}_{\mathbf{g}_j}$, $j = 1, 2, 3$, are mutually perpendicular for any \mathbf{g} . Note that in this step we have lost the directional dependence of the Debye-Waller exponent (and Debye-Waller factor $B = 4M/s^2$), obtaining an *isotropic* approximation of it, $M(s)$:

$$M(\mathbf{s}) \approx M(s) = \frac{s^2 k_B T}{2Nmc_s^2} \sum_{\mathbf{g}} \frac{1}{g^2}. \quad (5.22)$$

We now assume that, despite the small particle size, the density $\Gamma(\mathbf{g})$ of \mathbf{g} -vectors in reciprocal space is high, so we can approximate the sum in eq. 5.22 by an integral over the Brillouin zone. Using eq. 5.10 we therefore

write

$$\begin{aligned}
\sum_{\mathbf{g}} \frac{1}{g^2} &= \int_{BZ} \Gamma(\mathbf{g}) \frac{1}{g^2} d^3 \mathbf{g} = \int_{g_{min}}^{g_{max}} \rho(g) \frac{1}{g^2} dg \\
&= V \left\{ 4\pi\alpha_3(g_{max} - g_{min}) + \frac{\pi\alpha_2}{2} \frac{S}{V} \log \frac{g_{max}}{g_{min}} + \frac{\alpha_1}{8} \frac{E}{V} (g_{min}^{-1} - g_{max}^{-1}) \right\}.
\end{aligned} \tag{5.23}$$

Defining the contribution to the Debye-Waller exponent (and factor) by the volume, surface and edges of the particle, respectively as $(Y_0)_V$, $(Y_0)_S$ and $(Y_0)_E$:

$$\begin{aligned}
(Y_0)_V &= 4\pi\alpha_3(g_{max} - g_{min}) \\
(Y_0)_S &= \frac{\pi\alpha_2}{2} \frac{S}{V} \log \frac{g_{max}}{g_{min}} \\
(Y_0)_E &= \frac{\alpha_1}{8} \frac{E}{V} (g_{min}^{-1} - g_{max}^{-1}),
\end{aligned} \tag{5.24}$$

as well as the factor $A(s)$,

$$A(s) = \frac{s^2 k_B T V}{N m c_s^2}, \tag{5.25}$$

we obtain a nanoparticle Debye-Waller exponent as

$$M(s) = \frac{1}{2} A(s) [(Y_0)_V + (Y_0)_S + (Y_0)_E]. \tag{5.26}$$

Neglecting surface effects, i.e. assuming eqs. 5.17, we will have that $(Y_0)_V = 4\pi g_{max}$ and $(Y_0)_S = (Y_0)_E = 0$. Therefore eq. 5.26 will reduce to

$$M(s) = \frac{3}{2} \frac{s^2 k_B T}{m c_s^2} \frac{1}{g_m^2}, \tag{5.27}$$

which is Warren's expression for the Debye-Waller exponent at high temperatures (taking $T \rightarrow \infty$ in eq. 11.77 of [3]).

5.3 The first-order TDS in reciprocal space

In electron units, the first order TDS intensity in reciprocal space for a monatomic material is given by eq. 2.33:

$$I_1(\mathbf{s}) = \frac{1}{2}f^2e^{-2M} \sum_{\mathbf{g}j} G_{\mathbf{g}j} \{I_o(\mathbf{s} + \mathbf{g}) + I_o(\mathbf{s} - \mathbf{g})\}, \quad (5.28)$$

where

$$I_o(\mathbf{s}) = \sum_m \sum_n \text{Exp}[2\pi i \cdot (\mathbf{r}_m - \mathbf{r}_n)] \quad (5.29)$$

and

$$G_{\mathbf{g}j} = 2\pi^2 s^2 \cos^2(\mathbf{s}, \hat{\mathbf{e}}_{\mathbf{g}j}) \langle a_{\mathbf{g}j}^2 \rangle. \quad (5.30)$$

As already done with eq. 5.19, for high temperatures we can assume equipartition of energy among the modes, $\langle E_{\mathbf{g}j} \rangle = KT$. The mean square vibration amplitude of the atoms when vibrating under mode $\mathbf{g}j$ can then be expressed as

$$\langle a_{\mathbf{g}j}^2 \rangle = \frac{k_B T}{2\pi^2 N m \nu_{\mathbf{g}j}^2}, \quad (5.31)$$

which transforms eq. 5.30 to

$$G_{\mathbf{g}j} = \frac{k_B T s^2}{N m c_s^2} \frac{\cos^2(\mathbf{s}, \hat{\mathbf{e}}_{\mathbf{g}j})}{g^2}, \quad (5.32)$$

using the Debye linear dispersion relation in eq. 5.4. Substituting eq. 5.32 in eq. 5.28 we have

$$\begin{aligned} I_1(\mathbf{s}) &= \frac{1}{2}f^2e^{-2M} \frac{k_B T s^2}{N m c_s^2} \sum_{\mathbf{g}j} \frac{\cos^2(\mathbf{s}, \hat{\mathbf{e}}_{\mathbf{g}j})}{g^2} \{I_o(\mathbf{s} + \mathbf{g}) + I_o(\mathbf{s} - \mathbf{g})\} \\ &= \frac{1}{2}f^2e^{-2M} \frac{k_B T s^2}{N m c_s^2} \sum_{\mathbf{g}} \frac{1}{g^2} \{I_o(\mathbf{s} + \mathbf{g}) + I_o(\mathbf{s} - \mathbf{g})\}, \end{aligned} \quad (5.33)$$

where the sum over the modes has been split as in eq. 5.21. Using the density of \mathbf{g} -vectors in reciprocal space, $\Gamma(\mathbf{g})$, and the approximation of the function I_o with Dirac deltas of eq. 2.20, the sum over the \mathbf{g} in eq.

5.33 can be expressed as

$$\begin{aligned}
\sum_{\mathbf{g}} \frac{1}{g^2} \{I_o(\mathbf{s} + \mathbf{g}) + I_o(\mathbf{s} - \mathbf{g})\} &= \\
&= N_1 N_2 N_3 v_b \int_{BZ} \frac{\Gamma(\mathbf{g})}{g^2} \left\{ \frac{|F|^2}{f^2} \Big|_{\mathbf{s}+\mathbf{g}} \delta^{(3)}(\mathbf{s} + \mathbf{g} - \mathbf{s}_{hkl}) + \right. \\
&\quad \left. \frac{|F|^2}{f^2} \Big|_{\mathbf{s}-\mathbf{g}} \delta^{(3)}(\mathbf{s} - \mathbf{g} - \mathbf{s}_{hkl}) \right\} d^3 \mathbf{g} \\
&= N_1 N_2 N_3 v_b \int_{BZ} \frac{\Gamma(\mathbf{g})}{g^2} \left\{ \frac{|F|^2}{f^2} \Big|_{\mathbf{s}+\mathbf{g}} \delta^{(3)}(\mathbf{g} - [\mathbf{s}_{hkl} - \mathbf{s}]) + \right. \\
&\quad \left. \frac{|F|^2}{f^2} \Big|_{\mathbf{s}-\mathbf{g}} \delta^{(3)}(\mathbf{g} - [\mathbf{s} - \mathbf{s}_{hkl}]) \right\} d^3 \mathbf{g} \\
&= N_1 N_2 N_3 v_b \frac{|F|^2}{f^2} \Big|_{\mathbf{s}_{hkl}} \frac{1}{\|\mathbf{s} - \mathbf{s}_{hkl}\|^2} \{ \Gamma(\mathbf{s}_{hkl} - \mathbf{s}) + \Gamma(\mathbf{s} - \mathbf{s}_{hkl}) \}.
\end{aligned} \tag{5.34}$$

For a cubic monatomic material described with the common cubic unit cell and basis $D = \{\mathbf{a}_1, \mathbf{a}_2, \mathbf{a}_3\}$, we have that $|F|^2 = n^2 f^2$, at the active reciprocal lattice points \mathbf{s}_{hkl} (those where the structure factor does not vanish). Here n is the number of atoms per cubic unit cell ($n = 4$ for fcc and $n = 2$ for bcc). In this case $nN_1N_2N_3$ will be equal to the number of atoms, N , in the parallelepipedon crystallite approximation of edges N_1a_1 , N_2a_2 and N_3a_3 along the directions of D . On the other hand, if v'_a and v'_b are the volumes of the primitive unit cell and that of its reciprocal cell, we have that $v_b = 1/v_a = n/v'_a = nv'_b = nV_{BZ}$, where V_{BZ} is the volume of the Brillouin zone in the Born-von Kármán theory. Therefore we obtain from 5.34

$$\sum_{\mathbf{g}} \frac{1}{g^2} \{I_o(\mathbf{s} + \mathbf{g}) + I_o(\mathbf{s} - \mathbf{g})\} = \frac{NV_{BZ}}{\|\mathbf{s} - \mathbf{s}_{hkl}\|^2} \{ \Gamma(\mathbf{s}_{hkl} - \mathbf{s}) + \Gamma(\mathbf{s} - \mathbf{s}_{hkl}) \}. \tag{5.35}$$

As for the function $\Gamma(\mathbf{g})$, we now assume that the distribution of \mathbf{g} -vectors in reciprocal space has spherical symmetry and thus ²

$$\Gamma(\mathbf{g}) = \Gamma(g) = \frac{\rho(g)}{4\pi g^2}. \quad (5.36)$$

Therefore, substituting the density of g -norms from eq. 5.10, eq. 5.35 continue as

$$\begin{aligned} \sum_{\mathbf{g}} \frac{1}{g^2} \{I_o(\mathbf{s} + \mathbf{g}) + I_o(\mathbf{s} - \mathbf{g})\} &= \frac{NV_{BZ}}{\|\mathbf{s} - \mathbf{s}_{hkl}\|^2} 2 \frac{\rho(\|\mathbf{s} - \mathbf{s}_{hkl}\|)}{4\pi \|\mathbf{s} - \mathbf{s}_{hkl}\|^2} \\ &= 2NV_{BZ}V \left\{ \frac{\alpha_3}{\|\mathbf{s} - \mathbf{s}_{hkl}\|^2} + \frac{\alpha_2}{8} \frac{S}{V} \frac{1}{\|\mathbf{s} - \mathbf{s}_{hkl}\|^3} + \frac{\alpha_1}{32\pi} \frac{E}{V} \frac{1}{\|\mathbf{s} - \mathbf{s}_{hkl}\|^4} \right\}, \end{aligned} \quad (5.37)$$

for $g_{min} \leq \|\mathbf{s} - \mathbf{s}_{hkl}\| \leq g_{max}$, and

$$\sum_{\mathbf{g}} \frac{1}{g^2} \{I_o(\mathbf{s} + \mathbf{g}) + I_o(\mathbf{s} - \mathbf{g})\} = 0 \quad (5.38)$$

²In general, the relation between the VDOS, $g(w)$, and the dispersion relations of modes $\mathbf{q}j$ is given by the expression

$$g(w) = \sum_{i=1}^3 \iint_{w_j=w} \frac{\Gamma(\mathbf{q})}{|\nabla w_j(\mathbf{q})|} dS_{w_j},$$

where the integration is made over the surface in reciprocal space where mode j has constant frequency $w = 2\pi\nu$. $|\nabla w_j(\mathbf{q})|$ means the norm of the gradient of the scalar evaluated vector function (dispersion relation) $w_j(\mathbf{q})$. See [121], section 3.5.1, for details. Therefore, measuring the VDOS as well as the dispersion relations through suitable techniques, like Inelastic X-ray or Neutron Scattering (IXS, INS)[122], it is possible, in principle, to calculate the density of $\mathbf{q} = 2\pi\mathbf{g}$ vectors, $\Gamma(\mathbf{q})$. This density would be precise for a single crystal study, or an average, for a polycrystalline sample, in which also the determined dispersion relation would be an average.

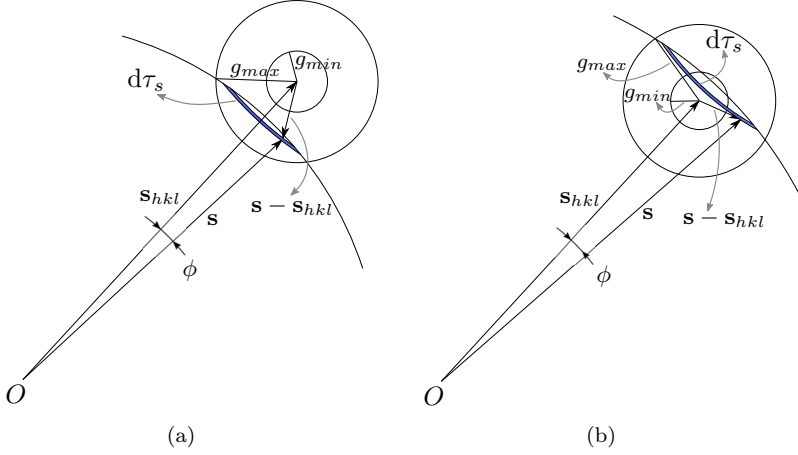


Figure 5.1: Hollow spherical region where the TDS intensity is concentrated. The intersection surface between an s -sphere and the hollow sphere has axial symmetry respect to \mathbf{s}_{hkl} . (a) A case where $g_{min} \leq |\mathbf{s} - \mathbf{s}_{hkl}| \leq g_{max}$. (b) A case where $0 \leq |\mathbf{s} - \mathbf{s}_{hkl}| < g_{min}$.

otherwise. Substituting this result in eq. 5.33, we express the first order TDS at reciprocal space point \mathbf{s} near \mathbf{s}_{hkl} , $I_1(\mathbf{s}) = I_1(\mathbf{s}, \mathbf{s}_{hkl})$, as

$$I_1(\mathbf{s}, \mathbf{s}_{hkl}) = \frac{k_B T V_{BZ} V}{m c_s^2} f^2 e^{-2M} s^2 \left\{ \frac{\alpha_3}{\|\mathbf{s} - \mathbf{s}_{hkl}\|^2} + \frac{\alpha_2 S}{8 V} \frac{1}{\|\mathbf{s} - \mathbf{s}_{hkl}\|^3} + \frac{\alpha_1 E}{32\pi V} \frac{1}{\|\mathbf{s} - \mathbf{s}_{hkl}\|^4} \right\}, \quad (5.39)$$

for the cases $g_{min} \leq \|\mathbf{s} - \mathbf{s}_{hkl}\| \leq g_{max}$. For $\|\mathbf{s} - \mathbf{s}_{hkl}\| \notin [g_{min}, g_{max}]$, $I_1(\mathbf{s}, \mathbf{s}_{hkl}) = 0$. This means that the first order TDS is concentrated in hollow spheres centered at the reciprocal space active lattice points \mathbf{s}_{hkl} , as shown in Figure 5.1.

5.4 The first order powder TDS

Let's call $I_{TDS1}^{hkl}(s)$ the first order TDS intensity profile, corresponding to the TDS scattered intensity around the reciprocal space lattice point \mathbf{s}_{hkl} . To find it, we must substitute eq. 5.39 in the powder average expression in eq. 2.42:

$$\begin{aligned}
 I_{TDS1}^{hkl}(s) &= \frac{N_c}{4\pi s^2} \iint_{s\text{-sphere}} I_{TDS1}(\mathbf{s}) d^2\mathbf{s} \\
 &= \frac{N_c}{4\pi s^2} \iint_{s\text{-sphere}} \sum_{hkl} I_1(\mathbf{s}, \mathbf{s}_{hkl}) d^2\mathbf{s} \\
 &= \frac{N_c p_{hkl}}{4\pi s^2} \iint_{\tau_s} I_1(\mathbf{s}, \mathbf{s}_{hkl}) d^2\mathbf{s}.
 \end{aligned} \tag{5.40}$$

Here N_c is the number of crystallites in the powder sample, p_{hkl} is the multiplicity of the hkl reflection, and τ_s is the intersection of the s -sphere and the hollow spherical region where the TDS is concentrated (see Figure 5.1). From eq. 5.39 it can be seen that we only need to solve integrals of the type

$$\int_{\tau_s} \frac{d^2\mathbf{s}}{\|\mathbf{s} - \mathbf{s}_{hkl}\|^i}, \tag{5.41}$$

with $i = 2, 3, 4$. Thanks to the axial symmetry of the involved integrands and τ_s , respect to \mathbf{s}_{hkl} , we can integrate eq. 5.40 without using the tangent plane approximation. We will follow the approach of [123]. Let's call ϕ the angle between \mathbf{s} and \mathbf{s}_{hkl} . Because of the axial symmetry we can write

$$d^2\mathbf{s} = \|\mathbf{s}\| d\phi 2\pi \|\mathbf{s}\| \sin \phi = 2\pi s^2 \sin \phi d\phi. \tag{5.42}$$

Defining $x = \|\mathbf{s} - \mathbf{s}_{hkl}\|$, we have that

$$x^2 = s^2 + s_{hkl}^2 - 2s s_{hkl} \cos \phi, \tag{5.43}$$

which can be differentiated and substituted in eq. 5.42 to obtain

$$d^2\mathbf{s} = \frac{2\pi s}{s_{hkl}} x dx. \tag{5.44}$$

As can be seen in Figure 5.1, when spanning all the area elements in eq. 5.42, x will go from a given minimum x_{min} to a maximum $x_{max} = g_{max}$. The minimum value of x depends on the s value where we are evaluating the TDS as

$$x_{min} = \begin{cases} |s - s_{hkl}|, & \text{for } g_{min} \leq |s - s_{hkl}| \leq g_{max} \\ g_{min}, & \text{for } 0 \leq |s - s_{hkl}| < g_{min}. \end{cases} \quad (5.45)$$

In this way, the integrals in eq. 5.41 transform to

$$\int_{\tau_s} \frac{d^2 \mathbf{s}}{\|\mathbf{s} - \mathbf{s}_{hkl}\|^i} = \frac{2\pi s}{s_{hkl}} \int_{x_{min}}^{g_{max}} x^{1-i} dx, \quad (5.46)$$

with $i = 2, 3, 4$, which can be easily solved to give a powder TDS of order one:

$$I_{TDS1}^{hkl}(s) = \frac{N_c p_{hkl} k_B T V_{BZ} V}{2 s_{hkl} m c_s^2} f^2 e^{-2M} s \left\{ \alpha_3 \log \frac{g_{max}}{x_{min}} + \frac{\alpha_2 S}{8 V} (x_{min}^{-1} - g_{max}^{-1}) + \frac{\alpha_1 E}{64\pi V} (x_{min}^{-2} - g_{max}^{-2}) \right\}. \quad (5.47)$$

Note that this expression is valid for $s_{hkl} - g_{max} \leq s \leq s_{hkl} + g_{max}$. Outside this interval $I_{TDS1}^{hkl}(s) = 0$. We can substitute the temperature in eq. 5.47 from eq. 5.26 to obtain:

$$I_{TDS1}^{hkl}(s) = \frac{N_c N p_{hkl} V_{BZ}}{(Y_0)_V + (Y_0)_S + (Y_0)_E} \frac{f^2 e^{-2M} M}{s s_{hkl}} \left\{ \alpha_3 \log \frac{g_{max}}{x_{min}} + \frac{\alpha_2 S}{8 V} (x_{min}^{-1} - g_{max}^{-1}) + \frac{\alpha_1 E}{64\pi V} (x_{min}^{-2} - g_{max}^{-2}) \right\}. \quad (5.48)$$

Equation 5.48 is equivalent to eq. 26 of Beyerlein et. al. [115] correcting the coefficients of S/V and E/V in that work.

Neglecting surface effects through eqs. 5.17, the volume of the Brillouin zone will be $(4/3)\pi g_m^3$ and eq. 5.48 will reduce to Warren's first order

powder TDS [3]:

$$I_{TDS1}^{hkl}(s) = N_c N f^2 e^{-2M} 2M \frac{g_{max}^2}{6} \frac{p_{hkl}}{s s_{hkl}} \log \frac{g_{max}}{|s - s_{hkl}|}. \quad (5.49)$$

5.5 Higher order TDS

In electron units, the TDS intensity of order l is given by eq. 2.31:

$$I_{TDSl}(\mathbf{s}) = f^2 e^{-2M} \sum_m \sum_n \text{Exp}[2\pi i \mathbf{s} \cdot \mathbf{r}_{mn}] \frac{Y_{mn}^l}{l!}. \quad (5.50)$$

where \mathbf{r}_{mn} is the vector separation between atoms m and n , $\mathbf{r}_{mn} = \mathbf{r}_m - \mathbf{r}_n$, and Y_{mn} is given by

$$Y_{mn} = \sum_{\mathbf{g}j} G_{\mathbf{g}j} \cos 2\pi \mathbf{g} \cdot \mathbf{r}_{mn}. \quad (5.51)$$

Substituting $G_{\mathbf{g}j}$ from eq. 5.30 (we use the Debye lattice model and assume equipartition of energy) we have

$$Y_{mn} = \frac{k_B T s^2}{NM c_s^2} \sum_{\mathbf{g}} \frac{\cos 2\pi \mathbf{g} \cdot \mathbf{r}_{mn}}{g^2}. \quad (5.52)$$

As before, we can solve the sum in eq. 5.52 approximating it by an integral over the hollow sphere approximation of the Brillouin zone, using the density $\Gamma(\mathbf{g})$ in eq. 5.36. Adopting a spherical coordinate system with

\mathbf{r}_{mn} oriented along the z -axis we write [3]:

$$\begin{aligned}
\sum_{\mathbf{g}} \frac{\cos 2\pi \mathbf{g} \cdot \mathbf{r}_{mn}}{g^2} &= \int_{BZ} \Gamma(\mathbf{g}) \frac{\cos 2\pi \mathbf{g} \cdot \mathbf{r}_{mn}}{g^2} d^3 \mathbf{g} \\
&= \int_0^\pi \int_0^{2\pi} \int_{g_{min}}^{g_{max}} \frac{\rho(g)}{4\pi g^2} \frac{1}{g^2} \cos\{2\pi g, r_{mn} \cos \theta\} g^2 \sin \theta dg d\theta d\phi \\
&= \int_{g_{min}}^{g_{max}} \frac{\rho(g)}{g^2} \text{Sinc}(2\pi g r_{mn}) dg,
\end{aligned} \tag{5.53}$$

where $\text{Sinc}(x) = \sin x/x$, and $\rho(g)$ is given by eq. 5.10. Using the SinIntegral and CosineIntegral function definitions:

$$\begin{aligned}
\text{Si}(x) &= \int_0^x \frac{\sin t}{t} dt \\
\text{Ci}(x) &= - \int_x^\infty \frac{\cos t}{t} dt,
\end{aligned} \tag{5.54}$$

as well as the definitions $a = 2\pi r_{mn} g_{max}$, $b = 2\pi r_{mn} g_{min}$ and

$$\begin{aligned}
(Y_{mn})_V &= \frac{2\alpha_3}{r_{mn}} [\text{Si}(a) - \text{Si}(b)] \\
(Y_{mn})_S &= \frac{\pi\alpha_2}{2} \frac{S}{V} [\text{Ci}(a) - \text{Ci}(b) - \text{Sinc}(a) + \text{Sinc}(b)] \\
(Y_{mn})_E &= \frac{\pi r_{mn} \alpha_1}{8} \frac{E}{V} \left[\frac{\cos b}{b} - \frac{\cos a}{a} - \text{Si}(a) + \text{Si}(b) + \frac{\text{Sinc}(b)}{b} - \frac{\text{Sinc}(a)}{a} \right],
\end{aligned} \tag{5.55}$$

the integral in eq. 5.53 can be solved to give

$$Y_{mn} = A(s) [(Y_{mn})_V + (Y_{mn})_S + (Y_{mn})_E], \tag{5.56}$$

where $A(s)$ is given by eq. 5.25. It can be demonstrated that in the limit $r_{mn} \rightarrow 0$ eqs. 5.55 reduce to eqs. 5.24.

Using the powder average with eq. 5.50, the l th-order powder TDS is

given by

$$\begin{aligned}
I_{TDSl}(s) &= \frac{N_c}{4\pi s^2} \int_{s\text{-sphere}} I_{TDSl}(\mathbf{s}) d^2\mathbf{s} \\
&= \frac{N_c}{4\pi s^2} f^2 e^{-2M} \sum_m \sum_n \int_{s\text{-sphere}} \text{Exp}[2\pi i \mathbf{s} \cdot \mathbf{r}_{mn}] d^2\mathbf{s} \frac{Y_{mn}^l}{l!}.
\end{aligned} \tag{5.57}$$

If \mathbf{s}_r is the vector ending at each observation point, \mathbf{s} , and starting at the nearest active reciprocal lattice point, \mathbf{s}_{hkl} , the integrand in eq. 5.57 is equal to $\text{Exp}[2\pi i \mathbf{s}_r \cdot \mathbf{r}_{mn}]$. For any fixed length s_r , all vectors \mathbf{s}_r involved in this integration will take most of the orientations relative to \mathbf{r}_{mn} , so we can approximate and substitute the integrand by such mean [3]:

$$\begin{aligned}
\text{Exp}[2\pi i \mathbf{s}_r \cdot \mathbf{r}_{mn}] &\approx \langle \text{Exp}[2\pi i s_r r_{mn} \cos \theta] \rangle_{\theta \in [0, \pi]} \\
&= \frac{1}{4\pi s_r^2} \int_0^{2\pi} \int_0^\pi \text{Exp}[2\pi i s_r r_{mn} \cos \theta] s_r^2 \sin \theta d\theta d\phi \tag{5.58} \\
&= \text{Sinc}(2\pi r_{mn} s_r),
\end{aligned}$$

where we have oriented the z -axis along \mathbf{r}_{mn} . In general, supposing that the Bragg intensity is concentrated at the active reciprocal lattice points \mathbf{s}_{hkl} , the l th-order TDS intensity at \mathbf{s} will be not null only if there is some \mathbf{s}_{hkl} such that [3, 6]:

$$\mathbf{s}_{hkl} = \mathbf{s} + \sum_{i=1}^l \mathbf{g}_i, \tag{5.59}$$

with the \mathbf{g}_i in the first Brillouin zone. This is called an l -phonons scattering process. This means that the maximum distance s_r in eq. 5.58 will be $g'_{max} = l g_{max}$, according to our Brillouin zone model. Nevertheless, extending the TDS l th-order contributions until such distance from the active reciprocal lattice points, will most likely overestimate the total TDS intensity at any s . This is because the probability of an l -phonons scattering process actually decrease with the increase of l , whereas our

development here implicitly considers it as constant ³. To reach a compromise between these two effects we prefer to consider an average constant extension $g'_{max} > g_{max}$, as an additional model parameter for the higher order TDS intensities ($l \geq 2$).

To solve the integral in eq. 5.57 we now use, as before, the intensity around only one point of reciprocal space and multiply by its multiplicity factor p_{hkl} :

$$\begin{aligned}
 I_{TDSl}(s) &= \frac{N_c p_{hkl}}{4\pi s^2} f^2 e^{-2M} \sum_m \sum_n \iint_{\Upsilon_s} \text{Exp}[2\pi i \mathbf{s} \cdot \mathbf{r}_{mn}] d^2 \mathbf{s} \frac{Y_{mn}^l}{l!} \\
 &\approx \frac{N_c p_{hkl}}{4\pi s^2} f^2 e^{-2M} \sum_m \sum_n \iint_{\Upsilon_s} \text{Sinc}(2\pi r_{mn} x) d^2 \mathbf{s} \frac{Y_{mn}^l}{l!}.
 \end{aligned} \tag{5.60}$$

Here Υ_s is the intersection of the s -sphere and a hollow sphere of inner radius g_{min} and outer radius g'_{max} . The integral over Υ_s is solved as in eq. 5.46 for τ_s :

$$\begin{aligned}
 \iint_{\Upsilon_s} \text{Sinc}(2\pi r_{mn} x) d^2 \mathbf{s} &= \frac{2\pi s}{s_{hkl}} \int_{x_{min,l}}^{g'_{max}} \text{Sinc}(2\pi r_{mn} x) x dx \\
 &= \frac{s}{2\pi r_{mn}^2 s_{hkl}} [\cos(2\pi r_{mn} x_{min,l}) - \cos(2\pi r_{mn} g'_{max})],
 \end{aligned} \tag{5.61}$$

where $x_{min,l}$ now is given by

$$x_{min,l} = \begin{cases} |s - s_{hkl}|, & \text{for } g_{min} \leq |s - s_{hkl}| \leq g'_{max} \\ g_{min}, & \text{for } |s - s_{hkl}| < g_{min}. \end{cases} \tag{5.62}$$

³See for instance Warren's treatment of the second order TDS at [3], p. 165-167. Warren's final expression for the second order TDS in reciprocal space (eq. 11.42) takes into account the decrease in the probability of a two-phonons scattering process by means of a function, Φ_{hkl} , depending on the volume of the intersection region between two spheres of radius g_{max} .

Table 5.1: Number of neighbors and radius (in units of unit cell) of the inner coordination shells, for fcc and bcc metals.

shell		1	2	3	4	5	6	7	8	9	10
fcc	mult.	12	6	24	12	24	8	48	6	36	24
	radius [u.c]	$1/\sqrt{2}$	1	$\sqrt{3}/2$	$\sqrt{2}$	$\sqrt{5}/2$	$\sqrt{3}$	$\sqrt{7}/2$	2	$3/\sqrt{2}$	$\sqrt{5}$
bcc	mult.	8	6	12	24	8	6	24	24	24	32
	radius [u.c]	$\sqrt{3}/2$	1	$\sqrt{2}$	$\sqrt{11}/2$	$\sqrt{3}$	2	$\sqrt{19}/2$	$\sqrt{5}$	$\sqrt{6}$	$3\sqrt{3}/2$

Substituting eq. 5.61 and 5.56 in eq. 5.60 we obtain

$$\begin{aligned}
 I_{TDSl}^{hkl}(s) &= \frac{N_c P_{hkl}}{2} \frac{A(s)^l}{l!} \frac{f^2 e^{-2M}}{s s_{hkl}} \\
 &\times \sum_m \sum_n \left[\frac{\cos(2\pi r_{mn} x_{min,l}) - \cos(2\pi r_{mn} g'_{max})}{(2\pi r_{mn})^2} \right. \\
 &\left. \times \{(Y_{mn})_V + (Y_{mn})_S + (Y_{mn})_E\}^l \right]. \quad (5.63)
 \end{aligned}$$

The sum over m and n in eq. 5.63 can be transformed to a sum over the coordination shells of each atom in the particle [3]. Calling m_i the number of neighbors at shell i , d_i its radius, and ignoring the sub-population of near-surface atoms' shells, we can write

$$\begin{aligned}
 &\sum_m \sum_n \frac{\cos(2\pi r_{mn} x_{min,l}) - \cos(2\pi r_{mn} g'_{max})}{(2\pi r_{mn})^2} \{(Y_{mn})_V + (Y_{mn})_S + (Y_{mn})_E\}^l \\
 &= \sum_m \sum_{i=0}^{\infty} m_i \frac{\cos(2\pi d_i x_{min,l}) - \cos(2\pi d_i g'_{max})}{(2\pi d_i)^2} \{(Y_i)_V + (Y_i)_S + (Y_i)_E\}^l \\
 &= \sum_m \frac{g_{max}^2 - x_{min}^2}{2} \{(Y_0)_V + (Y_0)_S + (Y_0)_E\}^l \\
 &\quad + \sum_m \sum_{i=1}^{\infty} \left[m_i \frac{\cos(2\pi d_i x_{min,l}) - \cos(2\pi d_i g'_{max})}{(2\pi d_i)^2} \right. \\
 &\quad \left. \times \{(Y_i)_V + (Y_i)_S + (Y_i)_E\}^l \right], \quad (5.64)
 \end{aligned}$$

where we have used the fact that $m_0 = 1$ and

$$\lim_{d_i \rightarrow 0} \frac{\cos(2\pi d_i x_{min,l}) - \cos(2\pi d_i g'_{max})}{(2\pi d_i)^2} = \frac{g'^2_{max} - x^2_{min}}{2}. \quad (5.65)$$

Replacing the sum over all atoms m in eq. 5.64 with a multiplication by the number of atoms N of the particle, and substituting this in eq. 5.63, we therefore obtain for the l th-order powder TDS:

$$\begin{aligned} I_{TDSl}^{hkl}(s) &= \frac{N_c p_{hkl}}{2} \frac{A(s)^l}{l!} \frac{f^2 e^{-2M}}{s s_{hkl}} N \left\{ \frac{g'^2_{max} - x^2_{min}}{2} [(Y_0)_V + (Y_0)_S + (Y_0)_E]^l \right. \\ &\quad \left. + \sum_{i=1}^{\infty} m_i \frac{\cos(2\pi d_i x_{min,l}) - \cos(2\pi d_i g'_{max})}{(2\pi d_i)^2} [(Y_i)_V + (Y_i)_S + (Y_i)_E]^l \right\}. \end{aligned} \quad (5.66)$$

Expression 5.66 is valid for $s_{hkl} - g'_{max} \leq s \leq s_{hkl} + g'_{max}$. Outside this interval $I_{TDSl}^{hkl}(s) = 0$. We can substitute the factor $A(s)$ in eq 5.66 from eq. 5.26 to obtain:

$$\begin{aligned} I_{TDSl}^{hkl}(s) &= \frac{N_c p_{hkl}}{2} \frac{(2M)^l}{l!} \frac{f^2 e^{-2M}}{s s_{hkl}} N \left\{ \frac{g'^2_{max} - x^2_{min}}{2} \right. \\ &\quad \left. + \sum_{i=1}^{\infty} m_i \frac{\cos(2\pi d_i x_{min,l}) - \cos(2\pi d_i g'_{max})}{(2\pi d_i)^2} \left[\frac{(Y_i)_V + (Y_i)_S + (Y_i)_E}{(Y_0)_V + (Y_0)_S + (Y_0)_E} \right]^l \right\}. \end{aligned} \quad (5.67)$$

Equation 5.67 is equivalent to eq. 42 of Beyerlein et. al. [115], placing the factor N outside the curly brackets and considering $g_{max} = g'_{max}$ in that work.

As before, neglecting surface effects reduces eq. 5.67 to the l th-order powder TDS of monatomic macrocrystals of Warren (see [3], p. 196-198):

$$\begin{aligned} I_{TDSl}^{hkl}(s) &= \frac{N_c p_{hkl}}{2} \frac{(2M)^l}{l!} \frac{f^2 e^{-2M}}{s s_{hkl}} N \left\{ \frac{g'^2_{max} - |s - s_{hkl}|^2}{2} \right. \\ &\quad \left. + \sum_{i=1}^{\infty} m_i \frac{\cos(2\pi d_i |s - s_{hkl}|) - \cos(2\pi d_i g'_{max})}{(2\pi d_i)^2} \left[\frac{\text{Si}(2\pi d_i g_{max})}{2\pi d_i g_{max}} \right]^l \right\}. \end{aligned} \quad (5.68)$$

The number of atoms in each coordination shell (multiplicity), as well as

their radius in unit cells for fcc and bcc metals, are shown in Table 5.1.

Summarizing, the total powder TDS intensity in this work will be given by eqs. 5.48 and 5.67 as

$$I_{TDS}(s) = \sum_{hkl} \left\{ I_{TDS1}^{hkl}(s) + \sum_{l=2}^{l_{max}} I_{TDSl}^{hkl}(s) \right\}. \quad (5.69)$$

In practical cases we can consider $l_{max} = 4$ since higher order TDS contributions will be much smaller, due to the factor $l!$ in the denominator of eq. 5.67 [115].

5.6 Powder TDS calculation from a Molecular Dynamics vibration trajectory

Powder TDS patterns were computed using the powder average (eq. 2.42), with the TDS intensity in reciprocal space given by eq. 2.35. Omitting the number of atoms, taking the intensity in electron units, and approximating the integral by a Riemann sum over N elements of equal area α , we have:

$$\begin{aligned} I_{TDS}(s) &= \frac{1}{4\pi s^2} \iint_{s\text{-sphere}} I_{TDS}(\mathbf{s}) d^2\mathbf{s} \approx \frac{1}{4\pi s^2} \sum_{i=1}^N I_{TDS}(\mathbf{s}_i) \alpha(\mathbf{s}_i) \\ &= \frac{\alpha}{4\pi s^2} \sum_{i=1}^N (\langle |\mathbb{F}(\mathbf{s}_i)|^2 \rangle - |\langle \mathbb{F}(\mathbf{s}_i) \rangle|^2) \\ &= \frac{1}{N} \sum_{i=1}^N (\langle |\mathbb{F}(\mathbf{s}_i)|^2 \rangle - |\langle \mathbb{F}(\mathbf{s}_i) \rangle|^2). \end{aligned} \quad (5.70)$$

The $\langle \rangle$ in this equation are time averages of the particle structure factor, \mathbb{F} , defined in eq. 2.3, which introduce the dynamic disorder caused by the thermal vibrations:

$$\mathbb{F}(\mathbf{s}_i) = \mathbb{F}(\mathbf{s}_i, t) = \sum_l f_l \text{Exp}[2\pi i \mathbf{s}_i \cdot \mathbf{R}_l(t)]. \quad (5.71)$$

The trajectories $\mathbf{R}_i(t)$ of every atom are obtained from a Molecular Dynamics simulation, with the settings specified in section 4.7. Expanding the exponential in eq. 5.71 it can be demonstrated that

$$\begin{aligned} \langle |\mathbb{F}(\mathbf{s})|^2 \rangle &= \langle |\mathbb{F}(-\mathbf{s})|^2 \rangle \\ \langle \mathbb{F}(\mathbf{s}) \rangle^2 &= \langle \mathbb{F}(-\mathbf{s}) \rangle^2. \end{aligned} \quad (5.72)$$

Therefore, the computation of the square mean and mean square structure factors in eq. 5.70 need to be done only for half of the \mathbf{s}_i . Labeling as \mathbf{s}_j those vectors on one side of a plane passing through the center of the s -sphere, eq. 5.70 can therefore be written as

$$I_{TDS}(s) = \frac{1}{2N} \sum_{j=1}^{N/2} (\langle |\mathbb{F}(\mathbf{s}_j)|^2 \rangle - |\langle \mathbb{F}(\mathbf{s}_j) \rangle|^2). \quad (5.73)$$

Note that considering only $\langle |\mathbb{F}(\mathbf{s})|^2 \rangle$ in eq. 5.70 or 5.73, we obtain the total diffracted powder intensity, carrying the effects of thermal vibrations. Such pattern will be equivalent to the mean of the patterns computed (with the Debye equation) over the single snapshots composing the Molecular Dynamics trajectory of the particle. In the limit of infinitely small elements of area ($N \rightarrow \infty$, the sum transforms into an integral) they will be equal, as can be deduced exchanging the sum and the average operations and using eqs. 2.43 and 2.36. The convenience of choosing a discretization of the s -sphere where all surface elements have equal area is evident from the compact form of eq. 5.73. One way for attaining this is using the Hierarchical Equal Area and isoLatitude Pixelization of a sphere, HEALPix [124]. See Figure 5.2. This discretization procedure is specially designed for the efficient analysis of large data sets distributed on a spherical domain. The discretization starts with twelve curvilinear quadrilateral pixels of equal area, the *base-resolution* pixels. In each discretization step each pixel is sub-divided into four smaller pixels of equal area, such that a hierarchical tree structure is obtained. Discretization steps are distinguished by their *resolution parameter*, N_{side} , defining the number of divisions along the base-resolution pixels. In each discretization step the total number

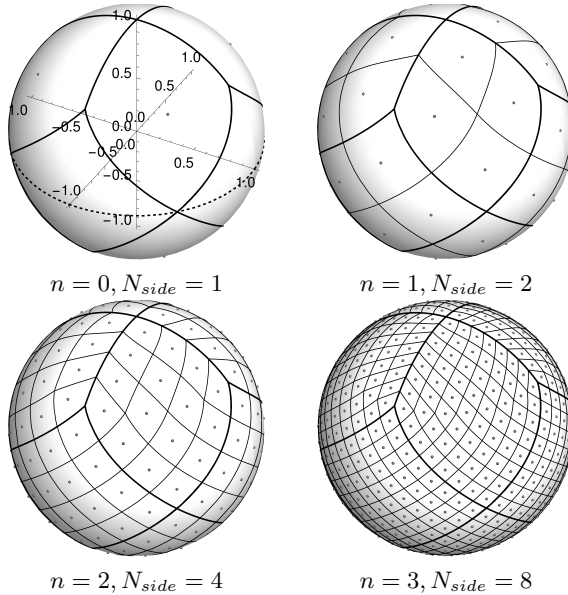


Figure 5.2: Unit sphere surface tessellation with the HEALPix method, for order parameter $n = 0, 1, 2$ and 3 . For order $n = 0$, axes are shown as well as the equatorial plane with a dashed line. Thicker lines delimit the base resolution pixels in the four cases. See [124] for details.

of pixels will be $12N_{side}^2$, and their area will be $\pi/(3N_{side}^2)$, considering a sphere of unit radius. Pixels centers will be placed on rings of constant latitude (constant θ spherical coordinated) and on each ring they will be equidistant in azimuth (constant separation in ϕ spherical coordinate). They are classified in *polar caps* pixels, having $|\cos\theta| > 2/3$, and *equatorial belt* pixels, having $|\cos\theta| \leq 2/3$. Their positions will have mirror symmetry respect to the equatorial plane, so only equations for pixels in the north hemisphere and the equatorial plane need to be specified. These equations are written in terms of a ring index, i , and a pixel-in-ring index, j , specifying, respectively, the ring of the pixel and its rank inside the ring. For the polar cap pixels in the north hemisphere, i will run from 1 to $N_{side} - 1$, and j from 1 to four times the pixel's ring index i . For the equatorial belt pixels in the north hemisphere (excluding those in the

equatorial plane), i will run from N_{side} to $2N_{side} - 1$, and j from 1 to $4N_{side}$. Equatorial plane pixels will have $i = 2N_{side}$, and j running from 1 to $4N_{side}$ as well. With these limits, the spherical coordinates $\theta \in [0, \pi]$ and $\phi \in [0, 2\pi]$ of the pixels (their centers) will be given by [124]:

$$\{\theta, \phi\} = \left\{ \arccos \left(1 - \frac{i^2}{3N_{side}^2} \right), \frac{\pi}{2i} \left(j - \frac{1}{2} \right) \right\}, \quad (5.74)$$

for the north polar cap pixels, and by

$$\{\theta, \phi\} = \left\{ \arccos \left(\frac{4}{3} - \frac{2i}{3N_{side}} \right), \frac{\pi}{2N_{side}} \left(j - \frac{\text{Mod}2[i - N_{side} + 1]}{2} \right) \right\}, \quad (5.75)$$

for the north equatorial belt pixels and those in the the equatorial plane. The function $\text{Mod}2[x]$ returns the rest of the division of its argument by two.

According to eq. 5.73 the powder TDS intensity, as well as the total intensity, can be found computing only at the north polar cap, equatorial belt and equatorial plane points. From what has been said above, this amounts to

$$N_{comp} = \frac{12N_{side}^2 - 4N_{side}}{2} + 4N_{side} = 6N_{side}^2 + 2N_{side} \quad (5.76)$$

computation points. The area α subtended over a sphere of radius s by a pixel over the unit sphere is given by

$$\alpha = \frac{\pi s^2}{3N_{side}^2}. \quad (5.77)$$

Therefore, to guarantee a tessellation of the surface of a s -sphere with elements of area equal or smaller than α , it is needed a resolution parameter N_{side} such that

$$N_{side} \geq \sqrt{\frac{\pi s^2}{3\alpha}}. \quad (5.78)$$

It is convenient to define an integer *order parameter*, $n = 0, 1, 2, \dots$, such that $N_{side} = 2^n$. With this, the minimum tessellation order needed to

discretize the surface of a sphere of radius s , with elements of area equal or smaller than α is given by

$$n = \text{Ceil} \left[\frac{1}{2} \log_2 \frac{\pi s^2}{3\alpha} \right], \quad (5.79)$$

and the corresponding number of computation point by

$$N_{comp}(n) = N_{comp}(\alpha, s) = 2^{n+1}(3 \times 2^n + 1) \sim 2^{2n+2}. \quad (5.80)$$

The $\text{Ceil}[x]$ function in eq. 5.79 returns the smallest integer greater or equal to its argument. From eq. 5.70 we can see that α has to be kept small enough to ensure negligible errors in the approximation of the powder integral with a Riemann sum. Not doing so may result in a considerable underestimation of the total intensity near the Bragg peak positions. This was indeed the criteria used in this work for choosing an appropriate resolution parameter in each case. Namely, the maximum area element α was lowered until the total intensity computed with eq. 5.70, or 5.73, was practically equal to that computed by means of the Debye equation over the trajectory snapshots and then averaging over time. For the spherical particles of diameter 12, 18 and 24 unit cells examined in the next section, an area $\alpha = 4 \times 10^{-4} \text{ \AA}^{-2}$ resulted good enough, whereas for those with diameter 30 unit cells, an $\alpha = 1 \times 10^{-4} \text{ \AA}^{-2}$ was needed, due to the increased concentration of the Bragg intensity around the reciprocal lattice points. Figure 5.3 show plots of the number of computation points in eq. 5.80 for these two values of α . As can be seen, the number of computation points in reciprocal space is very sensible to this parameter. Choosing a proper value may easily result in more than 10^7 computation points, when building a powder pattern with s between 0.2 and 2.0 \AA^{-1} , and a step of 0.002 \AA^{-1} (a small step is also needed for well populated peak profiles). Because of this, a parallel program implementing eq. 5.73 is highly recommended. For the present thesis an Open MP program was written and ran in single multi-cores nodes of the Italian supercomputing center, CINECA.

Last, it is worth mentioning that the methodology described above is specially designed for the construction of powder patterns through the in-

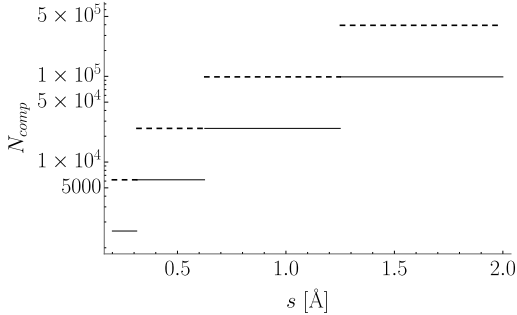


Figure 5.3: Number of computation points for $\alpha = 1 \times 10^{-4} \text{ \AA}^{-2}$ (solid line) and $\alpha = 1 \times 10^{-4} \text{ \AA}^{-2}$ (dashed line). See text for details.

tegration of the intensity in reciprocal space. The intensity is computed exactly at the integration points, and the HEALPix tessellation guarantees a constant minimum density of them over the integration surface (sphere), throughout all the $s = 2 \sin \theta / \lambda$. This is a key difference with other known software which compute total [125, 126, 127, 107] and diffuse [8, 128] powder intensity, but integrating a reciprocal space intensity map constructed over a square homogeneous grid of points, or other not homogeneous over the s -spheres.

5.7 Beyerlein et. al. TDS model test

In order to test Beyerlein et. al. TDS model [115], we computed the powder TDS intensity as described in section 5.6 and compared against eq. 5.69. We particularly examined the cases of Pd and Al spherical particles of nominal diameter 12, 18, 24 and 30 unit cells. Results for Pd and Al particles are shown in Figures 5.4 and 5.5, respectively. Table 5.2 summarizes the fits parameter values for both metals. To be able to fit the data using Beyerlein's original model, it was necessary to allow for independent Debye-Waller parameters, $B_{iso} = M(s/2)^{-2} = 8\pi^2 \langle u_s^2 \rangle$ (see eq. 2.9), for each hkl TDS profile. This highlights an anisotropic behavior of the powder TDS of nanoparticles that is not considered by Beyerlein's

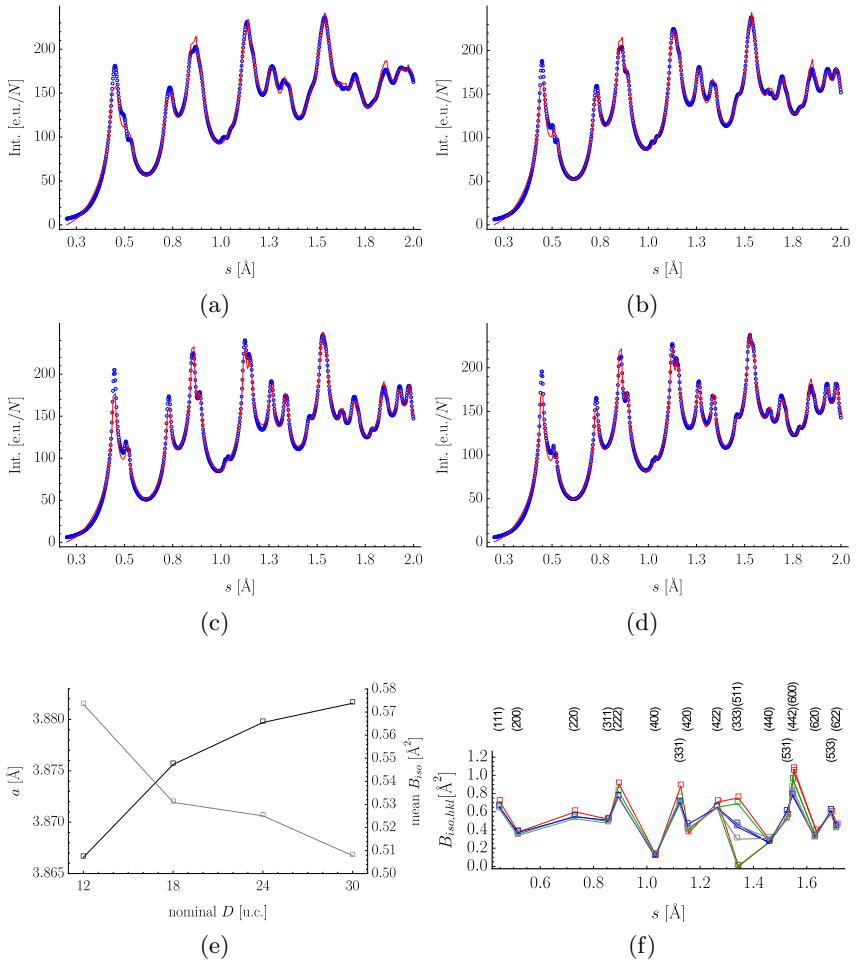


Figure 5.4: Fits of the Pd particles TDS powder profile according to Beyerlein's model, for particles diameter 12 (a), 18 (b), 24 (c) and 30 (d) unit cells. The profile computed from the Molecular Dynamics simulation (see section 4.7) is shown in blue whereas the model fit is shown in red in each case. The trends of the lattice parameter and mean B_{iso} are shown in (e), in black (left ordinate axis) and gray (right ordinate axis), respectively. The hkl -dependent B_{iso} trend is shown in (f) for particles diameter 12 (red), 18 (green), 24 (blue), and 30 (gray) unit cells.

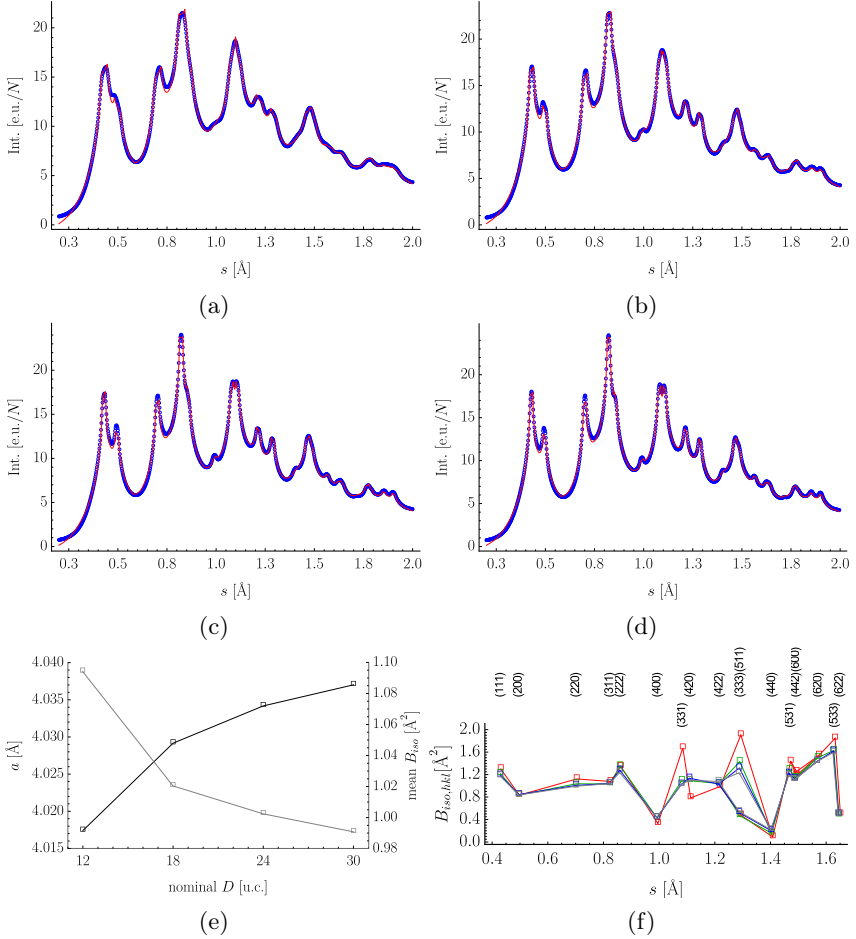


Figure 5.5: Fits of the Al particles TDS powder profile according to Beylerlein's model, for particles diameter 12 (a), 18 (b), 24 (c) and 30 (d) unit cells. The profile computed from the Molecular Dynamics simulation (see section 4.7) is shown in blue whereas the model fit is shown in red in each case. The trends of the lattice parameter and mean B_{iso} are shown in (e), in black (left ordinate axis) and gray (right ordinate axis), respectively. The hkl -dependent B_{iso} trend is shown in (f) for particles diameter 12 (red), 18 (green), 24 (blue), and 30 (gray) unit cells.

Table 5.2: Parameters values from the TDS fits in Figures 5.4 and 5.5. The Debye-Waller parameters are in square Anstrong. For the case of 18 u.c. of diameter the estimated standard deviation of the $B_{iso,hkl}$ is also reported between brackets.

	Pd				Al			
	12 u.c.	18 u.c.	24 u.c.	30 u.c.	12 u.c.	18 u.c.	24 u.c.	30 u.c.
a [Å]	3.867	3.876	3.880	3.882	4.017	4.029	4.034	4.037
D [nm]	1.517	1.476	1.727	1.373	1.343	1.400	1.353	1.287
\bar{B}_{iso}	0.573	0.531	0.523	0.508	1.090	1.020	1.000	0.991
$B_{iso,111}$	0.711	0.663 (0.012)	0.651	0.630	1.302	1.217 (0.073)	1.188	1.174
$B_{iso,200}$	0.378	0.354 (0.017)	0.372	0.337	0.834	0.836 (0.113)	0.845	0.836
$B_{iso,220}$	0.598	0.552 (0.008)	0.544	0.524	1.123	1.036 (0.077)	1.007	0.993
$B_{iso,311}$	0.516	0.492 (0.020)	0.509	0.476	1.077	1.034 (0.177)	1.042	1.038
$B_{iso,222}$	0.904	0.822 (0.077)	0.766	0.754	1.344	1.353 (0.693)	1.279	1.239
$B_{iso,400}$	0.120	0.125 (0.050)	0.106	0.128	0.329	0.429 (0.410)	0.431	0.437
$B_{iso,331}$	0.882	0.750 (0.065)	0.705	0.676	1.674	1.095 (0.760)	1.030	1.022
$B_{iso,420}$	0.367	0.397 (0.047)	0.458	0.411	0.785	1.090 (0.803)	1.136	1.098
$B_{iso,422}$	0.709	0.650 (0.093)	0.646	0.640	0.990	1.042 (1.007)	1.032	1.078
$B_{iso,333}$	0.000	0.000 (0.331)	0.413	0.299	0.478	0.467 (1.032)	0.521	0.541
$B_{iso,511}$	0.751	0.690 (0.348)	0.451	0.457	1.905	1.430 (2.218)	1.317	1.233
$B_{iso,440}$	0.278	0.266 (0.123)	0.261	0.308	0.091	0.157 (0.731)	0.201	0.220
$B_{iso,531}$	0.560	0.526 (0.130)	0.600	0.509	1.436	1.288 (1.801)	1.224	1.187
$B_{iso,442}$	1.042	0.957 (18.27)	0.783	0.864	1.185	1.139 (140.7)	1.118	1.112
$B_{iso,600}$	1.071	0.948 (73.58)	0.781	0.817	1.255	1.144 (557.1)	1.121	1.110
$B_{iso,620}$	0.388	0.333 (0.109)	0.319	0.311	1.543	1.501 (2.403)	1.438	1.430
$B_{iso,533}$	0.590	0.611 (0.452)	0.614	0.590	1.846	1.631 (1.702)	1.617	1.588
$B_{iso,622}$	0.453	0.420 (0.249)	0.435	0.411	0.497	0.479 (0.601)	0.497	0.497

model. Nevertheless, the hkl anisotropy trend kept almost constant among the studied cases of Pd particles, and among the Al particles as well, as can be seen in Figures 5.4f (Pd) and 5.5f (Al). This further indicates

a regularity yet to be explained. To keep the analysis simpler after the previous approximation, g'_{max} was considered equal to the fixed g_{max} .

With the allowance for hkl -dependent Debye-Waller parameters, the model was able to give other fitting parameters values with physical sense, both for Pd and Al particles. The lattice parameter approached the bulk value in each case (3.89 Å for Pd and 4.0495 Å for Al) and the mean Debye-Waller parameter decreased, when increasing particle diameter (see Figures 5.4e and 5.5e). Both effects are related to a lowering of the surface to volume ratio. As discussed in section 4.1, relaxation of the particle driven by atoms sub-coordination leads to a net shrinkage for most metals, lowering the mean lattice parameter. Sub-coordinated atoms also vibrate with larger amplitude [100], and thus the lowering of their fraction decreases the mean Debye-Waller parameter in each study case. For the case of Al particles, on the other hand, this magnitude resulted higher than for Pd particles, which is in correspondence with the different Young modulus of these metals (70 GPa for Al and 121 GPa for Pd). The higher the Young modulus of the material, the smaller the average amplitude of atomic vibrations and therefore the isotropic Debye-Waller parameter [100].

The relative spreading (relative standard deviation, $\sigma_{X,r} = \sigma_X/\bar{X}$) of the anisotropic Debye-Waller factors for the Pd and Al particles around their mean values, also resulted in correspondence with the Zener ratio, A_z , of these two metals [110]. The nearer this magnitude is to 1, the nearer a cubic material is isotropic in its elastic properties, and thus thermal vibrations. Therefore, Al particles should exhibit a proportionally smaller $\sigma_{B_{iso,hkl,r}}$, such that the inverse of its ratio to the same magnitude of Pd particles is similar to $A_z(\text{Pd})/A_z(\text{Al})$. Using the data of the first 4 peaks for the 18 unit cells diameter particles in Table 5.2, it was found that $\sigma_{B_{iso,hkl,r}}(\text{Pd})/\sigma_{B_{iso,hkl,r}}(\text{Al}) = 1.7$, whereas $A_z(\text{Pd})/A_z(\text{Al}) = 2.0$. Other peaks were not considered in this computation since they report less reliable values of $B_{iso,hkl}$, as can be seen from the larger standard deviations in Table 5.2.

The profile of the 200 TDS peak in Figure 5.4 shows a clear splitting

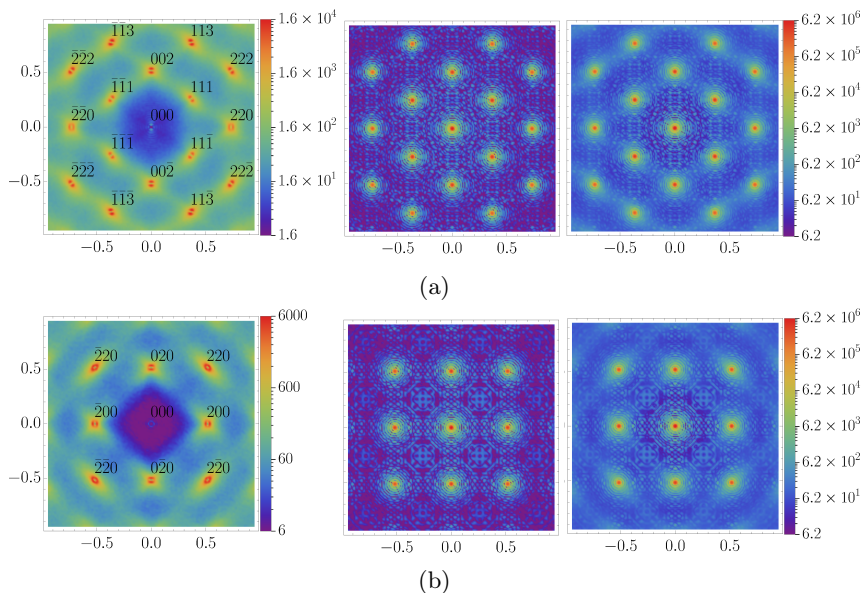


Figure 5.6: Reciprocal space maps of the TDS (left), Bragg (middle) and the total (right) intensity, for the Pd nanoparticle of diameter 12 unit cells. (a) plane $x = y$. (b) plane $z = 0$. The intensity is in electron units and normalized by the number of atoms of the particle in this case (3559). Frame axes are in inverse Anstrong.

of its maxima, as opposed to the other TDS peaks. To further investigate this feature, TDS intensity maps in reciprocal space were constructed for the Pd particles of 12 and 24 unit cells of diameter, for the planes $(1\bar{1}0)$, or $x = y$, and (100) , or $z = 0$. See Figures 5.6 and 5.7. It was found that such feature is due to the interplay between the particular TDS intensity distribution in reciprocal space at each hkl , and the way the (powder) integration s -sphere crosses them. As can be seen in Figures 5.6 and 5.7, both 111 and 200 points have a split TDS intensity distribution, but with different orientations respect to the tangent of the integration sphere. For point 111 the “intensity valley” is crossed transversally by the s -sphere and therefore the decrease of the intensity at the middle is compensated during the integration. For point 200, on the other hand, the intensity

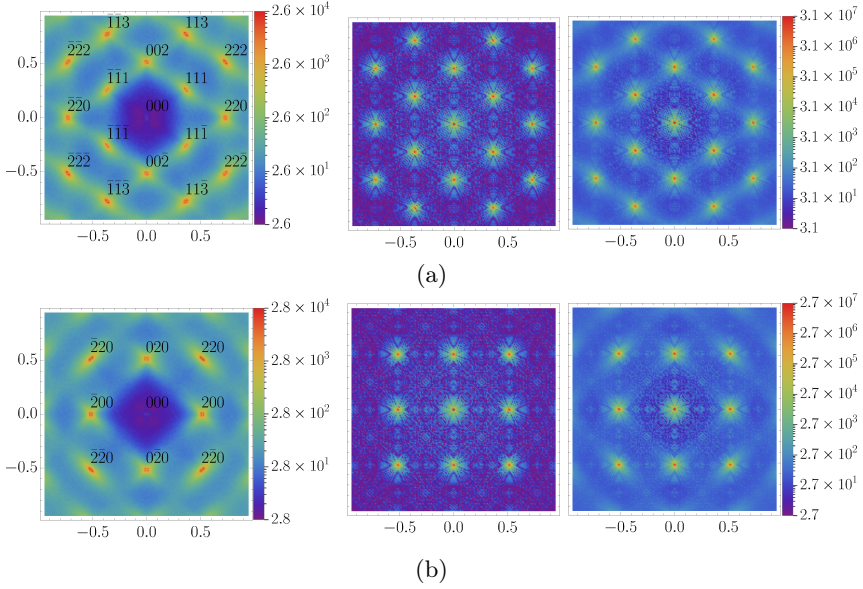


Figure 5.7: Reciprocal space maps of the TDS (left), Bragg (middle) and the total (right) intensity, for the Pd nanoparticle of diameter 24 unit cells. (a) plane $x = y$. (b) plane $z = 0$. The intensity is in electron units and normalized by the number of atoms of the particle in this case (28867). Frame axes are in inverse Anstrong.

valley is crossed longitudinally and therefore no compensation occurs after integration. This results in a bicuspid TDS peak. Such fine features are missed by the simplified analytical model studied here. Nevertheless, the cross sections in Figure 5.6 and 5.7 rather support the idea of vibration mode wavevectors confinement, taken into account by the model through a hollow spherical Brillouin zone at each hkl . These zones are shown to be not spherical in Figures 5.6 and 5.7 and not completely hollow, since the intensity exactly at the hkl positions is not null. Nevertheless, the mentioned Brillouin zone approximation seems still plausible.

In general, more work is necessary to understand the details of the TDS, and the nature of its anisotropic behavior in powder patterns of nanoparticles. As shown above, the use of the Born-von Kármán theory of lattice

dynamics with the sole addition of more suitable VDOS for nanoparticles, leads to a model unable to follow the anisotropic behavior of the TDS at this scale. Allowing for independent Debye-Waller parameters a-posteriori adds enough flexibility to the model to fit the simulated patterns. Such approach, nevertheless, derives from the known elastic properties of bulk crystals which, again, can not be the main or only properties used to study crystals at the nanoscale. It is expected that the validity of the model improves when increasing particle size and the need of anisotropic B_{iso} become less necessary. With larger particles, the BVK theory will be more suitable and expressions will converge to the well established ones in Warren's treatment of the TDS [3].

Chapter 6

Invariant forms of microstrain

Strain has a marked effect on diffraction, which manifests itself in different ways. The most evident is the displacement of Bragg peaks caused by a uniform variation of the interplanar distances through a macroscopic portion of a solid phase component. This effect can be used to measure the macrostrain to a high level of sensitivity, and is the basis of the so-called X-ray residual stress analysis [129, 130]. In addition to macrostrain, inhomogeneous strain is often present in bulk as well as in powder materials, where it is responsible for diffraction peak broadening effects [131, 3]. This microstrain is typical of plastically deformed metals, but is also found in ceramics and in organics, in thin films and coatings [132, 133], and is a key feature of nanocrystals where it results from the different coordination and environment of surface atoms [26, 109, 18].

Strain usually varies along different hkl directions. But since some of them are equivalent because of the point group symmetry of the crystal, also the strain must be the same along them. This led Popa [2] to generalize a result obtained by Stokes & Wilson for the cubic case in a seminal article on the diffraction of X-rays by distorted crystal aggregates [15]. According to Popa's study, the anisotropic effect of microstrain on the diffraction line broadening can be described by invariant forms of Miller indices. These are quartic polynomials, invariant to the symmetry operations of the Laue class of the crystalline phase.

The use of polynomials forms of the Miller indices is common to different models of microstrain, either specific of some defect, like dislocations

[134], surface [18] or compositional effects [135], or just in empirical descriptions of the line broadening effect [2, 136, 97]. Although the general concept of invariant has been described in the cited literature, some confusion in practical implementations arises from errors or missing information in published expressions. In what follows, we provide a complete list of invariant expressions for all Laue classes, also considering different crystallographic settings (e.g., unique axis in the monoclinic class and hexagonal vs rhombohedral cell).

6.1 Microstrain effect on line broadening

Inhomogeneity of atomic displacement in crystalline domains, often named microstrain for brevity, affects the width and shape of the diffraction line profiles. As shown in eqs. 3.51, within the limits of reasonable approximations, the real part of the Fourier Transform (FT) of the diffraction peak profile due to inhomogeneous strain, can be written in terms of the mean square strain $\langle \epsilon_{hkl}^2(L) \rangle = \langle \Delta L_{hkl}^2(L) \rangle / L^2$ as

$$M_{hkl}^D(L) = \text{Exp}[-2\pi^2 s_{hkl}^2 \langle \Delta L_{hkl}^2(L) \rangle] = \text{Exp}[-2\pi^2 s_{hkl}^2 L^2 \langle \epsilon_{hkl}^2(L) \rangle]. \quad (6.1)$$

where L is the distance over which the distortion is examined, projected in the hkl direction inside the domain. If the mean strain $\langle \epsilon_{hkl}(L) \rangle$ is null for any L , as in cold-worked metals [95, 137], the square strain equals the variance of the strain distribution $p_L(\epsilon_{hkl})$ ¹. Popular methods of Line Profile Analysis (PLA) employing Fourier analysis are based on eq. 6.1 for the real component of the FT, while it is assumed that the imaginary component, $N_{hkl}^D(L)$, is null or negligible [95, 137]. This assumption is often acceptable, as in the theory of Krivoglaz-Wilkens on line broadening caused by dislocations in polycrystalline materials [138, 139, 140, 141], but is not generally valid, as seen in Chapter 4 for the case of surface relaxation of nanocrystals [18].

¹For any random variable X with a defined probability density function, it holds that $\text{var}(X) = \langle X^2 \rangle - \langle X \rangle^2$.

Equation 6.1 is strictly correct only if the distribution p_L is Gaussian for every distance L [137, 3]. Even if this hypothesis is difficult to occur exactly in real cases, eq. 6.1 still holds its validity as an approximation independent of the distribution, as far as the values of $\Delta L_{hkl}(L)$ (or $\epsilon_{hkl}(L)$) are small (i.e. p_L being a narrow distribution with mean near zero). Moreover, differently from the early work of Stokes & Wilson [15], the distributions, and thus their moments (mean, mean square, variance ecc.) need not to be constant with L , which adds flexibility and possibility to describe different strain sources. As shown by Wilkens [140], deviations from the hypotheses underlying eq. 6.1 occur for the case of dislocation strain field, but all the same, in simplified form, the expression can be used for the level of approximations in the general theory.

Models implementing eq. 6.1 to describe the diffraction peak profile have shown that the hkl dependence can be singled out in a ‘‘Contrast Factor’’ term, \overline{C}_{hkl} , such that

$$\langle \Delta L_{hkl}^2(L) \rangle = \overline{C}_{hkl} f(L). \quad (6.2)$$

\overline{C}_{hkl} is also called ‘‘anisotropy factor’’, depending on the context. Stokes & Wilson [15] and then Popa [2], for example, proposed expressions equivalent to eq. 6.2 assuming a constant (i.e., independent of L) strain $\langle \epsilon_{hkl}^2 \rangle$, and thus having $f(L) = L^2$. In simplified form [142], also Wilkens model for dislocation strain broadening uses eq. 6.2 with

$$f(L) = (1/\pi)(b/2)^2 \rho L^2 f^*(L/R_e), \quad (6.3)$$

where b is the modulus of the Burgers vector for the given slip system, ρ the average dislocation density and R_e the effective outer cut-off radius. f^* is a known function of L/R_e , the so-called Wilkens function [140]. In this case, given the elastic constants and the slip system, \overline{C}_{hkl} can be calculated for any crystal symmetry [134], so that eq. 6.2 can be used in eq. 6.1 to determine ρ and R_e , and even to guess the (edge/screw) character of the dislocations.

But the validity of eq. 6.2 extends to more general cases, where the

source of strain broadening is different, or not uniquely associated with a dominant defect type. As far as the main source of anisotropy is the elastic medium, eq. 6.2 can be adopted with \overline{C}_{hkl} being the L -independent mean square strain of Popa [2] (an invariant form of the Miller indices), and $f(L)$ given by a polynomial expansion, like $f(L) = aL + bL^2$ in the Popa-Adler-Houska (PAH) model [109, 97]. Coefficients in the invariant and in $f(L)$ can be adjusted to fit the data using the FT of eq. 6.1, a procedure that proved successful in a rather broad variety of experimental cases (e.g., see [143] for recent results).

In all the applications mentioned so far it is fundamental to use the proper invariant form for the corresponding crystal structure, supporting the required choice of axes and crystal system.

6.2 Invariant forms for strain anisotropy

Following Popa [2] the mean square strain of the strain distribution along $[hkl]$ is given by

$$\langle \epsilon_{hkl}^2 \rangle = \frac{\Gamma_{hkl}}{a^4 s_{hkl}^4}, \quad (6.4)$$

with

$$\begin{aligned} \Gamma_{hkl} = & E_{400}h^4 + E_{040}k^4 + E_{004}l^4 + 2(E_{220}h^2k^2 + E_{022}k^2l^2 + E_{202}h^2l^2) \\ & + 4(E_{310}h^3k + E_{301}h^3l + E_{130}hk^3 + E_{031}k^3l + E_{103}hl^3 + E_{013}kl^3) \\ & + 4(E_{211}h^2kl + E_{121}hk^2l + E_{112}hkl^2). \end{aligned} \quad (6.5)$$

The E s in this equation are refinable parameters, whereas a is the first unit cell parameter and s_{hkl} is the modulus of the reciprocal lattice vector corresponding to the hkl reflection. As mentioned before, Popa assumed an L -independent mean square strain, so from eq. 6.2 $f(L) = L^2$, and the contrast factor is equal to the L -independent mean square strain:

$$\overline{C}_{hkl} = \frac{\Gamma_{hkl}}{a^4 s_{hkl}^4}. \quad (6.6)$$

The coefficients in eq. 6.5, the so called “invariant term”, conveniently remind the powers of h, k , and l in the terms they correspond to. The invariant term takes a different form according to the Laue class corresponding to the space group of the crystal under study, and the used setting for the crystal axes. In what follows we show these expressions using the conventional crystal axes and origin for each crystal system, as reported in the International Tables of Crystallography [144], as well as using non-conventional axes. This variety of choices has never been reported in the literature, and some of the expressions given by Popa [2] might generate confusion, for typing errors and missing information regarding the crystallographic setting they refer to. We will use short coefficient names, after some of the coefficients in eq. 6.5 vanish due to the symmetry rules in each case.

6.2.1 Triclinic crystal system (S.G. 1,2)

The two space groups have Laue class $\bar{1}$ and the invariant expression for them is the most general one given by eq. 6.5, since there are no symmetry restrictions:

$$\begin{aligned} \Gamma_{hkl} = & E_1h^4 + E_2k^4 + E_3l^4 + 2(E_4h^2k^2 + E_5k^2l^2 + E_6h^2l^2) \\ & + 4(E_7h^3k + E_8h^3l + E_9hk^3 + E_{10}k^3l + E_{11}hl^3 + E_{12}kl^3) \quad (6.7) \\ & + 4(E_{13}h^2kl + E_{14}hk^2l + E_{15}hkl^2). \end{aligned}$$

6.2.2 Monoclinic crystal system (S.G. 3-15)

All space groups have Laue class $2/m$, with the two fold axis oriented along b or c , depending on the used setting. The invariant expression for the unique axis b setting is:

$$\begin{aligned} \Gamma_{hkl} = & E_1h^4 + E_2k^4 + E_3l^4 + 2(E_4h^2l^2 + E_5k^2l^2 + E_6h^2k^2) \\ & + 4(E_7h^3l + E_8hl^3 + E_9hk^2l), \quad (6.8) \end{aligned}$$

whereas that for the unique axis c setting is:

$$\begin{aligned} \Gamma_{hkl} = & E_1 h^4 + E_2 k^4 + E_3 l^4 + 2 (E_4 h^2 k^2 + E_5 k^2 l^2 + E_6 h^2 l^2) \\ & + 4 (E_7 h^3 k + E_8 h k^3 + E_9 h k l^2). \end{aligned} \quad (6.9)$$

Expression 6.9 is equal to expression (7) of [2], i.e. in that study the author actually refers to the unique axis c setting.

6.2.3 Orthorhombic crystal system (S.G. 16-74)

All space groups have Laue class mmm , in the common standard setting. The invariant form is:

$$\Gamma_{hkl} = E_1 h^4 + E_2 k^4 + E_3 l^4 + 2 (E_4 h^2 k^2 + E_5 k^2 l^2 + E_6 h^2 l^2). \quad (6.10)$$

Equation 6.10 is equal to eq. 8 of [2], where the author labels the Laue class as $2/mmm$.

6.2.4 Tetragonal crystal system (S.G. 75-142)

Space groups 75-88 have Laue class $4/m$, and those No. 89-142 have $4/mmm$. The standard setting is used for all of them. The invariant form for the space groups having Laue class $4/m$ is:

$$\Gamma_{hkl} = E_1 (h^4 + k^4) + E_2 l^4 + 2E_3 h^2 k^2 + 2E_4 l^2 (h^2 + k^2) + 4E_5 h k (h^2 - k^2), \quad (6.11)$$

and for those having Laue class $4/mmm$ it is:

$$\Gamma_{hkl} = E_1 (h^4 + k^4) + E_2 l^4 + 2E_3 h^2 k^2 + 2E_4 l^2 (h^2 + k^2). \quad (6.12)$$

Expressions 6.11 and 6.12 are equal to expressions (9) and (10) of [2] respectively, labeled under the same Laue class symbols.

6.2.5 Trigonal crystal system (S.G. 143-167)

Space groups 143-148 have Laue class $\bar{3}$, and those No. 149-167 have $\bar{3}m$. For all space groups having Laue class $\bar{3}$ the following invariant form is correct when using hexagonal axes $\{\mathbf{a}, \mathbf{b}, \mathbf{c}\}$ in the common standard setting ($\gamma = 120^\circ$):

$$\Gamma_{hkl} = E_1 (h^2 - hk + k^2)^2 + 2E_2 l^2 (h^2 - hk + k^2) + E_3 l^4 + 4E_4 hkl(h - k) + 4E_5 l (h^3 - 3hk^2 + k^3). \quad (6.13)$$

When using the non standard setting with $\gamma = 60^\circ$ (crystal axes changes as $\{\mathbf{a} + \mathbf{b}, \mathbf{b}, \mathbf{c}\}$) the correct form is instead:

$$\Gamma_{hkl} = E_1 (h^2 + hk + k^2)^2 + 2E_2 l^2 (h^2 + hk + k^2) + E_3 l^4 + \frac{4}{3}E_4 l (h^3 + 3h^2k - k^3) + \frac{4}{3}E_5 l (-h^3 + 3hk^2 + k^3). \quad (6.14)$$

If on the other hand rhombohedral axes are used (space groups 146 and 148 only), also in the conventional way, the invariant takes the form:

$$\Gamma_{hkl} = E_1 (h^4 + k^4 + l^4) + 2E_2 (h^2k^2 + k^2l^2 + h^2l^2) + 4E_3 (h^3k + k^3l + hl^3) + 4E_4 (h^3l + hk^3 + kl^3) + 4E_5 hkl(h + k + l). \quad (6.15)$$

Equation 6.14 matches eq. 11 of [2], whereas eq. 6.15 matches equation 12 of [2], labeled under the Laue class symbol $\bar{3}R$, provided variable names are changed as $E3 \rightarrow E4$, $E4 \rightarrow E5$ and $E5 \rightarrow E3$. This choice of coefficient names allows for a better agreement with the general invariant expression in eq. 6.5, where the cubic powers appear before to the terms having h , k and l , one of them squared.

For space groups having Laue class $\bar{3}m$ attention should be paid to the orientation of the two-fold axis (s.g. 149-155) or mirror/glide plane (s.g. 156-167). Space groups 150, 152, 154, 155, 156, 158, 160, 161, 164, 165, 166 and 167 have these symmetry elements in the second position and therefore oriented along $\{100\}$ in the standard hexagonal axes setting

($\gamma = 120^\circ$). For them the invariant takes the form:

$$\Gamma_{hkl} = E_1 (h^2 - hk + k^2)^2 + 2E_2 l^2 (h^2 - hk + k^2) + E_3 l^4 + 4E_4 hkl(h - k). \quad (6.16)$$

If we use the hexagonal setting with $\gamma = 60^\circ$ the expression to be used is instead

$$\Gamma_{hkl} = E_1 (h^2 + hk + k^2)^2 + 2E_2 l^2 (h^2 + hk + k^2) + E_3 l^4 + 4E_4 hkl(h + k). \quad (6.17)$$

Equation 6.17 is equal to eq. 15 in [2], where it was wrongly reported under the Laue class $\bar{3}1m$, i.e., corresponding to space groups 149, 151, 153, 157, 159, 162 and 163, having the twofold rotation axis or mirror/glide plane in the third position.

Space groups 155, 160, 161, 166 and 167 support also a rhombohedral lattice. If the standard rhombohedral setting is used for them, eqs 6.16 and 6.17 are replaced by:

$$\begin{aligned} \Gamma_{hkl} = & E_1 (h^4 + k^4 + l^4) + 2E_2 (h^2 k^2 + k^2 l^2 + h^2 l^2) \\ & + 4E_3 (hk (h^2 + k^2) + kl (k^2 + l^2) + hl (h^2 + l^2)) + 4E_4 hkl(h + k + l). \end{aligned} \quad (6.18)$$

Exchanging E_3 and E_4 in eq. 6.18 (for the same reason as in eq. 6.15) gives correspondence with eq. 14 of [2], labeled under Laue class $\bar{3}m1R$.

Space groups 149, 151, 153, 157, 159, 162 and 163 have the two-fold rotation axis or mirror/glide plane in the third position (oriented along $\{1\bar{1}0\}$) and only allow for a hexagonal cell. With the setting $\gamma = 120^\circ$ the form of the invariant for they is:

$$\begin{aligned} \Gamma_{hkl} = & E_1 (h^2 - hk + k^2)^2 + 2E_2 l^2 (h^2 - hk + k^2) + E_3 l^4 \\ & + E_4 l (4h^3 - 6h^2 k - 6hk^2 + 4k^3), \end{aligned} \quad (6.19)$$

whereas for the setting $\gamma = 60^\circ$ it is

$$\begin{aligned} \Gamma_{hkl} = & E_1 (h^2 + hk + k^2)^2 + 2E_2 l^2 (h^2 + hk + k^2) + E_3 l^4 \\ & + \frac{4}{3} E_4 l (2h^3 + 3h^2 k - 3hk^2 - 2k^3). \end{aligned} \quad (6.20)$$

Equation 6.20 is equal to eq. 13 of [2], although in that study it is wrongly reported under the Laue class symbol $\bar{3}m1$, i.e. corresponding to space groups 150, 152, 154, 155, 156, 158, 160, 161, 164, 165, 166 and 167, having the two fold rotation axis or mirror/glide plane in the second position. Therefore, the present work suggests that eqs. 13 and 15 of [2] should be swapped, and referred to the non-standard hexagonal setting $\{\mathbf{a} + \mathbf{b}, \mathbf{b}, \mathbf{c}\}$ for the crystal axes ($\gamma = 60^\circ$).

6.2.6 Hexagonal crystal system (S.G. 168-194)

Space groups 168-176 have Laue class $6/m$, whereas those No. 177-194 have Laue class $6/mmm$. For all of them the correct invariant expression in the standard hexagonal setting of $\gamma = 120^\circ$ is:

$$\Gamma_{hkl} = E_1 (h^2 - hk + k^2)^2 + 2E_2 l^2 (h^2 - hk + k^2) + E_3 l^4. \quad (6.21)$$

For the setting with $\gamma = 60^\circ$ the correct expression is instead:

$$\Gamma_{hkl} = E_1 (h^2 + hk + k^2)^2 + 2E_2 l^2 (h^2 + hk + k^2) + E_3 l^4. \quad (6.22)$$

Equation 6.22, with the non-standard hexagonal axes, is equal to eq. 16 of [2].

6.2.7 Cubic crystal system (S.G. 195-230)

Space groups 195-206 have Laue class $m\bar{3}$, whereas those No. 207-230 have Laue class $m\bar{3}m$. For all cubic groups, when using the standard setting, the invariant form reads:

$$\Gamma_{hkl} = E_1 (h^4 + k^4 + l^4) + 2E_2 (h^2 k^2 + h^2 l^2 + k^2 l^2), \quad (6.23)$$

which is equal to eq. 17 of [2].

Tables 6.1 and 6.2 summarize the coefficients of all invariant forms mentioned above for the different crystal systems and settings. ‘‘O’’ stands for coefficients missing for symmetry, whereas rules are specified when a

coefficient depends on others. Table 6.3 provides a direct conversion to the alternative E_{hkl} notation. Last, a *TOPAS* macro called `getInvariant` is shown in Figures 6.1 and 6.2, which returns Γ_{hkl} given the space group and the number of independent coefficients E_i [97].

Table 6.1: Coefficients of the invariant form of the Miller indices in eq. 6.5, for the different Laue classes. Independent terms are indicated (X) together with those null for symmetry (0), and those related to others independent coefficients. (Part 1 of 2.)

Laue class	setting	Id	E400	E040	E004	E220	E202	E022	E310
$\bar{1}$	std.	1	X	X	X	X	X	X	X
$2/m$	u.a. b	2	X	X	X	X	X	X	0
	u.a. c	3	X	X	X	X	X	X	X
mmm	std.	4	X	X	X	X	X	X	0
$4/m$	std.	5	X	E400	X	X	X	E202	X
$4/mmm$	std.	6	X	E400	X	X	X	E202	0
$\bar{3}$	hex. std.	7	X	E400	X	3 E400/2	X	E202	-E400/2
	hex. 60°	8	X	E400	X	3 E400/2	X	E202	E400/2
	rhomb.	9	X	E400	E400	X	E220	E220	X
$\bar{3}m1$	hex. std.	10	X	E400	X	3 E400/2	X	E200	-E400/2
	hex. std.	11	X	E400	X	3 E400/2	X	E200	E400/2
$\bar{3}m$	rhomb.	12	X	E400	E400	X	E220	E220	X
	hex. std.	13	X	E400	X	3 E400/2	X	E220	-E400/2
	hex. 60°	14	X	E400	X	3 E400/2	X	E220	E400/2
$6/m, 6/mmm$	hex. std.	15	E400	X	E400	3 E400/2	X	E200	-E400/2
	hex. 60°	16	E400	X	E400	3 E400/2	X	E200	E400/2
$m\bar{3}, m\bar{3}m$	std.	17	X	E400	E400	X	E220	E220	0

Table 6.2: Coefficients of the invariant form of the Miller indices in eq. 6.5, for the different Laue classes (Part 2 of 2). The following auxiliary definitions are used: $A=-E_{211}-3 E_{301}$, $B=(E_{211}-E_{121})/3$, $C=(E_{121}-E_{211})/3$.

Id	E301	E130	E031	E103	E013	E211	E121	E112
1	X	X	X	X	X	X	X	X
2	X	0	0	X	0	0	X	0
3	0	X	0	0	0	0	0	X
4	0	0	0	0	0	0	0	0
5	0	-E310	0	0	0	0	0	0
6	0	0	0	0	0	0	0	0
7	X	-E400/2	E301	0	0	X	A	-E202/2
8	B	E400/2	C	0	0	X	X	E202/2
9	X	E301	E310	E310	E301	X	E211	E211
10	0	-E400/2	0	0	0	X	-E211	-E202/2
11	0	E400/2	0	0	0	X	E211	E202/2
12	E310	E310	E310	E310	E310	X	E211	E211
13	X	-E400/2	E301	0	0	-3 E301/2	-3 E301/2	-E202/2
14	2 E211/3	E400/2	-2 E211/3	0	0	X	-E211	E202/2
15	0	-E400/2	0	0	0	0	0	-E202/2
16	0	E400/2	0	0	0	0	0	E202/2
17	0	0	0	0	0	0	0	0

Table 6.3: Conversion from the E_i to the E_{hkl} coefficient notation, for all Laue classes and different settings listed in Tables 6.1 and 6.2.

Id	Transformation rules
1	E400=E1, E040=E2, E004=E3, E220=E4, E022=E5, E202=E6, E310=E7, E301=E8, E130=E9, E031=E10, E103=E11, E013=E12, E211=E13, E121=E14, E112=E15
2	E040=E2, E004=E3, E202=E4, E400=E1, E022=E5, E220=E6, E301=E7, E103=E8, E121=E9
3	E040=E2, E004=E3, E220=E4, E400=E1, E022=E5, E202=E6, E310=E7, E130=E8, E112=E9
4	E040=E2, E004=E3, E220=E4, E400=E1, E022=E5, E202=E6
5	E004=E2, E220=E3, E202=E4, E400=E1, E310=E5
6	E004=E2, E220=E3, E202=E4, E400=E1
7	E202=E2, E004=E3, E211=E4, E400=E1, E301=E5
8	E202=E2, E004=E3, E211=E4, E400=E1, E121=E5
9	E220=E2, E310=E3, E301=E4, E400=E1, E211=E5
10	E202=E2, E004=E3, E211=E4, E400=E1
11	E202=E2, E004=E3, E211=E4, E400=E1
12	E220=E2, E310=E3, E211=E4, E400=E1
13	E202=E2, E004=E3, E301=E4, E400=E1
14	E202=E2, E004=E3, E211=E4, E400=E1
15	E202=E2, E004=E3, E400=E1
16	E202=E2, E004=E3, E400=E1
17	E220=E2, E400=E1

```

macro getInvariant(sg, E1, E2, E3, E4, E5, E6, E7, E8, E9, E10, E11, E12,
E13, E14, E15) {
  #if Or(sg == 1, sg == 2); 'Triclinic, -1
    E1*H^4+E2*K^4+E3*L^4+2*(E4*H*H*K*K+E5*K*K*L*L+E6*H*H*L*L)+
    4*(E7*(H^3)*K+E8*(H^3)*L+E9*H*(K^3)+E10*(K^3)*L+E11*H*(L^3)+
    E12*K*(L^3) + E13*H*H*K*L + E14*H*K*K*L + E15*H*K*L*L)
  #elseif And(sg >= 3, sg <= 15); 'Monoclinic, 2/m
    If (And(Constant(Get(al))=90,Constant(Get(ga))=90), 'unique axis b
      E1*H^4 + E2*K^4 + E3*L^4 + 2*(E4*H*H*L*L + E5*K*K*L*L+E6*H*H*K*K)+
      4*(E7*(H^3)*L + E8*H*(L^3) + E9*H*K*K*L),
      If(And(Constant(Get(al))=90,Constant(Get(be))=90), 'unique axis c
        E1*H^4 + E2*K^4 + E3*L^4 + 2*(E4*H*H*K*K + E5*K*K*L*L +
        E6*H*H*L*L) + 4*(E7*(H^3)*K + E8*H*(K^3) + E9*H*K*L*L),
        "Invalid Monoclinic lattice parameters"
      )
    )
  #elseif And(sg >= 16, sg <= 74); 'Orthorhombic, mmm
    E1*H^4 + E2*K^4 + E3*L^4 + 2*(E4*H*H*K*K + E5*K*K*L*L + E6*H*H*L*L)
  #elseif And(sg >= 75, sg <= 88); 'Tetragonal, 4/m
    E1*(H^4 + K^4) + E2*L^4 + 2*E3*H*H*K*K + 2*E4*(H*H + K*K)*L*L +
    4*E5*H*K*(H*H - K*K)
  #elseif And(sg >= 89, sg <= 142); 'Tetragonal, 4/mmm
    E1*(H^4 + K^4) + E2*L^4 + 2*E3*H*H*K*K + 2*E4*(H*H + K*K)*L*L
  #elseif And(sg >= 143, sg <= 148); 'Trigonal, -3
    #if Or(sg == 146, sg == 148); 'Trigonal space groups supporting
    'also rhombohedral axes
      If (Constant(Get(ga)) == 120,
        E1*(H*H - H*K + K*K)^2 + 2*E2*(H*H - H*K + K*K)*L*L + E3*L^4
        + 4*E5*(H^3 - 3*H*K*K + (K^3))*L + 4*E4*H*(H - K)*K*L,
        If (Constant(Get(ga)) == 60,
          E1*(H*H + H*K + K*K)^2 + 2*E2*L*L*(H*H + H*K + K*K) +
          E3*L^4 + (4/3)*E4*L*(H^3 + 3*H*H*K - K^3) +
          (4/3)*E5*L*(-H^3 + 3*H*K*K + K^3), ' 60deg
          E1*(H^4 + K^4 + L^4) + 2*E2*(H*H*K*K + H*H*L*L +
          K*K*L*L) + 4*E3*((H^3)*K + (K^3)*L + H*(L^3)) +
          *E4*(H*(K^3) + (H^3)*L + K*(L^3))+ 4*E5*H*K*L*(H + K + L)
        )
      )
    #else
      If (Constant(Get(ga)) == 120,
        E1*(H*H - H*K + K*K)^2 + 2*E2*(H*H - H*K + K*K)*L*L + E3*L^4
        + 4*E5*(H^3 - 3*H*K*K + (K^3))*L + 4*E4*H*(H - K)*K*L,
        E1*(H*H + H*K + K*K)^2 + 2*E2*L*L*(H*H + H*K + K*K) + E3*L^4
        (4/3)*E4*L*(H^3+3*H*H*K-K^3)+(4/3)*E5*L*(-H^3+3*H*K*K+K^3) '60
      )
    #endif

```

Figure 6.1: *TOPAS* macro `getInvariant`, providing Popa's invariant according to the space group. (Part 1 of 2.)

```

#elseif And(sg >= 149, sg <= 167); 'Trigonal, -3m
  #if Or(sg ==150, sg ==152, sg ==154, sg ==155, sg ==156, sg ==158,
  sg ==160,sg ==161,sg==164,sg==165,sg==166,sg==167); 'Trigonal, -3m1
  #if Or(sg==155,sg==160,sg==161,sg==166,sg==167); 'Trigonal
  'space groups supporting also rhombohedral axes
  If (Constant(Get(ga)) == 120,
    E1*(H*H - H*K + K*K)^2 + 2*E2*L*L*(H*H - H*K + K*K) + E3*L^4
    + 4*E4*H*K*L*(H - K),
    If (Constant(Get(ga)) == 60,
      E1*(H*H + H*K + K*K)^2 + 2*E2*L*L*(H*H + H*K + K*K) +
      E3*L^4 + 4*E4*H*K*L*(H + K), ' 60deg
      E1*(H^4 + K^4 + L^4) + 2*E2*(H*H*K*K + H*H*L*L +
      K*K*L*L) + 4*E3*(H*K*(H*H + K*K) + H*L*(H*H + L*L) +
      K*L*(K*K + L*L)) + 4*E4*H*K*L*(H + K + L)
    )
  )
  #else
  If (Constant(Get(ga)) == 120,
    E1*(H*H - H*K + K*K)^2 + 2*E2*L*L*(H*H - H*K + K*K) + E3*L^4
    + 4*E4*H*K*L*(H - K),
    E1*(H*H + H*K + K*K)^2 + 2*E2*L*L*(H*H + H*K + K*K) + E3*L^4
    + 4*E4*H*K*L*(H + K) ' 60deg
  )
  #endif
#else 'Trigonal, -31m
  If (Constant(Get(ga)) == 120,
    E1*(H*H - H*K + K*K)^2 + 2*E2*L*L*(H*H - H*K + K*K) + E3*L^4
    + E4*L*(4*(H^3) - 6*H*H*K - 6*H*K*K + 4*(K^3)),
    E1*(H*H + H*K + K*K)^2 + 2*E2*L*L*(H*H + H*K + K*K) + E3*L^4
    + (4/3)*E4*L*(2*(H^3) + 3*H*H*K - 3*H*K*K - 2*(K^3)) ' 60deg
  )
  #endif
#elseif And(sg >= 168, sg <= 194); 'Hexagonal, 6/m and 6/mmm
  If (Constant(Get(ga)) == 120,
    E1*(H*H - H*K + K*K)^2 + 2*E2*L*L*(H*H - H*K + K*K) + E3*L^4,
    E1*(H*H + H*K + K*K)^2 + 2*E2*L*L*(H*H+H*K+K*K) + E3*L^4 ' 60deg
  )
#elseif And(sg >= 195, sg <= 230); 'Cubic, m-3 and m-3m
  E1*(H^4 + K^4 + L^4) + 2*E2*(H*H*K*K + H*H*L*L + K*K*L*L)
#else
#endif
}

```

Figure 6.2: *TOPAS* macro `getInvariant`, providing Popa's invariant according to the space group. (Part 2 of 2.)

Chapter 7

Conclusions

Diffraction from real materials will always reflect the disorder present in the crystalline structure, both static and dynamic. In this thesis we have shown how these types of disorder have separated effects on powder patterns, which originate from the differences in their intensity distribution in reciprocal space. The work that has been shown leads us to the following conceptual and practical conclusions.

In the description of static and dynamic disorder we have followed two distinct approaches. For the static disorder we opted for the WPPM approach. We saw how it translates any kind of intensity distribution in reciprocal space into mean values of projected length variations, entering directly in the expressions for the powder peak profile. The projected length variations then become the expressions needed by models trying to build peak profiles related to physical phenomena, like the Surface Relaxation treated here. With regard to the dynamic disorder, on the other hand, we worked out the intensity distribution in reciprocal space due to thermal vibrations, adopting physical models at this stage. The models were first the Born-von Kármán theory of lattice dynamics, then the Debye lattice model, and last an extension to account for the peculiarities of thermal vibrations in nanoparticles. We worked out the expression of the intensity distribution in reciprocal space, as far as it was possible to use it to integrate the powder average expression. Both approaches lead to profiles depending on parameters with physical meaning, but the second one has the disadvantage of requiring new analytical work whenever

a different lattice dynamics model is assumed, for instance. It would be very useful to have a TDS powder profile expression depending on one or more magnitudes embodying the peculiarities of thermal vibrations in a particle, regardless the lattice dynamics model used, in the same way the projected length variations embody the lattice distortions in the WPPM (Bragg) profile expressions.

From the practical point of view we would like to first highlight the generality of the methodology followed in Chapter 4 to deduce WPPM peak profiles expressions, for the Surface Relaxation phenomena. That methodology could be used as well for other phenomena causing a lattice distortion, as far as the latter can be characterized by some continuous and smooth displacement field. The quality of the profiles obtained in this way is expected to depend on the quality of the assumed displacement field. The key is choosing a realistic displacement field, but that allow at the same time obtaining compact, and/or easy to implement, expressions of the mean and square mean projected length variation. Unfortunately, this was not the case in this thesis. We obtained very long and complex expressions for the PLVs, even after choosing a very simple displacement field. Future works following this approach could try using more realistic displacement fields, supporting for physical simplifications in the analytical work without affecting too much the final profile. Some displacements fields candidates can be derived from this work though. First, one could solve the elastostatic problem of an elastically anisotropic body subject to hydrostatic pressure, to obtain a somehow physically biased displacement field of a nanoparticle. Special elastic constants would be justified in this case, as it is known that elastic properties change in the nanoscale. Secondly, and possibly the best option due to the lack of a proper theory, one could try to do a parametrization of the atomic displacements, obtained from atomistic simulations. These simulations could be tuned as far as necessary to match real experimental cases. In the first case the fitting parameters would still have a physical meaning, whereas in the second they would just characterize the displacement field inside the particle. These two approaches are expected to have particular influence on the obtained

values for the effective hydrostatic pressure upon a nanoparticle, in a the diffraction pattern modelling. The reason is that, with the deformation field proposed in this work for the Surface Relaxation phenomena, atoms do not interact when displaced from their bulk positions. Therefore, the particle can reach the distorted state needed to fit well a diffraction pattern with a considerably lower external pressure.

Related to the dynamic properties of nanoparticles addressed in Chapter 5, we have illustrated the limitations of current models of Thermal Diffuse Scattering, when used with nanoparticles. In all the studied cases it was necessary to use additional anisotropic factors (Debye-Waller parameters) to make the model fit the simulated TDS pattern. The need of this modification can be due, firstly, to all the simplifications involved in the assumed Debye lattice model. Assuming it, we have completely neglected the dispersion of vibration modes, as well as any kind of anisotropic behavior of them. This could be determined experimentally instead, as well as the vibrational density of states, by means of inelastic scattering of X-ray or neutrons measurements. A better estimate of the distribution of TDS intensity in reciprocal space could be obtained in this way, through the calculation of a more accurate density of phonon wave vectors from the experimental data. In addition, we have neglected anharmonicity in the thermal vibrations. All these are effects clearly present in a real crystal and the extent of their influence in the TDS intensity of nanoparticle needs further studies. We have also actually used the *ideal* TDS as termed in [123], i.e., we have ignored the fact that the real TDS intensity profile is a convolution with the Bragg-only profile. The importance of this convolution operation increases with nanoparticles, as the Bragg profiles become broader and can no longer be approximated by a Dirac delta, when needed in analytical works. Secondly, one could easily explain the differences in the computed and modeled TDS patterns as simply an inadequacy of the Born-von Kármán theory at nano-scale. This theory is based on periodic boundary conditions, which is the same as ignoring the peculiar behavior of surface atoms due to their relative low number. This is not the case any more for nanoparticles. Therefore, a theory giving the vibration modes of

a bounded crystalline structure is needed. One could again substitute the nanoparticle with a spherical elastically anisotropic body, a case already studied in the literature and giving results in good agreement with simulations and experimental measurements [145, 146, 147, 148]. Using the new vibration laws, the TDS intensity expressions for nanoparticles could be found starting back from the general expression of TDS intensity in reciprocal space.

Appendix A

Analytical definitions of the F_i and G_i functions in the expressions of $\langle \Delta L(L) \rangle$ and $\langle \Delta L^2(L) \rangle$ of the surface relaxation model in Chapter 4

We obtained the functions F_i and G_i defined piecewise in a (R, L, r_o) space with $0 \leq L \leq 2R$. The G_i functions are defined in Tables A.1 and A.2. The F_i functions are defined in the Tables A.3, A.4, A.5, A.6 and A.7. For the case of F_{10} we expressed it as $F_{10} = F_{10a} + F_{10b}$ with $F_{10a} = f_{R,r_o}(\varrho)^2 \cos^2 \varphi + f_{R,r_o}(\varrho')^2 \cos^2 \varphi'$ and $F_{10b} = -2f_{R,r_o}(\varrho)f_{R,r_o}(\varrho') \cos \varphi \cos \varphi'$. The functions F_{31} , F_{51} and F_{61} make use of the dilogarithm function $\text{Li}_2(x)$ [149]. The function $\Re[z]$ in F_{51} means the real part of z .

Table A.1: Explicit form of the G_1 , G_2 and G_3 functions of Table 4.1.

function	$L \neq 0$ && $L \neq R$ && $L \neq 2R$	$L = 0$	$L = R$	$L = 2R$	
G_1	L				
G_2		G_{21}	0	$93R/160$	$2R$
G_3		G_{31}	0	$159R/400$	$2R$

Table A.2: Explicit form of the G_4 function of Table 4.1.

function	$0 \leq L < r_o$	$r_o \leq L < 2R - r_o$	$2R - r_o \leq L \leq 2R$
G_4	G_{41}	G_{42}	G_{43}

Table A.3: Explicit form of the F_i functions, $i = 1, 2, \dots, 6$, of Table 4.1. The following auxiliary definitions are used: $y_1(R) = (1680\pi^2 + 8663)R^2/67200$, $y_2(R) = \pi^2 R^2/20 + (480\pi^2 - 5951)R^2/19200$, $y_3(R) = (73920\pi^2 + 302879)R^2/4730880$.

<i>function</i>	$L \neq 0 \ \&\& \ L \neq R \ \&\& \ L \neq 2R$	$L = 0$	$L = R$	$L = 2R$
F_1		L^2		
F_2	F_{21}	0	$93R^2/80$	$8R^2$
F_3	F_{31}	0	$y_1(R)$	$4R^2$
F_4	F_{41}	0	$159R^2/200$	$8R^2$
F_5	F_{51}	0	$y_2(R)$	$8R^2$
F_6	F_{61}	0	$y_3(R)$	$4R^2$

Table A.4: Explicit form of the F_7 , F_8 and F_9 functions of Table 4.1 as well as of F_{10a} . The following auxiliary definitions are used: $w_1(R, r_o) = (10R^2 r_o - 5Rr_o^2 + r_o^3)/(15R^3)$, $\text{booleanExpression} = (r_o \leq L < 2R - r_o \ \&\& \ L \neq R - r_o \ \&\& \ L \neq R)$. (Part 1 of 2.)

<i>function</i>	$0 \leq L < r_o$		$r_o \leq L < 2R - r_o$		
	$L = 0$	$0 < L < r_o$	booleanExpression	$L = R - r_o$	$L = R$
F_7	F_{71}		F_{72}		
F_8	0	F_{81}	F_{821}	F_{822}	F_{823}
F_9	0	F_{91}	F_{921}	F_{922}	F_{923}
F_{10a}	$w_1(R, r_o)$	F_{10a1}	F_{10a2}		

Table A.5: Explicit form of the F_7 , F_8 and F_9 functions of Table 4.1 as well as of F_{10a} . (Part 2 of 2.)

<i>function</i>	$2R - r_o \leq L \leq 2R$	
	$2R - r_o \leq L < 2R$	$L = 2R$
F_7	F_{73}	
F_8	F_{83}	$8R$
F_9	F_{93}	$8R$
F_{10a}	F_{10a3}	2

Table A.6: Explicit form of the F_{10b} function. (Part 1 of 2.)

<i>function</i>	$0 \leq L < r_o$	$r_o \leq L < 2(R - r_o)$
F_{10b}	F_{10b1}	F_{10b2}

Table A.7: Explicit form of the F_{10b} function. (Part 2 of 2.)

function	$2(R - r_o) \leq L < 2R - r_o$	$2R - r_o \leq L \leq 2R$
F_{10b}	F_{10b3}	F_{10b4}

The F s and G s function of the previous tables are defined as follow:

$$G_{21} = \frac{3(L^2 - R^2)^4 \log\left(\left|1 - \frac{L}{R}\right|\right)}{4L^4(L - 2R)^2(L + 4R)} + \frac{7L^7 + 24L^6R - 268L^5R^2 + 424L^4R^3 - 42L^3R^4 - 88L^2R^5 + 12LR^6 + 24R^7}{32L^3(L - 2R)^2(L + 4R)} \quad (\text{A.1})$$

$$G_{31} = \frac{3(L^2 - R^2)^5 \log\left(\left|1 - \frac{L}{R}\right|\right)}{4L^6(L - 2R)^2(L + 4R)} + \frac{1}{160L^5R^2(L - 2R)(L + 4R)}(10L^{10} + 20L^9R - 33L^8R^2 + 54L^7R^3 - 787L^6R^4 + 426L^5R^5 + 382L^4R^6 - 260L^3R^7 - 250L^2R^8 + 60LR^9 + 60R^{10}) \quad (\text{A.2})$$

$$G_{41} = \frac{L(5L^3 + 16L^2(R - r_o) - 30LR(R + r_o) + 80R^2r_o)}{5r_o(L - 2R)^2(L + 4R)} \quad (\text{A.3})$$

$$G_{42} = -\frac{r_o(15L^4 - 5L^2(12R^2 - 4Rr_o + r_o^2) + r_o^2(10R^2 - 6Rr_o + r_o^2))}{5L^2(L - 2R)^2(L + 4R)} \quad (\text{A.4})$$

$$G_{43} = \frac{5L^4 + 4L^3(R + 4r_o) + 34L^2R(r_o - R) + 8LR^2(R - r_o) + 8R^3(R - r_o)}{5L^2r_o(L + 4R)} \quad (\text{A.5})$$

$$F_{21} = \frac{3(L^2 - R^2)^4 \log\left(\left|1 - \frac{L}{R}\right|\right)}{2L^3(L - 2R)^2(L + 4R)} + \frac{7L^6 + 38L^5R - 192L^4R^2 + 40L^3R^3 + 38L^2R^4 - 12LR^5 - 12R^6}{16L^2(L - 2R)(L + 4R)} \quad (\text{A.6})$$

$$F_{31} = -\frac{3L^5 \left(\log\left(\frac{R}{L}\right) \log(|R - L|) + \text{Li}_2\left(1 - \frac{R}{L}\right)\right)}{2(L - 2R)^2(L + 4R)} + \frac{(R^2 - L^2)(5L^{10} + 41L^8R^2 - 67L^6R^4 + 53L^4R^6 - 28L^2R^8 + 8R^{10}) \log\left(\left|1 - \frac{L}{R}\right|\right)}{16L^7(L - 2R)^2(L + 4R)} + \frac{3L^5(\log^2(L) - \log^2(R))}{4(L - 2R)^2(L + 4R)} + \frac{1}{13440L^6R^2(L - 2R)^2(L + 4R)}(360L^{13} + 21(829 + 80\pi^2)L^{11}R^2 - 24360L^{10}R^3 - 100632L^9R^4 + 181160L^8R^5 - 37590L^7R^6 + R^6 - 83208L^6R^7 + 27580L^5R^8 + 59304L^4R^9 - 13440L^3R^{10} - 28000L^2R^{11} + 3360LR^{12} + 6720R^{13}) \quad (\text{A.7})$$

$$F_{41} = \frac{3(L^2 - R^2)^5 \log\left(\left|1 - \frac{L}{R}\right|\right)}{2L^5(L-2R)^2(L+4R)} + \quad (\text{A.8})$$

$$+ \frac{1}{80L^4R^2(L-2R)(L+4R)} (10L^{10} + 20L^9R - 33L^8R^2 + 54L^7R^3 - 787L^6R^4 +$$

$$+ 426L^5R^5 + 382L^4R^6 - 260L^3R^7 - 250L^2R^8 + 60LR^9 + 60R^{10})$$

$$F_{51} = \frac{1}{16L^9R^2(L-2R)^2(L+4R)} ((L^2 - R^2)(3L^{14} - 2L^{12}R^2 - 92L^{10}R^4 + 196L^8R^6 -$$

(A.9)

$$- 224L^6R^8 + 169L^4R^{10} - 77L^2R^{12} + 15R^{14}) \log\left(\left|1 - \frac{L}{R}\right|\right) +$$

$$+ \frac{3L^5 (\Re [\text{Li}_2(\frac{R}{L})] + \frac{1}{2}(\log(\frac{R}{L}))^2)}{2(L-2R)^2(L+4R)} + \frac{1}{26880L^8R^4(L-2R)^2(L+4R)} (140L^{17} -$$

$$- 3039L^{15}R^2 + 5040L^{14}R^3 + 6(6103 - 560\pi^2)L^{13}R^4 - 47040L^{12}R^5 - 303576L^{11}R^6 +$$

$$+ 702688L^{10}R^7 - 239820L^9R^8 - 548896L^8R^9 + 249410L^7R^{10} + 549792L^6R^{11} -$$

$$- 172200L^5R^{12} - 366800L^4R^{13} + 70980L^3R^{14} + 146160L^2R^{15} - 12600LR^{16} -$$

$$- 25200R^{17})$$

$$F_{61} = \frac{15L^5 (2 \log(\frac{L}{R}) \log(|R-L|) - 2\text{Li}_2(1 - \frac{R}{L}) - \log^2(L) + \log^2(R))}{32(L-2R)^2(L+4R)} + \quad (\text{A.10})$$

$$+ \frac{5(R^2 - L^2) \log\left(\left|1 - \frac{L}{R}\right|\right)}{256L^{11}(L-2R)^2(L+4R)} (7L^{14} + 151L^{12}R^2 - 401L^{10}R^4 + 607L^8R^6 - 617L^6R^8 +$$

$$+ 391L^4R^{10} - 129L^2R^{12} + 15R^{14}) + \frac{1}{946176L^{10}R^6(L-2R)^2(L+4R)} (336L^{21} +$$

$$+ 12936L^{19}R^2 - 71632L^{17}R^4 + 33(21181 + 2240\pi^2)L^{15}R^6 - 1016400L^{14}R^7 -$$

$$- 4384776L^{13}R^8 + 12336016L^{12}R^9 - 5805492L^{11}R^{10} - 13711248L^{10}R^{11} +$$

$$+ 7949480L^9R^{12} + 17982800L^8R^{13} - 7320390L^7R^{14} - 15917264L^6R^{15} +$$

$$+ 4185720L^5R^{16} + 8778000L^4R^{17} - 1261260L^3R^{18} - 2568720L^2R^{19} +$$

$$+ 138600LR^{20} + 277200R^{21})$$

$$F_{71} = \frac{2L^2 (5L^3 + 16L^2(R - r_o) - 30LR(R + r_o) + 80R^2 r_o)}{5r_o(L - 2R)^2(L + 4R)} \quad (\text{A.11})$$

$$F_{72} = -\frac{2r_o (15L^4 - 5L^2 (12R^2 - 4Rr_o + r_o^2) + r_o^2 (10R^2 - 6Rr_o + r_o^2))}{5L(L - 2R)^2(L + 4R)} \quad (\text{A.12})$$

$$F_{73} = \frac{2 (5L^4 + 4L^3(R + 4r_o) + (8R^3 - 34L^2R + 8LR^2) (R - r_o))}{5Lr_o(L + 4R)} \quad (\text{A.13})$$

$$\begin{aligned} F_{81} = & -\frac{L^4 \left(189L \log \left(\frac{R-L-r_o}{R+L-r_o} \right) - 640(R - r_o) \log ((R - r_o)^2 - L^2) \right)}{210r_o(L - 2R)^2(L + 4R)} - \quad (\text{A.14}) \\ & -\frac{(R - r_o)^2 (-630L^8 + 210L^6(R - r_o)^2 - 45L^2(R - r_o)^6 + 14(R - r_o)^8) \tanh^{-1} \left(\frac{L}{R-r_o} \right)}{105L^5r_o(L - 2R)^2(L + 4R)} + \\ & +\frac{1}{42L^5r_o(L - 2R)^2(L + 4R)} (128L^9(r_o - R) \log(R(R - L)) + (63L^{10} - \\ & - 252L^8Rr_o + 42L^6R^3(5R + 4r_o) - 252L^4R^6 + 9L^2R^7(15R - 8r_o) + \\ & + 28R^9(r_o - R)) \log \left(1 - \frac{L}{R} \right)) - \\ & -\frac{1}{529200L^4Rr_o(L - 2R)^2(L + 4R)} (6615L^9(13R - 48r_o) - 40L^8R(18047R + 1798r_o) + \\ & + 6300L^7R^2(886R + 521r_o) - 2520L^6R(1151R^3 + 5906R^2r_o - 2238Rr_o^2 + 746r_o^3) + \\ & + 1050L^5R^4(1163R + 160r_o) + 504L^4R(5437R^5 - 150R^4r_o + 1220R^3r_o^2 - 1220R^2r_o^3 + \\ & + 610Rr_o^4 - 122r_o^5) - 6300L^3R^6(121R - 58r_o) - 840L^2R(1643R^7 + 754R^6r_o - \\ & - 5082R^5r_o^2 + 8470R^4r_o^3 - 8470R^3r_o^4 + 5082R^2r_o^5 - 1694Rr_o^6 + 242r_o^7) + \\ & + 176400LR^8(R - r_o) + 70560R(4R^9 + 4R^8r_o - 36R^7r_o^2 + 84R^6r_o^3 - 126R^5r_o^4 + \\ & + 126R^4r_o^5 - 84R^3r_o^6 + 36R^2r_o^7 - 9Rr_o^8 + r_o^9)) \end{aligned}$$

$$\begin{aligned}
F_{821} = & \frac{(126L^6 + 693RL^5 + 935R^2L^4 + 265R^3L^3 - 465R^4L^2 - 434R^5L - 112R^6)(L - R)^4}{210L^5(L - 2R)^2R(L + 4R)} \\
& \tag{A.15} \\
& - \frac{r_o}{529200L^5(L - 2R)^2(L + 4R)} \left(279090L^8 + 939960(3R - r_o)L^7 - \right. \\
& - 210 \left(48498R^2 - 17212r_oR + 4303r_o^2 \right) L^6 + 30744 \left(10R^3 - 10r_oR^2 + 5r_o^2R - r_o^3 \right) L^5 + \\
& + 2520 \left(915R^4 + 40r_oR^3 + 600r_o^2R^2 - 366r_o^3R + 61r_o^4 \right) L^4 + \\
& + 101640 \left(21R^5 - 35r_oR^4 + 35r_o^2R^3 - 21r_o^3R^2 + 7r_o^4R - r_o^5 \right) L^3 - \\
& - 45(47516R^6 - 71512r_oR^5 + 148190r_o^2R^4 - 139720r_o^3R^3 + 74564r_o^4R^2 - 21976r_o^5R + \\
& + 2747r_o^6)L^2 - \\
& - 35280 \left(36R^7 - 84r_oR^6 + 126r_o^2R^5 - 126r_o^3R^4 + 84r_o^4R^3 - 36r_o^5R^2 + 9r_o^6R - r_o^7 \right) L + \\
& + 14(35280R^8 - 94080r_oR^7 + 259140r_o^2R^6 - 405468r_o^3R^5 + 451290r_o^4R^4 - 328080r_o^5R^3 + \\
& + 143280r_o^6R^2 - 34090r_o^7R + 3409r_o^8) + \\
& + \frac{1}{529200L^5(L - 2R)^2(L + 4R)r_o} \left(- 317520 \log(R - r_o) \left(R^2 - L^2 \right)^5 - \right. \\
& - 2520 \log(R) \left(126L^{10} - 630 \left(R^2 + r_o^2 \right) L^8 + 210 \left(6R^4 + 6r_o^2R^2 - 4r_o^3R + r_o^4 \right) L^6 - 1260R^6L^4 + \right. \\
& + 45 \left(14R^8 - 28r_o^2R^6 + 56r_o^3R^5 - 70r_o^4R^4 + 56r_o^5R^3 - 28r_o^6R^2 + 8r_o^7R - r_o^8 \right) L^2 - \\
& - 14(9R^{10} - 45r_o^2R^8 + 120r_o^3R^7 - 210r_o^4R^6 + 252r_o^5R^5 - 210r_o^6R^4 + 120r_o^7R^3 - 45r_o^8R^2 + \\
& + 10r_o^9R - r_o^{10}) + \\
& + 2520 \log(|R - L|) \left(189L^{10} - 640(R - r_o)L^9 + 630R(R - 2r_o)L^8 - 210R^3(R - 4r_o)L^6 + \right. \\
& + 45R^7(R - 8r_o)L^2 - 14R^9(R - 10r_o) \left. \right) - \\
& - 2520 \log(|L - R + r_o|) \left(189L^5 + 305(R - r_o)L^4 + 265(R - r_o)^2L^3 + 165(R - r_o)^3L^2 + \right. \\
& + 70(R - r_o)^4L + 14(R - r_o)^5 \left. \right) (L - R + r_o)^5 \left. \right)
\end{aligned}$$

$$\begin{aligned}
F_{822} = & \frac{r_o}{529200R(R-r_o)^5(5R-r_o)(R+r_o)^2} \left(5252310R^9 - 31293360R^8r_o + \right. & (A.16) \\
& + 80429580R^7r_o^2 - 104633424R^6r_o^3 + 50079960R^5r_o^4 + 25896960R^4r_o^5 - \\
& - 42815655R^3r_o^6 + 20196170R^2r_o^7 - 4141835Rr_o^8 + 317520r_o^9 + \\
& + 2520Rr_o^3 \left(5r_o \log(R)(r_o - R)(-336R^3 + 576R^2r_o - 333Rr_o^2 + 65r_o^3) + \right. \\
& + \log(r_o)(4032R^5 - 11760R^4r_o + 14640R^3r_o^2 - 9585R^2r_o^3 + 3250Rr_o^4 - 451r_o^5) - \\
& \left. \left. - 126 \log(R - r_o)(2R - r_o)^5 \right) \right)
\end{aligned}$$

$$\begin{aligned}
F_{823} = & \frac{r_o}{2646000R^8} (5252310R^8 - 3774960R^7r_o + 3166380R^6r_o^2 - 1968624R^5r_o^3 - & (A.17) \\
& - 864360R^4r_o^4 + 2435760R^3r_o^5 - 1564785R^2r_o^6 + 441980Rr_o^7 - 47726r_o^8) \\
& + 2520 \log\left(\frac{R}{r_o}\right) r_o^3 (1008R^5 - 1680R^4r_o + 1320R^3r_o^2 - 585R^2r_o^3 + 140Rr_o^4 - 14r_o^5)
\end{aligned}$$

$$\begin{aligned}
F_{83} = & \frac{\log\left(\frac{L}{R} - 1\right)}{42L^5r_o(L-2R)^2(L+4R)} (63L^{10} + 4(32L^9 + 7R^9)(r_o - R) - 252L^8Rr_o + & (A.18) \\
& + 42L^6R^3(5R + 4r_o) - 252L^4R^6 + 9L^2R^7(15R - 8r_o)) + \\
& + \frac{2R - L}{105840L^5Rr_o(L-2R)^2(L+4R)} (1323L^9(13R - 48r_o) + 2L^8R(25883R - 151568r_o) \\
& + 4L^7R^2(304973R + 12547r_o) + 8L^6R^3(362071r_o - 395146R) + \\
& + 2L^5R^4(347827R - 473512r_o) + 20L^4R^5(96353R - 92384r_o) + \\
& + 4L^3R^6(110494r_o - 90649R) - 1041872L^2R^7(R - r_o) + \\
& + 108080LR^8(R - r_o) + 286720R^9(R - r_o))
\end{aligned}$$

$$\begin{aligned}
F_{91} = & \frac{640L^4(R-r_o)}{231r_o(L-2R)^2(L+4R)} \log\left(\frac{(R-r_o)^2-L^2}{R^2}\right) - & (A.19) \\
& - \frac{1}{924L^7r_o(L-2R)^2(L+4R)} \log\left(\frac{R-L-r_o}{R+L+r_o}\right) (693L^{12} + 2772L^{10}(R-r_o)^2 - \\
& - 1155L^8(R-r_o)^4 + 495L^4(R-r_o)^8 - 308L^2(R-r_o)^{10} + 63(R-r_o)^{12}) + \\
& + \frac{1}{462L^7r_o(L-2R)^2(L+4R)} \log\left(1 - \frac{L}{R}\right) (693L^{12} - 1280L^{11}(R-r_o) - \\
& - 693L^{10}R(R+4r_o) + 2310L^8R^3(2R+r_o) - 6930L^6R^6 + 495L^4R^7(11R-4r_o) - \\
& - 77L^2R^9(29R-20r_o) + 378R^{11}(R-r_o)) + \\
& + \frac{1}{166486320L^6R^3r_o(L-2R)^2(L+4R)} (2972970L^{13}(5R+2r_o) + \\
& + 194040R(R-r_o)(256L^{12} + 351LR^{11} + 117R^2(5R^{10} + 10R^9r_o - 45R^8r_o^2 + \\
& + 120R^7r_o^3 - 210R^6r_o^4 + 252R^5r_o^5 - 210R^4r_o^6 + 120R^3r_o^7 - 45R^2r_o^8 + 10Rr_o^9 - r_o^{10})) - \\
& - 2081079L^{11}R^2(53R+20r_o) - 520L^{10}R^3(84160R - 564409r_o) - 9009L^9R^4(149837R + 56908r_o) \\
& + 360360L^8R^3(4215R^3 + 10781R^2r_o - 5169Rr_o^2 + 1723r_o^3) - 30030L^7R^6(29144R + 3427r_o) \\
& - 144144L^6R^3(14050R^5 - 390R^4r_o + 2810(R^3r_o^2 - R^2r_o^3) + 1405Rr_o^4 - 281r_o^5) + \\
& + 90090L^5R^8(8909R - 2672r_o) + 48048L^4R^3(32785R^7 + 9692R^6r_o - \\
& - 63777R^5r_o^2 + 106295R^4r_o^3 - 106295R^3r_o^4 + 63777R^2r_o^5 - 21259Rr_o^6 + 3037r_o^7) \\
& - 1261260L^3R^{10}(292R - 193r_o) - 2522520L^2R^3(260R^9 + 167R^8r_o - 1476R^7r_o^2 + \\
& + 3444R^6r_o^3 - 5166R^5r_o^4 + 5166R^4r_o^5 - 3444R^3r_o^6 + 1476R^2r_o^7 - 369Rr_o^8 + 41r_o^9))
\end{aligned}$$

$$\begin{aligned}
& \frac{1}{332972640L^7(L-2R)^2R^3(L+4R)(R-r_o)^2} \left(-5945940(3R-2r_o)r_oL^{14} + \right. \\
& + 41621580R \left(6R^3 - 12r_oR^2 + 10r_o^2R - 3r_o^3 \right) L^{12} + 249729480R^3(R-r_o)^2L^{11} - \\
& - 36036R(60250R^5 - 131778r_oR^4 + 105906r_o^2R^3 - 42463r_o^3R^2 + 13860r_o^4R - 2310r_o^5)L^{10} + \\
& + 360360R^3(R-r_o)^2(905R^2 - 5169r_oR + 1723r_o^2)L^9 + \\
& + 15015R(271200R^7 - 171426r_oR^6 - 496304r_o^2R^5 + 483915r_o^3R^4 - 49422r_o^4R^3 - 43507r_o^5R^2 + \\
& + 22176r_o^6R - 2772r_o^7)L^8 - 144144R^3(R-r_o)^2(625R^4 + 2810r_oR^3 - 2810r_o^2R^2 + \\
& + 1405r_o^3R - 281r_o^4)L^7 - 180180R^3(28220R^7 - 37150r_oR^6 - 8360r_o^2R^5 + 27650r_o^3R^4 - \\
& - 19348r_o^4R^3 + 14294r_o^5R^2 - 4744r_o^6R + 593r_o^7)L^6 - 48048R^3(R-r_o)^2(1875R^6 + 63777r_oR^5 - \\
& - 106295r_o^2R^4 + 106295r_o^3R^3 - 63777r_o^4R^2 + 21259r_o^5R - 3037r_o^6)L^5 + \\
& + 12870R(284060R^{11} - 210252r_oR^{10} - 888692r_o^2R^9 + 2231250r_o^3R^8 - 3220812r_o^4R^7 + \\
& + 3279066r_o^5R^6 - 2254440r_o^6R^5 + 1078263r_o^7R^4 - 360350r_o^8R^3 + 83467r_o^9R^2 - 12936r_o^{10}R + \\
& + 1078r_o^{11})L^4 + 2522520R^3(R-r_o)^2(35R^8 + 1476r_oR^7 - 3444r_o^2R^6 + 5166r_o^3R^5 - 5166r_o^4R^4 + \\
& + 3444r_o^5R^3 - 1476r_o^6R^2 + 369r_o^7R - 41r_o^8)L^3 - \\
& - 10010R(140868R^{13} - 50526r_oR^{12} - 854952r_o^2R^{11} + 2688840r_o^3R^{10} - 5374908r_o^4R^9 + \\
& + 7742658r_o^5R^8 - 8096616r_o^6R^7 + 6207399r_o^7R^6 - 3455342r_o^8R^5 + 1380291r_o^9R^4 - \\
& - 392280r_o^{10}R^3 + 78554r_o^{11}R^2 - 10584r_o^{12}R + 756r_o^{13})L^2 - 22702680R^3(R-r_o)^2(R^{10} + \\
& + 55r_oR^9 - 165r_o^2R^8 + 330r_o^3R^7 - 462r_o^4R^6 + 462r_o^5R^5 - 330r_o^6R^4 + 165r_o^7R^3 - 55r_o^8R^2 + \\
& + 11r_o^9R - r_o^{10})L + 63R(3603600R^{15} - 1081080r_oR^{14} - 29069040r_o^2R^{13} + 116696580r_o^3R^{12} - \\
& - 304744440r_o^4R^{11} + 577621044r_o^5R^{10} - 814619520r_o^6R^9 + 867443148r_o^7R^8 - 698504092r_o^8R^7 + \\
& + 424233810r_o^9R^6 - 193197732r_o^{10}R^5 + 65388505r_o^{11}R^4 - 16253034r_o^{12}R^3 + 2903331r_o^{13}R^2 - \\
& - 348480r_o^{14}R + 21780r_o^{15}) - \\
& - \frac{\log \left(\left| \frac{L-R}{L-R+r_o} \right| \right)}{462L^7(L-2R)^2(L+4R)r_o} (1280(R-r_o)L^{11} - 693R(5R-4r_o)L^{10} + \\
& + 1155R^3(5R-2r_o)L^8 - 6930R^6L^6 + 990R^7(5R+2r_o)L^4 - 385R^9(5R+4r_o)L^2 + \\
& + 63R^{11}(5R+6r_o)) - \\
& - \frac{r_o}{924L^7(L-2R)^2(L+4R)} \log \left(\left| \frac{L-R+r_o}{R} \right| \right) (63r_o^{10} - 756Rr_o^9 + \\
& + 154(27R^2 - 2L^2)r_o^8 + 1540R(2L^2 - 9R^2)r_o^7 + 495(L^4 - 28R^2L^2 + 63R^4)r_o^6 - \\
& - 264R(15L^4 - 140R^2L^2 + 189R^4)r_o^5 + 924R^2(15L^4 - 70R^2L^2 + 63R^4)r_o^4 - \\
& - 5544R^3(5L^4 - 14R^2L^2 + 9R^4)r_o^3 - 1155(L^8 - 30R^4L^4 + 56R^6L^2 - 27R^8)r_o^2 + \\
& + 4620R(L^2 - R^2)^3(L^2 + 3R^2)r_o + 1386(L^2 - R^2)^4(2L^2 + 3R^2)) + \\
& + \frac{3 \log \left(\left| \frac{(L-R)(R-r_o)}{R(L-R+r_o)} \right| \right) (L^2 - R^2)^6}{4L^7(L-2R)^2(L+4R)r_o}
\end{aligned}$$

$$\begin{aligned}
F_{922} = & \frac{r_o^5}{924(R-r_o)^7(5R-r_o)(R+r_o)^2} \left(-2 \log(R)(R-r_o)(3696R^5 - 2640R^4r_o - \right. \\
& - 5610R^3r_o^2 + 8030R^2r_o^3 - 3685Rr_o^4 + 587r_o^5) + \\
& + \log(r_o)(-36960R^6 + 120384R^5r_o - 172260R^4r_o^2 + 138160R^3r_o^3 - 65010R^2r_o^4 + \\
& + 16860Rr_o^5 - 1867r_o^6) + 693(r_o - 2R)^6 \log(R - r_o) + \\
& + \frac{r_o}{332972640R^3(R-r_o)^9(5R-r_o)(R+r_o)^2} (2302862562R^{15} - 22992553584R^{14}r_o + \\
& + 104337670437R^{13}r_o^2 - 288721963530R^{12}r_o^3 + 534351024207R^{11}r_o^4 - 654395999400R^{10}r_o^5 + \\
& + 469186792074R^9r_o^6 - 80707502876R^8r_o^7 - 201739357820R^7r_o^8 + 237128673964R^6r_o^9 - \\
& - 140614480552R^5r_o^{10} + 53642464652R^4r_o^{11} - 13981370134R^3r_o^{12} + 2457682920R^2r_o^{13} - \\
& - 259888860Rr_o^{14} + 11891880r_o^{15})
\end{aligned} \tag{A.21}$$

$$\begin{aligned}
F_{923} = & \frac{r_o}{1664863200R^{12}} (2302862562R^{12} - 2071169100R^{11}r_o + 1385899515R^{10}r_o^2 + \\
& + 1534052520R^9r_o^3 - 4092788700R^8r_o^4 + 2301361920R^7r_o^5 + 1470346020R^6r_o^6 - \\
& - 2726103380R^5r_o^7 + 1706374670R^4r_o^8 - 604982196R^3r_o^9 + 135550233R^2r_o^{10} - \\
& - 19209960Rr_o^{11} + 1372140r_o^{12} + 360360R^2r_o^4 \log\left(\frac{R}{r_o}\right) (7392R^6 - 16896R^5r_o + \\
& + 17820R^4r_o^2 - 10780R^3r_o^3 + 3850R^2r_o^4 - 756Rr_o^5 + 63r_o^6))
\end{aligned} \tag{A.22}$$

$$\begin{aligned}
F_{93} = & \frac{\log\left(\frac{L}{R} - 1\right)}{462L^7r_o(L-2R)^2(L+4R)} (693L^{12} - 1280L^{11}(R-r_o) - 693L^{10}R(R+4r_o) + \\
& + 2310L^8R^3(2R+r_o) - 6930L^6R^6 + 495L^4R^7(11R-4r_o) + 77L^2R^9(20r_o-29R) + \\
& + 378R^{11}(R-r_o) + \\
& + \frac{1}{166486320L^7R^3r_o(L-2R)(L+4R)} (2972970L^{13}(5R+2r_o) - \\
& - 13860L^{12}R(1439R-4442r_o) + 693L^{11}R^2(117620r_o-216719R) + \\
& + 2L^{10}R^3(59629060r_o-3439927R) - L^9R^4(1363641241R+274167932r_o) + \\
& + 2L^8R^5(2496895439R-2053625612r_o) + 2L^7R^6(1168854611r_o-771368522R) + \\
& + 4L^6R^7(1132278071r_o-1267548206R) + 2L^5R^8(658675321R-918810196r_o) + \\
& + 20L^4R^9(217793837R-211550600r_o) + 140L^3R^{10}(5495681r_o-4603790R) - \\
& - 2048339720L^2R^{11}(R-r_o) + 112525560LR^{12}(R-r_o) + 361267200R^{13}(R-r_o))
\end{aligned} \tag{A.23}$$

$$\begin{aligned}
F_{10a1} = & \frac{2(L^2 - R^2)^3 (R - r_o)^2 \log\left(1 - \frac{L}{R}\right)}{L^3 r_o^2 (L - 2R)^2 (L + 4R)} + \\
& + \frac{1}{420L^2 r_o^2 (L - 2R)^2 (L + 4R)} (231L^7 + 1248L^6 (R - r_o) - 210L^5 (3R + r_o)^2 + \\
& + 168L^4 R (-11R^2 + 46Rr_o + 5r_o^2) + 210L^3 R^2 (5R^2 - 10Rr_o - 19r_o^2) + \\
& + 448L^2 (5R^5 - 10R^4 r_o + 5R^3 r_o^2 + 10R^2 r_o^3 - 5Rr_o^4 + r_o^5) - \\
& - 420LR^4 (R - r_o)^2 - 840R^5 (R - r_o)^2)
\end{aligned} \tag{A.24}$$

$$\begin{aligned}
F_{10a2} = & \frac{2(L^2 - R^2)^3 (R - r_o)^2 \log\left(1 - \frac{r_o}{R}\right)}{L^3 r_o^2 (L - 2R)^2 (L + 4R)} + \\
& + \frac{1}{420L^3 r_o (L - 2R)^2 (L + 4R)} (14r_o^5 (3L^2 + 7R^2) + 840R(L^2 - R^2)^3 - \\
& - 28r_o^4 (-8L^3 + 9L^2 R + R^3) - 70r_o^3 (-3L^4 + 16L^3 R - 3L^2 R^2 + R^4) - \\
& - 280Rr_o^2 (3L^4 - 8L^3 R - 3L^2 R^2 + R^4) + 1260r_o (R - L)^3 (R + L)^3 - \\
& - 40Rr_o^6 + 5r_o^7)
\end{aligned} \tag{A.25}$$

$$\begin{aligned}
F_{10a3} = & \frac{2(L^2 - R^2)^3 (R - r_o)^2 \log\left(\frac{L}{R} - 1\right)}{L^3 r_o^2 (L - 2R)^2 (L + 4R)} + \\
& + \frac{1}{140L^3 r_o^2 (L - 2R)(L + 4R)} (77L^7 + L^6 (416r_o - 262R) - \\
& - 2L^5 (577R^2 - 206Rr_o + 35r_o^2) + 4L^4 R (837R^2 - 718Rr_o + 35r_o^2) - \\
& - 2L^3 R^2 (957R^2 - 1258Rr_o + 525r_o^2) - 4L^2 R^3 (R - r_o) (173R + 35r_o) + \\
& + 4LR^4 (67R - 35r_o) (R - r_o) + 256R^6 (R - r_o))
\end{aligned} \tag{A.26}$$

$$\begin{aligned}
F_{10b1} = & \frac{27L^5 - 40L^3 (2R^2 - 4Rr_o + 5r_o^2) + 288L^2 r_o^2 (r_o - R) + 360LR^2 r_o^2 - 32r_o^3 (10R^2 - 5Rr_o + r_o^2)}{30r_o^2 (L - 2R)^2 (L + 4R)}
\end{aligned} \tag{A.27}$$

$$F_{10b2} = \frac{90L^4 r_o^2 + r_o^4 (-40R^2 + 32Rr_o - 7r_o^2)}{30L^3 (L - 2R)^2 (L + 4R)} \tag{A.28}$$

$$\begin{aligned}
F_{10b3} = & \frac{1}{420L^3 r_o^2 (L - 2R)^2 (L + 4R)} (-189L^8 + 1440L^7 (R - r_o) - 3920L^6 (R - r_o)^2 + \\
& + 4032L^5 (R - r_o)^3 + 1260L^4 r_o^4 - 1792L^3 (R - r_o)^5 + 2(128R^8 - 1024R^7 r_o + 3584R^6 r_o^2 - \\
& - 7168R^5 r_o^3 + 8960R^4 r_o^4 - 7168R^3 r_o^5 + 3304R^2 r_o^6 - 800Rr_o^7 + 79r_o^8)
\end{aligned} \tag{A.29}$$

$$\begin{aligned}
F_{10b4} = & \frac{(-48L^2R^2 - 64LR^3 - 64R^4)(R - 7r_o)(R - r_o)}{420L^3r_o^2(L + 4R)} + & (A.30) \\
& + \frac{189L^6 + 36L^5(40r_o - 19R) + 4L^4(107R^2 - 520Rr_o + 560r_o^2) + 32L^3R(13R^2 - 62Rr_o + 28r_o^2)}{420L^3r_o^2(L + 4R)}.
\end{aligned}$$

Bibliography

- [1] P. Scardi and M. Leoni. Whole powder pattern modelling. *Acta Crystallographica Section A*, 58(2):190–200, 2002.
- [2] N. C. Popa. The (hkl) Dependence of Diffraction-Line Broadening Caused by Strain and Size for all Laue Groups in Rietveld Refinement. *Journal of Applied Crystallography*, 31(2):176–180, Apr 1998.
- [3] B. E. Warren. *X-Ray Diffraction*. Dover, New York, 1990.
- [4] R. Koch. *Modeling diffraction of nanostructured materials: a combined theoretical and experimental study*. Phd, University of Trento, 2015.
- [5] S.L. Morelhão. *Computer Simulation Tools for X-ray Analysis: Scattering and Diffraction Methods*. Graduate Texts in Physics. Springer International Publishing, 2015. ISBN 9783319195544. URL <https://books.google.it/books?id=XgCOCgAAQBAJ>.
- [6] B.T.M. Willis and A.W. Pryor. *Thermal Vibrations in Crystallography*. Cambridge University Press, 1975. ISBN 9780521204477. URL <https://books.google.it/books?id=66yIQgAACAAJ>.
- [7] A. Guinier. *X-ray Diffraction in Crystals, Imperfect Crystals, and Amorphous Bodies*. Dover Books on Physics Series. Dover Publications, 1994. ISBN 9780486680118. URL <https://books.google.it/books?id=vjyZFo5nGUoC>.
- [8] Alexandru M. Micu and Jeremy C. Smith. Serena: a program for calculating X-ray diffuse scattering intensities from molecular dynamics trajectories. *Computer Physics Communications*, 91(1):331 – 338, 1995. ISSN 0010-4655. doi: [https://doi.org/10.1016/0010-4655\(95\)00057-M](https://doi.org/10.1016/0010-4655(95)00057-M). URL <http://www.sciencedirect.com/science/article/pii/001046559500057M>.

- [9] P. Debye. Zerstreung von röntgenstrahlen. *Annalen der Physik*, 351(6):809–823, 1915. doi: 10.1002/andp.19153510606. URL <https://onlinelibrary.wiley.com/doi/abs/10.1002/andp.19153510606>.
- [10] A.L. Patterson. The scherrer formula for X-ray particle size determination. *Physical Review*, 56(10):978–982, 1939. doi: 10.1103/PhysRev.56.978. URL <https://www.scopus.com/inward/record.uri?eid=2-s2.0-0001162210&doi=10.1103%2fPhysRev.56.978&partnerID=40&md5=244c2432bf1d58262f42be3266645459>.
- [11] M. von Laue. Vi. Lorentz-faktor und intensitätsverteilung in Debye-Scherrer-ringen. 64:115–142, 1926. ISSN 21967105. URL <https://www.degruyter.com/view/j/zkri.1926.64.issue-1-6/zkri.1926.64.1.115/zkri.1926.64.1.115.xml>.
- [12] K. R. Beyerlein and P. Scardi. Simulating the diffraction line profile from nanocrystalline powders using a spherical harmonics expansion. *Acta Crystallographica Section A*, 74(6):640–646, Nov 2018. doi: 10.1107/S2053273318011452. URL <https://doi.org/10.1107/S2053273318011452>.
- [13] A.J.C. Wilson. *X-ray Optics: The Diffraction of X-rays by Finite and Imperfect Crystals*. Methuen’s monographs on physical subjects. Methuen, 1949. URL <https://books.google.it/books?id=-DY6twEACAAJ>.
- [14] B. E. Warren. A generalized treatment of cold work in powder patterns. *Acta Crystallographica*, 8(8):483–486, Aug 1955. doi: 10.1107/S0365110X55001503. URL <https://doi.org/10.1107/S0365110X55001503>.
- [15] A R Stokes and A J C Wilson. The diffraction of X-rays by distorted crystal aggregates - I. *Proceedings of the Physical Society*, 56(3):174, 1944. URL <http://stacks.iop.org/0959-5309/56/i=3/a=303>.
- [16] Alberto Leonardi, Matteo Leoni, Stefano Siboni, and Paolo Scardi. Common volume functions and diffraction line profiles of polyhedral domains. *Journal of Applied Crystallography*, 45(6):1162–1172, Dec 2012. doi: 10.1107/S0021889812039283. URL <https://doi.org/10.1107/S0021889812039283>.

- [17] M.B. Boisen and G.V. Gibbs. *Mathematical crystallography: an introduction to the mathematical foundations of crystallography, Revised Edition*, volume 15 of *Reviews in mineralogy*. Mineralogical Society of America, 1990.
- [18] C. Perez-Demydenko and P. Scardi. Diffraction peak profiles of surface relaxed spherical nanocrystals. *Philosophical Magazine*, 97(26):2317–2346, 2017. doi: 10.1080/14786435.2017.1332435. URL <https://doi.org/10.1080/14786435.2017.1332435>.
- [19] Marvin L. Cohen. *Theory of Surface Reconstruction*, pages 4–11. Springer Berlin Heidelberg, Berlin, Heidelberg, 1985. ISBN 978-3-642-82493-7.
- [20] K. Oura, V.G. Lifshits, A. Saranin, A.V. Zotov, and M. Katayama. *Surface Science: An Introduction*. Advanced Texts in Physics. Springer-Verlag Berlin Heidelberg, 1 edition, 2003.
- [21] C.W. Mays, J.S. Vermaak, and D. Kuhlmann-Wilsdorf. On surface stress and surface tension. II. Determination of the surface stress of gold. *Surface Science*, 12(2):134–140, 1968. cited By 247.
- [22] J.S. Vermaak and D. Kuhlmann-Wilsdorf. Measurement of the average surface stress of gold as a function of temperature in the temperature range 50-985. *Journal of Physical Chemistry*, 72(12):4150–4154, 1968. cited By 48.
- [23] B. Palosz, E. Grzanka, S. Gierlotka, S. Stel'makh, R. Pielaszek, W. Lojkowski, U. Bismayer, J. Neufeind, H.-P. Weber, and W. Palosz. Application of x-ray powder diffraction to nano-materials - determination of the atomic structure of nanocrystals with relaxed and strained surfaces. *Phase Transitions*, 76(1-2):171–185, 2003. doi: 10.1080/0141159031000076129. URL <https://doi.org/10.1080/0141159031000076129>.
- [24] A. C. Nunes and D. Lin. Effects of surface relaxation on powder diffraction patterns of very fine particles. *Journal of Applied Crystallography*, 28(3):274–278, 1995.
- [25] Kenji Ishikawa and Takatoshi Uemori. Surface relaxation in ferroelectric perovskites. *Physical Review B*, 60(17):11841–11845, 1999.

- [26] W. J. Huang, R. Sun, J. Tao, L. D. Menard, R. G. Nuzzo, and J. M. Zuo. Coordination-dependent surface atomic contraction in nanocrystals revealed by coherent diffraction. *Nat Mater*, 7(4):308–313, 2008. 10.1038/nmat2132.
- [27] Kenneth R. Beyerlein, Robert L. Snyder, Mo. Li, and P. Scardi. Simulation and modeling of nanoparticle surface strain. *Journal of nanoscience and nanotechnology*, 12(11):8554–8560, 2012.
- [28] L. Gelisio and P. Scardi. On the modeling of the diffraction pattern from metal nanocrystals. *Metallurgical and Materials Transactions A: Physical Metallurgy and Materials Science*, 45(11):4786–4795, 2014. cited By 4.
- [29] M. Leoni and P. Scardi. Grain surface relaxation effects in powder diffraction. In Eric J. Mittemeijer and Paolo Scardi, editors, *Diffraction Analysis of the Microstructure of Materials*, pages 413–454. Springer Berlin Heidelberg, Berlin, Heidelberg, 2004. ISBN 978-3-662-06723-9.
- [30] Jillian F. Banfield and Hengzhong Zhang. Nanoparticles in the environment. In J. F. Banfield and A. Navrotsky, editors, *Nanoparticles and the Environment*, pages 1–58. Mineralogical Society of America, Washington, D.C., 2001. ISBN 0-939950-56-1. doi: <http://dx.doi.org/10.1180/0380255>.
- [31] H.J. Wasserman and J.S. Vermaak. On the determination of a lattice contraction in very small silver particles. *Surface Science*, 22(1):164–172, 1970. doi: 10.1016/0039-6028(70)90031-2. cited By 148.
- [32] H.J. Wasserman and J.S. Vermaak. On the determination of the surface stress of copper and platinum. *Surface Science*, 32(1):168–174, 1972. doi: 10.1016/0039-6028(72)90127-6. cited By 129.
- [33] J. Woltersdorf, A.S. Nepijko, and E. Pippel. Dependence of lattice parameters of small particles on the size of the nuclei. *Surface Science*, 106(1-3):64–69, 1981. doi: 10.1016/0039-6028(81)90182-5. cited By 87.
- [34] S. Onodera. Lattice parameters of fine copper and silver particles. *Journal of the Physical Society of Japan*, 61(7):2190–2193, 1992. cited By 7.

- [35] J. Sheng, U. Welzel, and E.J. Mittemeijer. Nonmonotonic crystallite-size dependence of the lattice parameter of nanocrystalline nickel. *Applied Physics Letters*, 97(15):153109, 2010. doi: 10.1063/1.3500827. cited By 15.
- [36] M. Ya. Gamarnik. Change of lattice parameters in highly disperse nickel powders. *physica status solidi (b)*, 168(2):389–395, 1991. ISSN 1521-3951. doi: 10.1002/pssb.2221680202.
- [37] X.D. Liu, H.Y. Zhang, K. Lu, and Z.Q. Hu. The lattice expansion in nanometre-sized Ni polycrystals. *Journal of Physics: Condensed Matter*, 6(34):L497–L502, 1994. doi: 10.1088/0953-8984/6/34/001. cited By 67.
- [38] Z. Wei, T. Xia, J. Ma, W. Feng, J. Dai, Q. Wang, and P. Yan. Investigation of the lattice expansion for Ni nanoparticles. *Materials Characterization*, 58(10):1019–1024, 2007. doi: 10.1016/j.matchar.2006.08.004. cited By 30.
- [39] P. Zimmer and R. Birringer. Measuring the interface stress of nanocrystalline iron. *Applied Physics Letters*, 92(8):081912, 2008. doi: 10.1063/1.2888751. cited By 4.
- [40] G.K. Rane, U. Welzel, S.R. Meka, and E.J. Mittemeijer. Non-monotonic lattice parameter variation with crystallite size in nanocrystalline solids. *Acta Materialia*, 61(12):4524–4533, 2013. doi: 10.1016/j.actamat.2013.04.021. cited By 17.
- [41] X.F. Yu, X. Liu, K. Zhang, and Z.Q. Hu. The lattice contraction of nanometre-sized Sn and Bi particles produced by an electrohydrodynamic technique. *Journal of Physics Condensed Matter*, 11(4):937–944, 1999. doi: 10.1088/0953-8984/11/4/001. cited By 55.
- [42] A.M. Stoneham. Comment on ‘The lattice contraction of nanometre-sized Sn and Bi particles produced by an electrohydrodynamic technique’. *Journal of Physics Condensed Matter*, 11(42):8351–8352, 1999. doi: 10.1088/0953-8984/11/42/315. cited By 14.
- [43] C.Q. Sun. Comment on ‘The lattice contraction of nanometre-sized Sn and Bi particles produced by an electrohydrodynamic technique’. *Journal of Physics Condensed Matter*, 11(24):4801–4803, 1999. doi: 10.1088/0953-8984/11/24/401. cited By 35.

- [44] K.K. Nanda, S.N. Behera, and S.N. Sahu. Comment on ‘The lattice contraction of nanometre-sized Sn and Bi particles produced by an electrohydrodynamic technique’. *Journal of Physics Condensed Matter*, 13(12):2861–2864, 2001. doi: 10.1088/0953-8984/13/12/401. cited By 26.
- [45] M.I. Ahmad and S.S. Bhattacharya. Size effect on the lattice parameters of nanocrystalline anatase. *Applied Physics Letters*, 95(19), 2009. doi: 10.1063/1.3261754. cited By 26.
- [46] S. Tsunekawa, S. Ito, and Y. Kawazoe. Surface structures of cerium oxide nanocrystalline particles from the size dependence of the lattice parameters. *Applied Physics Letters*, 85(17):3845–3847, 2004. doi: 10.1063/1.1811771. cited By 46.
- [47] L. Wu, H.J. Wiesmann, A.R. Moodenbaugh, R.F. Klie, Y. Zhu, D.O. Welch, and M. Suenaga. Oxidation state and lattice expansion of CeO_{2-x} nanoparticles as a function of particle size. *Physical Review B - Condensed Matter and Materials Physics*, 69(12):1254151–1254159, 2004. cited By 193.
- [48] S. Tsunekawa, S. Ito, T. Mori, K. Ishikawa, Z.-Q. Li, and Y. Kawazoe. Critical size and anomalous lattice expansion in nanocrystalline $BaTiO_3$ particles. *Physical Review B - Condensed Matter and Materials Physics*, 62(5):3065–3070, 2000. cited By 106.
- [49] XueWei Wu, DaJian Wu, and XiaoJun Liu. Negative pressure effects in $SrTiO_3$ nanoparticles investigated by raman spectroscopy. *Solid State Communications*, 145(5–6):255 – 258, 2008. ISSN 0038-1098. doi: <http://dx.doi.org/10.1016/j.ssc.2007.11.018>.
- [50] E.K. Akdogan, C.J. Rawn, W.D. Porter, E.A. Payzant, and A. Safari. Size effects in $PbTiO_3$ nanocrystals: Effect of particle size on spontaneous polarization and strains. *Journal of Applied Physics*, 97(8):084305, 2005. doi: 10.1063/1.1872195. cited By 44.
- [51] A. Cimino, P. Porta, and M. Valigi. Dependence of the lattice parameter of magnesium oxide on crystallite size. *Journal of the American Ceramic Society*, 49(3):152–156, 1966. doi: 10.1111/j.1151-2916.1966.tb15394.x. cited By 49.
- [52] A. Kumar and J. Kumar. On the synthesis and optical absorption studies of nano-size magnesium oxide powder. *Journal of Physics*

- and Chemistry of Solids*, 69(11):2764–2772, 2008. doi: 10.1016/j.jpics.2008.06.143. cited By 57.
- [53] P. Ayyub, M. Multani, M. Barma, V.R. Palkar, and R. Vijayaraghavan. Size-induced structural phase transitions and hyperfine properties of microcrystalline Fe_2O_3 . *Journal of Physics C: Solid State Physics*, 21(11):2229–2245, 1988. doi: 10.1088/0022-3719/21/11/014. cited By 158.
- [54] N. Uekawa, N. Mochizuki, J. Kajiwara, F. Mori, Y.J. Wu, and K. Kakegawa. Nonstoichiometric properties of zinc oxide nanoparticles prepared by decomposition of zinc peroxide. *Physical Chemistry Chemical Physics*, 5(5):929–934, 2003. doi: 10.1039/b210990e. cited By 49.
- [55] N. Uekawa, N. Mochizuki, J. Kajiwara, F. Mori, Y.J. Wu, and K. Kakegawa. Erratum: Nonstoichiometric properties of zinc oxide nanoparticles prepared by decomposition of zinc peroxide. *Physical Chemistry Chemical Physics*, 5(7):1489–1490, 2003. cited By 1.
- [56] J. Li, R. Kykyneshi, J. Tate, and A.W. Sleight. p-type zinc oxide powders. *Solid State Sciences*, 9(7):613–618, 2007. doi: 10.1016/j.solidstatesciences.2007.02.007. cited By 14.
- [57] J. Zhang and L. Gao. Synthesis and characterization of nanocrystalline tin oxide by sol-gel method. *Journal of Solid State Chemistry*, 177(4-5):1425–1430, 2004. doi: 10.1016/j.jssc.2003.11.024. cited By 178.
- [58] E. Abdelkader, L. Nadjia, B. Naceur, and B. Noureddine. SnO_2 foam grain-shaped nanoparticles: Synthesis, characterization and UVA light induced photocatalysis. *Journal of Alloys and Compounds*, 679:408–419, 2016. doi: 10.1016/j.jallcom.2016.04.016. cited By 0.
- [59] P. Ayyub, V.R. Palkar, S. Chattopadhyay, and M. Multani. Effect of crystal size reduction on lattice symmetry and cooperative properties. *Physical Review B*, 51(9):6135–6138, 1995. doi: 10.1103/PhysRevB.51.6135. cited By 249.
- [60] M. Fukuhara. Lattice expansion of nanoscale compound particles. *Physics Letters, Section A: General, Atomic and Solid State Physics*, 313(5-6):427–430, 2003. doi: 10.1016/S0375-9601(03)00793-X. cited By 33.

- [61] P.M. Diehm, P. Ágoston, and K. Albe. Size-dependent lattice expansion in nanoparticles: Reality or anomaly? *ChemPhysChem*, 13(10):2443–2454, 2012. doi: 10.1002/cphc.201200257. cited By 42.
- [62] K. Ohshima and J. Harada. An X-ray diffraction study of soft surface vibrations of fcc fine metal particles. *Journal of Physics C: Solid State Physics*, 17(9):1607–1616, 1984. doi: 10.1088/0022-3719/17/9/017. cited By 12.
- [63] M. Dubiel, S. Brunsch, W. Seifert, H. Hofmeister, and G.L. Tan. Stress state of silver nanoparticles embedded in a silicate glass matrix investigated by HREM and EXAFS spectroscopy. *European Physical Journal D*, 8(3):229–232, 2001. cited By 20.
- [64] G. Li, L. Li, J. Boerio-Goates, and B.F. Woodfield. High purity anatase TiO_2 nanocrystals: Near room-temperature synthesis, grain growth kinetics, and surface hydration chemistry. *Journal of the American Chemical Society*, 127(24):8659–8666, 2005. doi: 10.1021/ja050517g. cited By 357.
- [65] Y. Ding, Y. Gao, Z. L. Wang, N. Tian, Z. Y. Zhou, and S. Sun. Facets and surface relaxation of tetrahedral platinum nanocrystals. *Applied Physics Letters*, 91(12):121901–1219013, 2007.
- [66] Na Tian, Zhi-You Zhou, Shi-Gang Sun, Yong Ding, and Zhong Lin Wang. Synthesis of tetrahedral platinum nanocrystals with high-index facets and high electro-oxidation activity. *Science*, 316(5825):732–735, 2007. ISSN 0036-8075. doi: 10.1126/science.1140484.
- [67] Na Tian, Zhi-You Zhou, and Shi-Gang Sun. Platinum metal catalysts of high-index surfaces: From single-crystal planes to electrochemically shape-controlled nanoparticles. *The Journal of Physical Chemistry C*, 112(50):19801–19817, 2008. doi: 10.1021/jp804051e.
- [68] Wenxin Niu, Shanliang Zheng, Dawei Wang, Xiaoqing Liu, Haijuan Li, Shuang Han, Jiuan Chen, Zhiyong Tang, and Guobao Xu. Selective synthesis of single-crystalline rhombic dodecahedral, octahedral, and cubic gold nanocrystals. *Journal of the American Chemical Society*, 131(2):697–703, 2009. doi: 10.1021/ja804115r. PMID: 19102696.
- [69] Zhenmeng Peng and Hong Yang. Designer platinum nanoparticles: Control of shape, composition in alloy, nanostructure and electrocat-

alytic property. *Nano Today*, 4(2):143 – 164, 2009. ISSN 1748-0132. doi: <http://dx.doi.org/10.1016/j.nantod.2008.10.010>.

- [70] Wenxin Niu, Ling Zhang, and Guobao Xu. Shape-controlled synthesis of single-crystalline palladium nanocrystals. *ACS Nano*, 4(4): 1987–1996, 2010. doi: 10.1021/nn100093y. PMID: 20307089.
- [71] Xiaohu Xia, Jie Zeng, L. Kyle Oetjen, Qingge Li, and Younan Xia. Quantitative analysis of the role played by poly(vinylpyrrolidone) in seed-mediated growth of Ag nanocrystals. *Journal of the American Chemical Society*, 134(3):1793–1801, 2012. doi: 10.1021/ja210047e. PMID: 22206387.
- [72] Shuo Liu, Na Tian, Ai-Yun Xie, Jia-Huan Du, Jing Xiao, Li Liu, Hong-Yu Sun, Zhi-Ying Cheng, Zhi-You Zhou, and Shi-Gang Sun. Electrochemically seed-mediated synthesis of sub-10 nm tetrahedral Pt nanocrystals supported on graphene with improved catalytic performance. *Journal of the American Chemical Society*, 138(18):5753–5756, 2016. doi: 10.1021/jacs.5b13473. PMID: 27063648.
- [73] Tao Huang and Xiao-Hong Nancy Xu. Synthesis and characterization of tunable rainbow colored colloidal silver nanoparticles using single-nanoparticle plasmonic microscopy and spectroscopy. *J. Mater. Chem.*, 20:9867–9876, 2010. doi: 10.1039/C0JM01990A.
- [74] Qiang Zhang, Weiyang Li, Christine Moran, Jie Zeng, Jingyi Chen, Long-Ping Wen, and Younan Xia. Seed-mediated synthesis of Ag nanocubes with controllable edge lengths in the range of 30–200 nm and comparison of their optical properties. *Journal of the American Chemical Society*, 132(32):11372–11378, 2010. doi: 10.1021/ja104931h. PMID: 20698704.
- [75] Qingbo Zhang, Jianping Xie, Yue Yu, Jinhua Yang, and Jim Yang Lee. Tuning the crystallinity of Au nanoparticles. *Small*, 6(4):523–527, 2010. ISSN 1613-6829. doi: 10.1002/sml.200902033.
- [76] Yiqun Zheng, Yanyun Ma, Jie Zeng, Xiaolan Zhong, Mingshang Jin, Zhi-Yuan Li, and Younan Xia. Seed-mediated synthesis of single-crystal gold nanospheres with controlled diameters in the range 5–30 nm and their self-assembly upon dilution. *Chemistry – An Asian Journal*, 8(4):792–799, 2013. ISSN 1861-471X. doi: 10.1002/asia.201201105.

- [77] V. Nandwana, K.E. Elkins, N. Poudyal, G.S. Chaubey, K. Yano, and J.P. Liu. Size and shape control of monodisperse FePt nanoparticles. *Journal of Physical Chemistry C*, 111(11):4185–4189, 2007. doi: 10.1021/jp068330e. cited By 109.
- [78] L. Colak and G.C. Hadjipanayis. Chemically synthesized FePt nanoparticles with controlled particle size, shape and composition. *Nanotechnology*, 20(48):485602, 2009. doi: 10.1088/0957-4484/20/48/485602. cited By 15.
- [79] B.R. Bian, J. Du, W.X. Xia, J. Zhang, J.P. Liu, W. Li, Z.H. Guo, and A.R. Yan. Effect of reaction temperature on the shape of FePt nanoparticles. *IEEE Transactions on Magnetics*, 50(11):2102704, 2014. doi: 10.1109/TMAG.2014.2322879. cited By 0.
- [80] K. Elkins, D. Li, N. Poudyal, V. Nandwana, Z. Jin, K. Chen, and J.P. Liu. Monodisperse face-centred tetragonal FePt nanoparticles with giant coercivity. *Journal of Physics D: Applied Physics*, 38(14):2306–2309, 2005. doi: 10.1088/0022-3727/38/14/003. cited By 104.
- [81] Y. Tamada, S. Yamamoto, M. Takano, S. Nasu, and T. Ono. Well-ordered $L1_0$ -FePt nanoparticles synthesized by improved SiO_2 -nanoreactor method. *Applied Physics Letters*, 90(16):162509, 2007. doi: 10.1063/1.2728760. cited By 24.
- [82] J. Kim, C. Rong, Y. Lee, J.P. Liu, and S. Sun. From core/shell structured FePt/ Fe_3O_4 /MgO to ferromagnetic FePt nanoparticles. *Chemistry of Materials*, 20(23):7242–7245, 2008. doi: 10.1021/cm8024878. cited By 51.
- [83] J. Kim, C. Rong, J. Ping Liu, and S. Sun. Dispersible ferromagnetic FePt nanoparticles. *Advanced Materials*, 21(8):906–909, 2009. doi: 10.1002/adma.200801620. cited By 84.
- [84] M. Delalande, M.J.-F. Guinel, L.F. Allard, A. Delattre, R. Le Bris, Y. Samson, P. Bayle-Guillemaud, and P. Reiss. $L1_0$ ordering of ultrasmall FePt nanoparticles revealed by tem in situ annealing. *Journal of Physical Chemistry C*, 116(12):6866–6872, 2012. doi: 10.1021/jp300037r. cited By 26.
- [85] S. O’Brien, L. Brus, and C.B. Murray. Synthesis of monodisperse nanoparticles of barium titanate: Toward a generalized strategy of

- oxide nanoparticle synthesis. *Journal of the American Chemical Society*, 123(48):12085–12086, 2001. doi: 10.1021/ja011414a. cited By 333.
- [86] J. Tang, F. Redl, Y. Zhu, T. Siegrist, L.E. Brus, and M.L. Steigerwald. An organometallic synthesis of TiO_2 nanoparticles. *Nano Letters*, 5(3):543–548, 2005. doi: 10.1021/nl047992h. cited By 90.
- [87] N. Zhao, W. Nie, X. Liu, S. Tian, Y. Zhang, and X. Ji. Shape- and size-controlled synthesis and dependent magnetic properties of nearly monodisperse Mn_3O_4 nanocrystals. *Small*, 4(1):77–81, 2008. doi: 10.1002/smll.200700698. cited By 49.
- [88] T. I. Mazilova and I. M. Mikhailovskij. Atomic relaxation at the kinks of steps on the {112} tungsten surface. *Technical Physics Letters*, 29(12):989–990, Dec 2003. ISSN 1090-6533. doi: 10.1134/1.1639451. URL <https://doi.org/10.1134/1.1639451>.
- [89] L. Gelisio, K. R. Beyerlein, and P. Scardi. Atomistic modeling of lattice relaxation in metallic nanocrystals. *Thin Solid Films*, 530: 35–39, 2013.
- [90] J.F Nye. *Physical Properties of Crystals: Their Representation by Tensors and Matrices*. Oxford: Clarendon Press, 1985.
- [91] L. Pauling. Atomic radii and interatomic distances in metals. *Journal of the American Chemical Society*, 69(3):542–553, 1947. cited By 932.
- [92] L.X. Chen, T. Rajh, W. Jäger, J. Nedeljkovic, and M.C. Thurnauer. X-ray absorption reveals surface structure of titanium dioxide nanoparticles. *Journal of Synchrotron Radiation*, 6(3):445–447, 1999. cited By 97.
- [93] M. Rappaz and A. Châtelain. Existence of a surface-induced pressure in anisotropic crystals. *Journal of Physics C: Solid State Physics*, 14 (30):4515–4520, 1981. doi: 10.1088/0022-3719/14/30/015. cited By 9.
- [94] J.-P. Borel and A. Châtelain. Surface stress and surface tension: Equilibrium and pressure in small particles. *Surface Science*, 156 (PART 2):572–579, 1985. doi: 10.1016/0039-6028(85)90226-2. cited By 25.

- [95] B.E. Warren and B.L. Averbach. The effect of cold-work distortion on X-ray patterns. *Journal of Applied Physics*, 21(6):595–599, 1950. doi: 10.1063/1.1699713. cited By 863.
- [96] B.E. Warren and B.L. Averbach. The separation of cold-work distortion and particle size broadening in X-ray patterns. *Journal of Applied Physics*, 23, 03 1952. doi: 10.1063/1.1702234.
- [97] Paolo Scardi, Cristy L. Azanza Ricardo, Camilo Perez-Demydenko, and Alan A. Coelho. Whole powder pattern modelling macros for *TOPAS*. *Journal of Applied Crystallography*, 51(6):1752–1765, Dec 2018. doi: 10.1107/S160057671801289X. URL <https://doi.org/10.1107/S160057671801289X>.
- [98] Alan A. Coelho. *Topas-academic*. Version 7, 2018.
- [99] Alan A. Coelho. *TOPAS* and *TOPAS-Academic*: an optimization program integrating computer algebra and crystallographic objects written in C++. *Journal of Applied Crystallography*, 51(1):210–218, Feb 2018. doi: 10.1107/S1600576718000183.
- [100] L. Gelisio. *Structure and properties of nanostructured materials from atomistic modeling and advanced diffraction methods*. Phd, University of Trento, 2014. URL <http://eprints-phd.biblio.unitn.it/1373/>.
- [101] D.C. Rapaport, D.C.R. Rapaport, and ProQuest (Firm). *The Art of Molecular Dynamics Simulation*. Cambridge University Press, 2004. ISBN 9780521825689. URL <https://books.google.it/books?id=iqDJ2hjQBMEC>.
- [102] M.E. Tuckerman. *Statistical Mechanics: Theory and Molecular Simulation*. Oxford graduate texts. Oxford University Press, 2011. URL <https://books.google.it/books?id=UMM2NAEACAAJ>.
- [103] A. P. Miiller and B. N. Brockhouse. Anomalous behavior of the lattice vibrations and the electronic specific heat of palladium. *Phys. Rev. Lett.*, 20:798–801, Apr 1968. doi: 10.1103/PhysRevLett.20.798. URL <https://link.aps.org/doi/10.1103/PhysRevLett.20.798>.
- [104] A. P. Miiller and B. N. Brockhouse. Crystal dynamics and electronic specific heats of palladium and copper. *Canadian Journal of Physics*, 49(6):704–723, 1971. doi: 10.1139/p71-087. URL <https://doi.org/10.1139/p71-087>.

- [105] Murray S. Daw and M. I. Baskes. Embedded-atom method: Derivation and application to impurities, surfaces, and other defects in metals. *Phys. Rev. B*, 29:6443–6453, Jun 1984. doi: 10.1103/PhysRevB.29.6443. URL <https://link.aps.org/doi/10.1103/PhysRevB.29.6443>.
- [106] <https://sites.google.com/site/eampotentials/>.
- [107] Steve Plimpton. Fast parallel algorithms for short-range molecular dynamics. *Journal of Computational Physics*, 117(1):1 – 19, 1995. ISSN 0021-9991. doi: <https://doi.org/10.1006/jcph.1995.1039>. URL <http://www.sciencedirect.com/science/article/pii/S002199918571039X>.
- [108] Andrew B. Yankovich, Benjamin Berkels, W. Dahmen, P. Binev, S. I. Sanchez, S. A. Bradley, Ao Li, Izabela Szlufarska, and Paul M. Voyles. Picometre-precision analysis of scanning transmission electron microscopy images of platinum nanocatalysts. *Nature Communications*, 5:4155, June 2014.
- [109] P. Scardi, A. Leonardi, L. Gelisio, M. R. Suchomel, B. T. Sneed, M. K. Sheehan, and C. K. Tsung. Anisotropic atom displacement in Pd nanocubes resolved by molecular dynamics simulations supported by X-ray diffraction imaging. *Physical Review B*, 91(15):155414, 2015. PRB.
- [110] H.W. Sheng, M.J. Kramer, A. Cadien, T. Fujita, and M.W. Chen. Highly optimized embedded-atom-method potentials for fourteen fcc metals. *Physical Review B - Condensed Matter and Materials Physics*, 83(13):134118, 2011. doi: 10.1103/PhysRevB.83.134118. cited By 102.
- [111] Alberto Leonardi, Matteo Leoni, and Paolo Scardi. Directional pair distribution function for diffraction line profile analysis of atomistic models. *Journal of Applied Crystallography*, 46(1):63–75, 2013.
- [112] R.W. James. *The Optical Principles of the Diffraction of X-rays*. Crystalline state. Bell, 1950. URL <https://books.google.it/books?id=cIsynQEACAAJ>.
- [113] K. R. Beyerlein. *Simulation and Modeling of the Powder Diffraction Pattern from Nanoparticles: Studying the Effects of Faulting in Small Crystallites*. Phd, University of Trento, 2011. URL <http://eprints-phd.biblio.unitn.it/591/>.

- [114] J.M. Cowley. *Diffraction Physics*. North-Holland Personal Library. Elsevier Science, 1995. ISBN 9780080530390. URL <https://books.google.it/books?id=S3ekKcs2QoIC>.
- [115] K. R. Beyerlein, M. Leoni, and P. Scardi. Temperature diffuse scattering of nanocrystals. *Acta Crystallographica Section A*, 68(3):382–392, May 2012. doi: 10.1107/S0108767312009853. URL <https://doi.org/10.1107/S0108767312009853>.
- [116] Elliott W. Montroll. Size effect in low temperature heat capacities. *The Journal of Chemical Physics*, 18(2):183–185, 1950. doi: 10.1063/1.1747584. URL <https://doi.org/10.1063/1.1747584>.
- [117] F. R. L. Schoening. The Debye–Waller factor for small cubes and thin films. *Acta Crystallographica Section A*, 24(6):615–619, Nov 1968. doi: 10.1107/S0567739468001348. URL <https://doi.org/10.1107/S0567739468001348>.
- [118] J. P. Urban. Thermal diffuse X-ray scattering for small samples and small coherent scattering domains. *Acta Crystallographica Section A*, 31(1):95–100, Jan 1975. doi: 10.1107/S0567739475000186. URL <https://doi.org/10.1107/S0567739475000186>.
- [119] R. H. Bolt. Frequency distribution of eigentones in a threedimensional continuum. *The Journal of the Acoustical Society of America*, 10(3):258–258, 1939. doi: 10.1121/1.1902105. URL <https://doi.org/10.1121/1.1902105>.
- [120] DahYou Maa. Distribution of eigentones in a rectangular chamber at low frequency range. *The Journal of the Acoustical Society of America*, 10(3):235–238, 1939. doi: 10.1121/1.1915981. URL <https://doi.org/10.1121/1.1915981>.
- [121] P. Brüesch. *Phonons, theory and experiments*. Number v. 1 in Phonons, Theory and Experiments. Springer-Verlag, 1982. ISBN 9783540113065. URL <https://books.google.it/books?id=BxbAtwEACAAJ>.
- [122] S.L. Chaplot, R. Mittal, and N. Choudhury. *Thermodynamic Properties of Solids: Experiment and Modeling*. Wiley, 2010. ISBN 9783527630424. URL <https://books.google.it/books?id=vydJKiaKsR8C>.

- [123] P. Suortti. *Correction of integrated Bragg reflections of cubic powders for thermal diffuse scattering*. Annales Academiae Scientiarum Fennicae, Series A, VI. Physica, 240, Helsinki, 1967.
- [124] K. M. Górski, E. Hivon, A. J. Banday, B. D. Wandelt, F. K. Hansen, M. Reinecke, and M. Bartelmann. HEALPix: A framework for high-resolution discretization and fast analysis of data distributed on the sphere. *The Astrophysical Journal*, 622(2):759, 2005. URL <http://stacks.iop.org/0004-637X/622/i=2/a=759>.
- [125] Th. Proffen and R. B. Neder. Discus: a program for diffuse scattering and defect-structure simulation. *Journal of Applied Crystallography*, 30(2):171–175, 1997. doi: 10.1107/S002188989600934X. URL <https://onlinelibrary.wiley.com/doi/abs/10.1107/S002188989600934X>.
- [126] Reinhard B. Neder and Thomas Proffen. *Diffuse Scattering and Defect Structure Simulations: A cook book using the program DISCUS*. Oxford University Press, Oxford, 2008. URL <http://www.oxfordscholarship.com/10.1093/acprof:oso/9780199233694.001.0001/acprof-9780199233694>.
- [127] Shawn P. Coleman, Mehrdad M. Sichani, and Douglas E. Spearot. A computational algorithm to produce virtual x-ray and electron diffraction patterns from atomistic simulations. *JOM*, 66(3):408–416, Mar 2014. ISSN 1543-1851. doi: 10.1007/s11837-013-0829-3. URL <https://doi.org/10.1007/s11837-013-0829-3>.
- [128] Benjamin Lindner and Jeremy C. Smith. Sassena — x-ray and neutron scattering calculated from molecular dynamics trajectories using massively parallel computers. *Computer Physics Communications*, 183(7):1491 – 1501, 2012. ISSN 0010-4655. doi: <https://doi.org/10.1016/j.cpc.2012.02.010>. URL <http://www.sciencedirect.com/science/article/pii/S001046551200063X>.
- [129] I.C. Noyan and J.B. Cohen. *Residual Stress: Measurement by Diffraction and Interpretation*. Materials Research and Engineering. Springer New York, 1987. ISBN 9780387963785. URL <https://books.google.it/books?id=c2NsQgAACAAJ>.
- [130] G.S. Schajer. *Practical Residual Stress Measurement Methods*. Wiley, 2013. ISBN 9781118402825. URL <https://books.google.it/books?id=teVvAAAAQBAJ>.

- [131] H.P. Klug and L.E. Alexander. *X-Ray Diffraction Procedures: For Polycrystalline and Amorphous Materials*. A Wiley-interscience publication. Wiley, 1974. ISBN 9780471493693. URL <https://books.google.it/books?id=GaQRAQAIAAJ>.
- [132] R.L. Snyder, J. Fiala, H.J. Bunge, H.J. Bunge, and International Union of Crystallography. *Defect and Microstructure Analysis by Diffraction*. IUCr monographs on crystallography. Oxford University Press, 1999. ISBN 9780198501893. URL https://books.google.it/books?id=b_4m8iQiW94C.
- [133] E.J. Mittemeijer and P. Scardi. *Diffraction Analysis of the Microstructure of Materials*. Springer Series in Materials Science. Springer Berlin Heidelberg, 2003. ISBN 9783540405191.
- [134] Jorge Martinez-Garcia, Matteo Leoni, and Paolo Scardi. A general approach for determining the diffraction contrast factor of straight-line dislocations. *Acta Crystallographica Section A*, 65(2):109–119, Mar 2009. doi: 10.1107/S010876730804186X.
- [135] Andreas Leineweber and Eric J. Mittemeijer. Diffraction line broadening due to lattice-parameter variations caused by a spatially varying scalar variable: its orientation dependence caused by locally varying nitrogen content in ϵ -FeN_{0.433}. *Journal of Applied Crystallography*, 37(1):123–135, Feb 2004. doi: 10.1107/S0021889803026906. URL <https://doi.org/10.1107/S0021889803026906>.
- [136] Peter W. Stephens. Phenomenological model of anisotropic peak broadening in powder diffraction. *Journal of Applied Crystallography*, 32(2):281–289, Apr 1999. doi: 10.1107/S0021889898006001. URL <https://doi.org/10.1107/S0021889898006001>.
- [137] B.E. Warren. X-ray studies of deformed metals. *Progress in Metal Physics*, 8:147 – 202, 1959. ISSN 0502-8205. doi: [https://doi.org/10.1016/0502-8205\(59\)90015-2](https://doi.org/10.1016/0502-8205(59)90015-2). URL <http://www.sciencedirect.com/science/article/pii/0502820559900152>.
- [138] MA Krivoglaz and KP Ryaboshapka. Theory of X-ray scattering by crystals containing dislocations. case of random distribution of screw and edge dislocations in the crystal. *Phys Met Metallogr*, 15 (18), 1963.

- [139] M.A. Krivoglaz. *X-ray and neutron diffraction in nonideal crystals*. Springer, 1996. ISBN 9783540505648. URL <https://books.google.it/books?id=cgzwAAAAMAAJ>.
- [140] M. Wilkens. The mean square stresses $\langle \sigma^2 \rangle$ for a completely random and a restrictedly random distribution of dislocations in a cylindrical body. In J. A. Simmons, R. de Witt, and R. Bullough, editors, *Fundamental Aspects of Dislocation Theory: Conference Proceedings, National Bureau of Standards, April 21-25, 1969*, pages 1191–1193. U.S. Department of Commerce, National Bureau of Standards, Special Publication 317, 1969.
- [141] M. Wilkens. X-ray line broadening and mean square strains of straight dislocations in elastically anisotropic crystals of cubic symmetry. *physica status solidi (a)*, 104(1):K1–K6, 1987. doi: 10.1002/pssa.2211040137. URL <https://onlinelibrary.wiley.com/doi/abs/10.1002/pssa.2211040137>.
- [142] Nicholas Armstrong, Matteo Leoni, and P Scardi. Considerations concerning Wilkens’ theory of dislocation line-broadening. *Zeitschrift für Kristallographie Supplements*, 2006:81–86, 06 2006.
- [143] P. Scardi, M. Ermrich, A. Fitch, E-Wen Huang, R. Jardin, R. Kuzel, A. Leineweber, A. Mendoza Cuevas, S. T. Misture, L. Rebuffi, and Christian Schimpf. Size–strain separation in diffraction line profile analysis. *Journal of Applied Crystallography*, 51(3):831–843, Jun 2018. doi: 10.1107/S1600576718005411. URL <https://doi.org/10.1107/S1600576718005411>.
- [144] T. Hahn. *International Tables for Crystallography, Volume A: Space Group Symmetry*. International Tables for Crystallography. Springer Netherlands, 2005. ISBN 9780792365907. URL <https://books.google.it/books?id=wmdwyvvn4wQC>.
- [145] I D Morokhov, V I Petinov, L I Trusov, and V F Petrunin. Structure and properties of fine metallic particles. *Soviet Physics Uspekhi*, 24(4):295, 1981. URL <http://stacks.iop.org/0038-5670/24/i=4/a=R03>.
- [146] N. Nishiguchi and T. Sakuma. Vibrational spectrum and specific heat of fine particles. *Solid State Communications*, 38(11):1073 – 1077, 1981. ISSN 0038-1098. doi: [https://doi.org/10.1002/1522-2720\(198106\)38:11%3C1073::AID-SSC1073%3E3.0.CO;2-3](https://doi.org/10.1002/1522-2720(198106)38:11%3C1073::AID-SSC1073%3E3.0.CO;2-3).

1016/0038-1098(81)90020-X. URL <http://www.sciencedirect.com/science/article/pii/003810988190020X>.

- [147] A Tamura, K Higeta, and T Ichinokawa. Lattice vibrations and specific heat of a small particle. *Journal of Physics C: Solid State Physics*, 15(24):4975, 1982. URL <http://stacks.iop.org/0022-3719/15/i=24/a=010>.
- [148] Aurélien Crut, Paolo Maioli, Natalia Del Fatti, and Fabrice Vallée. Acoustic vibrations of metal nano-objects: Time-domain investigations. *Physics Reports*, 549:1 – 43, 2015. ISSN 0370-1573. doi: <https://doi.org/10.1016/j.physrep.2014.09.004>. URL <http://www.sciencedirect.com/science/article/pii/S0370157314003172>. Acoustic vibrations of metal nano-objects: Time-domain investigations.
- [149] Eric W. Weisstein. Mathworld—A wolfram web resource,“Dilogarithm”. URL <http://mathworld.wolfram.com/Dilogarithm.html>.